Simulation of Location-Aided Beam Management for 5G-NR Networks in ns-3

Artiom Palovandov

Master's Thesis

March 24, 2025

Examiners

Prof. Dr.-Ing. Marina Petrova
Dr. Ljiljana Simić

Supervisors

Prof. Dr.-Ing. Marina Petrova
Research Assistant, M.Sc. Aron Schott
Research Assistant, M.Sc. Enrico Tosi

Mobile Communications and Computing
RWTH Aachen University

communicated by Prof. Dr.-Ing. Marina Petrova

The present work was submitted to Mobile Communications and Computing

Simulation of Location-Aided Beam Management for 5G-NR Networks in ns-3

Master's Thesis

presented by
Artiom Palovandov

Prof. Dr.-Ing. Marina Petrova
Dr. Ljiljana Simić

Aachen, March 24, 2025

(Artiom Palovandov)

Acknowledgements

I would like to thank Prof. Dr.-Ing. Marina Petrova and Dr. Ljiljana Simić for the opportunity to work on this thesis and explore the forward-looking topic in the context of 5G-NR networks. I am also deeply thankful to Aron Schott and Enrico Tosi for their exceptionally supportive supervision during the course of this thesis. Their insightful feedback and constructive criticism played a crucial role in shaping the direction and quality of this work. Their guidance made the research journey rewarding and enjoyable.

Contents

Abstract

The evolution of mobile communication networks with the advent of 5G-NR introduces substantial improvements in data rates, latency, and reliability. In particular, the utilization of millimeter-wave (mmWave) frequencies in the Frequency Range 2 (FR2) spectrum band offers unprecedented bandwidth but poses significant challenges due to increased path loss, signal blockage, and limited penetration. To address these limitations, advanced beamforming techniques and intelligent beam management are essential. Existing beam management schemes, however, often fail to provide optimal Beam Pair Link (BPL) in dynamic environments. Location-Aided Beam Management (LABM) has emerged as a promising approach to enhance beam selection by leveraging User Equipment (UE) location data. When combined with a Radio Environment Map (REM), which contains site-specific propagation information, LABM promises to significantly improve mmWave link reliability and performance.

This thesis presents an end-to-end simulation of a REM-based LABM scheme for 5G-NR networks using the ns-3 simulator. The open-source Centre Tecnològic de Telecomunicacions de Catalunya (CTTC) 5G module that supports Non-Standalone Architecture (NSA) architecture and dual connectivity with Long Term Evolution (LTE) coordinator is extended by implementing a REM-based LABM algorithm. The study evaluates the impact of realistic UE location inaccuracies in REM construction and querying on the performance of the LABM algorithm in realistic channel conditions that are modeled using ray-tracing software.

1

Introduction

Mobile communications are undergoing a significant transformation with the advent of 5G-New Radio (NR), promising dramatic improvements in peak data rates and latency. The latest generation networks promise peak data rates in the Gbps range, up to 100 times faster than current LTE networks. Furthermore, 5G aims to deliver reliable 100+ Mbps speeds in urban areas and ultra-low 1 ms latency for critical applications. 5G-NR operates in two spectrum ranges: Frequency Range 1 (FR1) (400 MHz - 7 GHz), commonly used in mobile communications, and FR2 (24-53 GHz), also referred to as millimeter-wave (mmWave). While FR2 offers significantly larger bandwidths, it comes with increased challenges, such as higher path loss, limited penetration, and greater sensitivity to blockages. To overcome these issues and harness the full potential of mmWave communications, advanced techniques like beamforming and antenna arrays are essential. However, existing beam management schemes are often not able to provide optimal up-to-date BPLs for the mmWave link establishment in dynamic propagation conditions. The concept of LABM addresses this limitation by utilizing the knowledge of the UE location. In conjunction with location information, the REM plays a pivotal role in enabling environment-aware mobile communication. It facilitates more intelligent selection of BPLs based on site-specific channel propagation characteristics.

This thesis presents an end-to-end simulation of a REM-based LABM scheme for 5G-NR mmWave network implemented in the ns-3 network simulator. For the simulation of the novel LABM algorithm and selected scenarios, the open source CTTC 5G-NR compliant ns-3 module is extended to model the 5G NSA network [1]. The dual connectivity support implemented by the work of [2] allows sending and receiving control signals to and from a LTE coordinator. The ray tracing tool Wireless InSite is used to model realistic channel effects, allowing to acquire site-specific 3D spatial and angular channel performance. The simulated environment corresponds to an area located west of Frankfurt's main train station in Germany. Realistic pedestrian walk paths are generated using the commercial tool *Viswalk*. The impact of UE location errors in REM querying and location errors during REM construction on the performance of the implemented LABM algorithm is investigated. Various combinations of the available LABM algorithm parameters are tested in a set of scenarios. The algorithm's performance is evaluated in terms of the instantaneous Signal to Interference and Noise Ratio (SINR), link stability implied from the amount of Radio Link Failure (RLF) events and their duration, control signal overhead related to handovers, and Internet Protocol (IP)-layer throughput.

The remainder of this thesis is organized as follows: Chapter 2 addresses the theoretical background for 5G-NR and existing LABM schemes. Chapter 3 provides a detailed overview of the simulation setup and the implementation of the LABM algorithm in ns-3. Chapter 4 presents the system model and defines simulation scenarios that are selected to test the performance of the implemented LABM algorithm. Chapter 5 presents and discusses the

simulation results. Finally, Chapter 6 concludes the thesis and outlines directions for future work.

2

Background

In this chapter an overview of 5G New Radio (5G-NR) networks and their key distinguishing features from previous network generations are highlighted. Section 2.1 presents the requirements for new generation of cellular network, motivating and explaining the concept of mmWave communication with its advantages and challenges. Subsequently, the concept of beamforming in 5G-NR networks is introduced as a solution for challenging propagation characteristics of mmWave. Different types of 5G-NR network architectures are presented in Section 2.2. Some basic details of the 5G-NR Physical Layer of the OSI model (PHY) are described in Section 2.3. In the Section 2.4 control procedures and signals involved in 5G communication are explained. The available positioning frameworks for the UE localization in 5G-NR networks are presented in Section 2.5. In Section 2.6 beam management with additional information is presented, introducing existing approaches and the concept of the REM. Section 2.7 presents existing network simulators and their modules with the focus on those which were used for this thesis. Finally, the Section 2.8 presents existing efforts for the implementation of location-aided beam management and highlights the contribution of this thesis.

2.1 5G-NR Requirements and Technologies

As the amount of mobile users increases along with their requirements for higher data rates with low latency, the previous generation mobile networks had to undergo an evolution in their Radio Access Technology (RAT) and backhaul core components. Along with the expected evolution of the known use-case of serving mobile users with improved performance and seamless experience referred to as Enhanced Mobile Broadband (eMBB), new scenarios emerge with the rise of Massive Internet of Things (mIoT) and autonomous driving. Ultra-reliable and Low Latency Communication (URLLC) poses strict requirements for latency and availability. Such conditions are a must in intelligent transport systems, Vehicle-to-Everything (V2X), autonomous driving and teleoperations [3]. Furthermore, Massive Machine Type Communications (mMTC) is a new use-case for mIoT systems that require interconnection of massive amounts of devices that generate low data rate traffic with applications in smart-home, machine-to-machine and industrial monitoring.

The technical performance requirements in terms of data rates, spectral- and energy-efficiency, reliability, mobility, bandwidth require new technologies. 3rd Generation Partnership Project (3GPP) Releases 15 through 18 standardized the Massive Multiple Input Multiple Output (MIMO) system, which is able to improve spectral efficiency, capacity and signal quality by using a large amount of antennas, greater by an order of magnitude than what LTE systems are using [4, 5]. Massive MIMO increases the amount of served users at the same time. This is achieved through the simultaneous coverage of large number of users on the same time-frequency resources with the exploitation of spatial dimension.

The large amount of antennas in the Massive MIMO system provides higher resolution of the spatial distinction of radio signals, allowing to limit the transmission of data towards a narrow angular domain. Focusing the signal to a narrow angular domain results in a beam and is done with help of special signal processing steps that are covered in Section 2.1.2. In addition to that, Massive MIMO can be used for simultaneous transmission of multiple data streams towards a specific target receiver, increasing the signal quality and data rate. Experimental trial have shown that data rates of over 1 Gbps can be achieved [6].

In addition to MIMO, the usage of additional spectrum is a further solution for increasing network capacity. The sub-6 GHz frequency range is heavily congested because it has been allocated and exploited by earlier generations of mobile networks and other communication systems such as Wi-Fi, Bluetooth, satellite communications, Global Navigation Satellite System (GNSS) systems, broadcast television, radio, automotive and intelligent transportation systems. This heavy utilization led to the investigation of frequency bands above 6 GHz as an attractive alternative due to the significantly larger contiguous bandwidths available. The frequency range above 24 GHz offers bandwidth as wide as 400 MHz for 5G-NR networks [7]. As a result, the concept of mmWave communication with frequencies around 30-300 GHz emerged as a key enabled for 5G requirements.

2.1.1 Millimeter Wave

5G-NR defines FR2 in the mmWave bands, starting from 24.25 GHz [8]. The main challenge of using mmWave frequencies is their fundamentally different propagation characteristics compared to the sub-6 GHz frequency range that is used in previous network generations. Propagation of electromagnetic waves through free space imposes a loss in signal strength. Considering the order of magnitude of mmWave frequencies, the propagation loss of such signals is much higher than in sub-6 GHz bands. The reason for that can be seen from the relationship between the transmitted and received power under Line of Sight (LOS) that is given by the Friis equation:

$$P_{\text{loss}} = G_t \cdot G_r \cdot \left(\frac{\lambda}{4\pi R}\right)^2 \tag{2.1}$$

$$= G_t \cdot G_r \cdot \left(\frac{c}{4\pi f R}\right)^2 . \tag{2.2}$$

The Free Space Path Loss (FSPL) represents the attenuation of signal strength as electromagnetic waves propagate through free space. It is derived from the reciprocal of Friis' transmission equation [9]:

$$FSPL = G_t \cdot G_r \cdot \left(\frac{4\pi f R}{c}\right)^2 . \tag{2.3}$$

In both formulas G_t and G_r stand for Transmitter (TX) and Receiver (RX) antenna gain, λ is the wave length, f is the carrier frequency and R represents the distance between the TX and RX. c stands for the speed of light in vacuum. It can be seen that the loss is inversely proportional to both squared frequency and distance R. Considering the order of magnitude of mmWave frequencies, the path loss of such signals is much higher that in sub-6 GHz bands. As a result, mmWave systems have a fundamental limitation in the

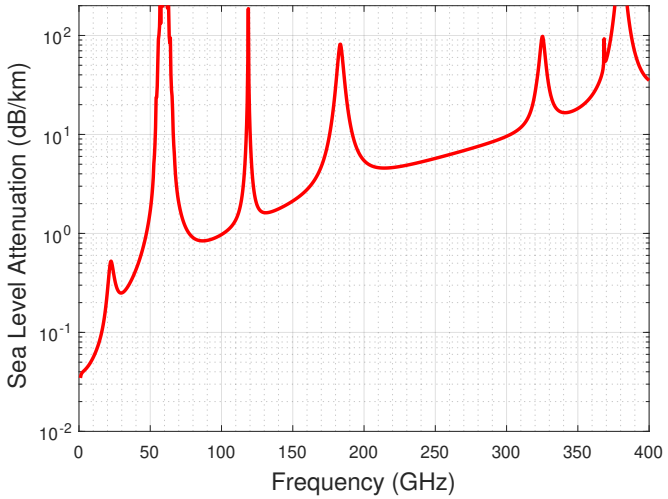

Figure 2.1: Atmospheric absorption across mmWave frequencies in dB/km based on the ITU-R P.P676 model [11].

operating range. Considering transmission power regulations, the range is typically a couple of hundred meters.

Furthermore, the atmospheric attenuation plays a much higher role in contrast to sub-6 GHz range. The Figure 2.1 shows peaks of attenuation at specific frequencies such as 60, 119, 183 GHz. The local minima can be observed in the range between 28-38 GHz, where the attenuation is 0.012 dB over 200 m at 28 Ghz and 0.016 dB over 200 m at 38 GHz, making them good candidates for carrier frequencies to be used in 5G-NR network deployments [10]. However, due to smaller cell size of around 200 meter in dense urban environments, the negative effect of other types of losses play a more significant role at mmWave frequencies [3, 10].

Shadow fading is a large-scale variation of the received signal strength. The main cause of shadow fading are objects on the path between the TX and RX with dimensions much larger than the wavelength. The effect of a shadow fade may last for seconds or minutes, occurring at a slower time-scale compared to the small-scale fading, which refers to rapid fluctuations of the signal strength [9]. Shadow fading may be caused by:

- Absorption of signal energy at the impacted object.
- Reflections, which cause the portion of the signal energy to be lost after impinging the encountered object and being reflected back.
- Scattering, which is a less uniform type of reflection. Scattering happens when the electromagnetic signal encounters large number of objects smaller or similar to its wavelength. This effects is caused by rough surfaces, small objects and irregularities such as street signs or lamp posts. Surfaces that typically act as reflectors for propagating waves experience diffuse scattering when their roughness getting closer to the wavelength. In extreme cases, rough surfaces scatter radiation uniformly in all directions.

Studies have shown that urban environments are primarily dominated by LOS propagation, while in Non Line of Sight (NLOS) conditions, reflections become the primary signal propagation mechanism [12]. The study performed by authors in [13] identified that the Friis path loss model fitted to measurement data from measurements at mmWave frequencies in urban and suburban locations delivered a shadowing factor varied between 3.5 and 6.3 dB. In NLOS scenarios, the path loss exponent significantly exceeded 3, with shadowing factors surpassing 10 dB.

Additional source of signal quality degradation are *penetration losses and reflections* from solid materials. Depending on the wavelength that is reflected from the impeding surface, the propagation characteristic change. It is shown by authors in [13], that such losses are dependent not only on the exact frequency used for mmWave communication, but also on material of the reflecting surface. Measurements at 28 GHz showed that outdoor tinted glass and brick pillars had penetration losses of 40.1 and 28.3 dB, respectively [10].

Multipath effect mainly occurs due to reflections from ground and objects in the environment and scattering [14]. Multipath is a small-scaled effect that causes rapid changes in the signal strength, random frequency modulation and time dispersion. As a result, the signal at the RX is a combination of several radio waves that arrive from different directions with different propagation delays. In mmWave frequencies in outdoor environments, this is the primary reception source in NLOS conditions [14].

2.1.2 Directional Communication

The previous section highlighted major factors that contribute to signal degradation in mmWave frequencies. However, their effect can be diminished with help of directional communication by focusing the transmission power towards the receiver to a narrow angular range. Multiple antennas can be combined at both TX and/or RX sides to create a phased antenna array. Due to the fact that mmWave allows the usage of smaller antennas, it becomes possible to install multiple elements even in the space-constrained user equipment such as smartphones. With such setup, an increased antenna gain may be achieved, improving the Signal to Noise Ratio (SNR) and reducing the delay spread due to multipath dispersion [15]. The spatial distribution of the output power is determined by the vector sum of fields radiated by individual antenna array elements. Weights that are applied to the array elements may be fixed or adaptive. For the case of adaptive weights, the main lobe of the antenna may be steered in the desired direction with arbitrary granularity. In practice and especially in mobile devices, the concept of codebooks is used, which contain a set of fixed weights that are applied to antenna elements. The codebook is thus containing a set of parameters that allow to focus the transmission and reception in predefined directions.

Depending on the exact place in the Radio Frequency (RF) chain where the weight are applied, one can differentiate between three types of beamforming. Applying weights using time delay elements of phase-shifting the signal before or after the upconversion on all antenna elements is known as*analog beamforming* and is presented in the Figure 2.2. The system essentially has a single RF chain connected to multiple antenna elements, but each signal for a specific element is manipulated using individual phase shifters. Adjustments of phase shifters steers the beam towards the desired angle, achieving high directional gain. Analog beamforming has low hardware complexity and power consumption, since only one RF chain is required. The limitation of such approach is that at a single time instance all

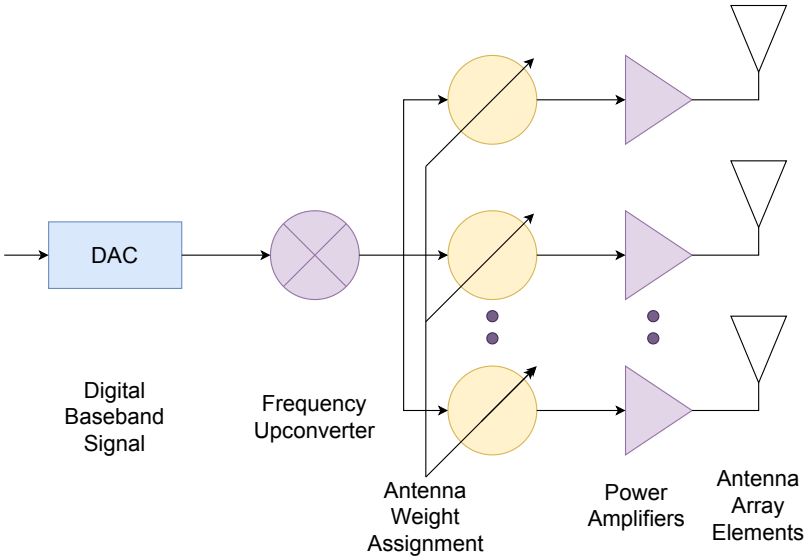

Figure 2.2: TX RF circuit for analog beamforming architecture. Adapted from [15].

antenna elements are used for the beamforming process. Thus, serving multiple users over different beams requires the Time Division Multiple Access (TDMA) scheme.

In contrast, *digital beamforming* uses a RF chain with Analog to Digital Converter (ADC), Digital to Analog Converter (DAC) and Digital Signal Processor (DSP) for each antenna element. The Figure 2.3 shows an example architecture for digital beamforming. Precise control over each element of the array becomes possible, allowing to form multiple individual beams simultaneously. Digital beamforming applies complex weights to each signal at the baseband level before upconversion. Such configuration allows greater flexibility for serving multiple users simultaneously with help of Multi-User MIMO (MU-MIMO) and high precision control over phase, amplitude and frequency in the digital domain. Alternatively, a single user can be served with several individual data streams over different multipath components - Single-User MIMO (SU-MIMO). The downside of the digital beamforming is the high computational complexity, high power consumption and overall complexity of the system, which make it unsuitable for mobile user equipment [15].

The *hybrid beamforming* combines the elements of analog and digital beamforming and its architecture is presented in the Figure 2.4. Within this setup, RF chains are connected to a subset of antenna elements, also called sub-arrays. Such architecture helps to lower hardware costs and energy consumption by reducing the amount of required converters and amplifiers. Hybrid beamforming generates signal streams for multiple users or beams in the baseband during the digital precoding phase. Then, precoded streams are routed to sub-arrays, where each sub-array then applies phase shifting to its stream, creating a beam. As a result, the hybrid beamforming enables the use of both MU-MIMO and SU-MIMO with less complexity and cost than digital beamforming.

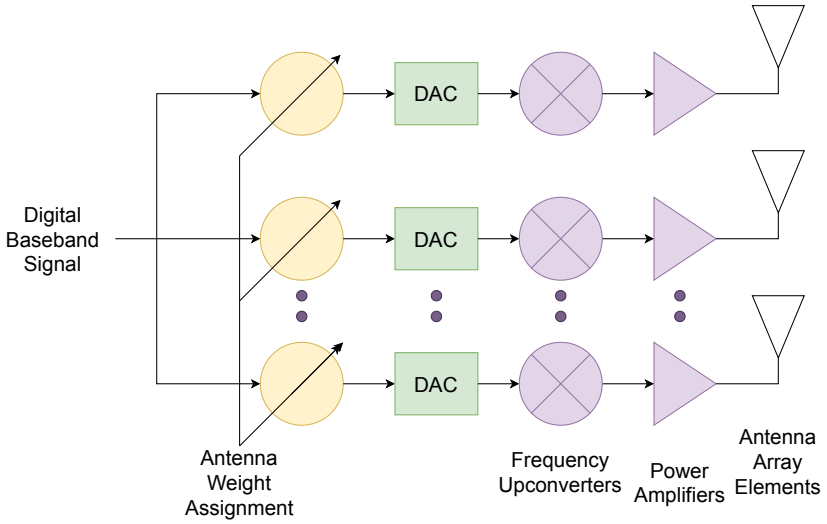

Figure 2.3: TX RF circuit for digital beamforming architecture. Adapted from [15].

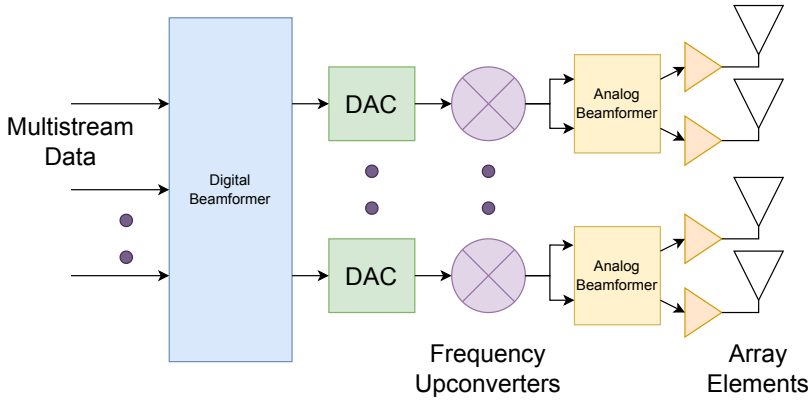

Figure 2.4: TX RF circuit for sub-array hybrid beamforming architecture. Adapted from [15].

2.2 5G-NR Network Architectures

The initial phase of 5G-NR was specified in the 3GPP Release 15, which defined main requirements for eMBB, URLLC, mIoT scenarios along with the definition of the NR interface [4]. 3GPP Release 16 defines enhancements for the URLLC, refines MIMO and introduces several improvements for the network slicing [8]. 3GPP Release 17 focuses on radio interface protocol architecture of NR connected to 5G Core [4]. The 5G core network offers a set of new characteristics such as Network Slicing, Mobile Edge Computing, Network Capability Exposure. 5G network consists of 3 main components:

- **UE**, which is a mobile station with a Universal Subscriber Identity Module (USIM).
- **New Generation Radio Access Network (NG-RAN)**, whose main entity is a Next Generation Node B (gNB). Main functions of gNB include radio resource management, admission control, packet scheduling, connection mobility control, routing of user-plane and control information to the 5G Core, measurement and measurement reporting configuration, Quality of Service (QoS) flow management, connection setup and release, scheduling and transmission of paging messages, scheduling and transmission of system broadcast information. NG-RAN node may also be represented by an New Generation Enhanced Node B (ng-eNB), which provides Evolved Universal Terrestrial Radio Access Network (E-UTRAN) user plane and control plane protocol terminations towards the UE.
- **5G Core Network (5GC)**, represented by entities responsible for managing idle state mobility, mobility anchoring, security, Protocol Data Unit (PDU) handling, PDU session control and IP address allocation. The 5GC relies on the Service-Based Architecture (SBA) framework, where elements are defined as Network Function (NF)s. They offer their services to all authorized NFs or other consumers. Such approach offers greater modularity, reusability and enables a virtualized deployment of NFs.

3GPP Release 15 defined two types of network architectures: the Standalone Architecture (SA) and NSA. The former means that gNBs are connected directly to the 5GC, not requiring any 4G network components for the proper operation. The later architecture combines 5G Radio Access Network (RAN) and existing LTE and Enhanced Packet Core (EPC) infrastructure. In NSA, the NR technology is available without changes in the core network. In such configuration, the control plane is still handled by the 4G LTE EPC. While 5G-NR provide faster radio interface, the services and features available to users are limited to what the 4G LTE core network can support, meaning that URLLC, mMTC are not fully enabled [4]. Network slicing and virtualization of core components is also not supported in such architecture. NSA is also known as Evolved Universal Terrestrial Radio Access New Radio Dual Connectivity (EN-DC) and may be considered a temporary step towards full 5G deployment. In NSA gNBs can be interconnected with 4G Enhanced Node B (eNB)s via the Xn interface and offer the 5G-NR capacities such as low latency and increased bandwidth [16]. The 4G radio network is used for control plane functionality such as initial access, paging and mobility management, while 5G NR provides user plane connectivity. Transmitting control data over the LTE connection enhances spatial coverage and accelerates control procedures by leveraging the high reliability and widespread

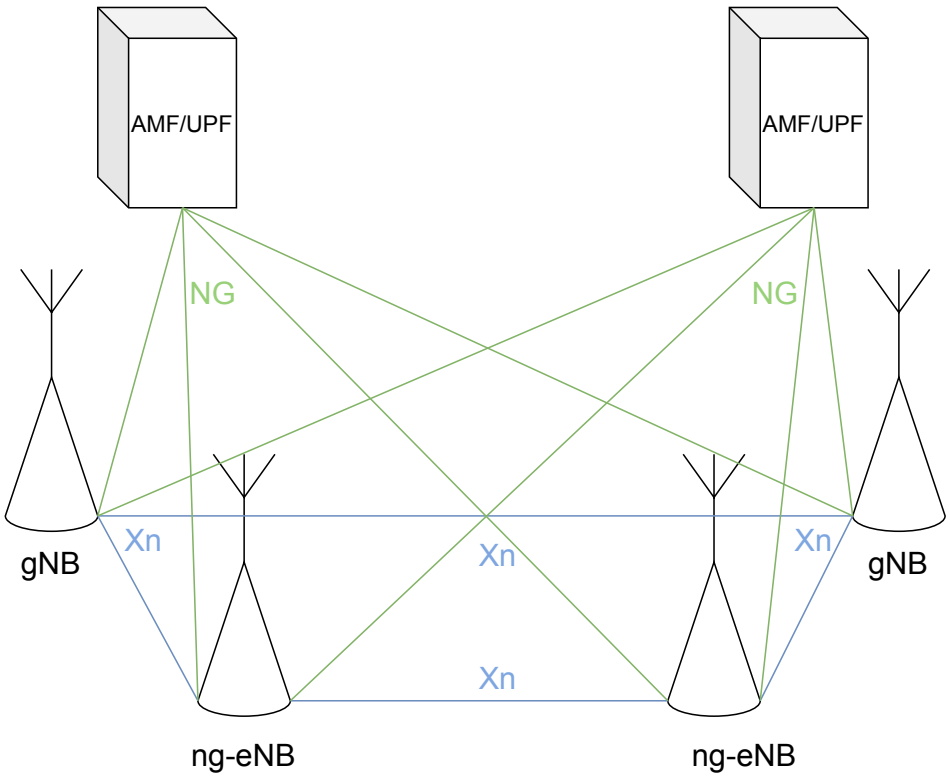

Figure 2.5: 5G-NR NSA architecture. Adapted from [16].

availability of the LTE radio link [17]. The simultaneous connection to both the 5G-NR gNB as well as the LTE eNB is referred to as Dual Connectivity (DC). Such setup enables a fallback mechanism, allowing the user data plane to switch to the LTE connection if the 5G radio becomes unavailable. An example of such NG-RAN architecture can be seen in Figure 2.5, where the mmWave gNBs and LTE ng-eNBs are interconnected via Xn interface and each of them is connected to the core network components such as Access and Mobility Management Function (AMF) by means of NG interfaces, and to the User Plane Function (UPF) by means of NG-U interfaces.

Several studies [18–20] compare the performance of SA and NSA architectures with focus on throughput, reliability, robustness, latency, beam management procedures and reactiveness on RLF events. Authors in [18] show that for the NSA the beam reporting delay is not higher than the LTE connection latency of up to 11 ms. Additionally, the authors observe that NSA architecture incurs lower overhead of beam reporting especially for analog beamforming. NSA scheme also offers reactive recovery for connected users in case of radio link failure events [18]. Additionally, the NSA facilitates centralized beam selection. By utilizing an eNB operating at sub-6 GHz frequencies, NSA-based beam association can consider real-time load conditions of nearby cells, ensuring fairer resource distribution across the entire cellular network [20]. Furthermore, the DC approach enabled by the NSA

allows faster path switching during mobility management procedures with help of a local coordinator, eliminating the delay of a hard handover and decreasing the packet latency [19].

2.3 5G-NR Physical Layer

5G introduces the concept of numerologies, which regulates the exponentially scalable subcarrier spacing and length of Orthogonal Frequency-Division Multiplexing (OFDM) symbols. 12 consecutive sub-carriers form a Physical Resource Block (PRB) and up to 275 PRBs are supported on a carrier. These PRBs are then used during scheduling of radio resources. Downlink (DL) and Uplink (UL) transmissions are organized into frames. One single frame has a duration of 10 ms and consists of 1 ms subframes. Each subframe consists of a variable amount of slots. Number of slots is governed by the numerology and varies from 1 to 16. Each slot consists of 14 OFDM symbols and a Cycling Prefix (CP) or 12 OFDM symbols with an extended CP [4].

A key characteristic of the 5G PHY is that it spreads over multiple frequency ranges. FR1 is defined as 410 MHz - 7125 MHz and FR2 as 24250 MHz - 52600 MHz [16]. FR1 includes bands inherited from previous 3GPP systems, which enable data rates similar to LTE and benefit from favorable propagation characteristics, allowing for omnidirectional transmission. FR2 range is introduced specifically for 5G-NR and supports Frequency Division Duplex (FDD) and Time Division Duplex (TDD) modes. In FDD, separate carrier frequencies are allocated for UL and DL, permitting simultaneous data transmission in both directions. In contrast, the TDD uses a single frequency carrier, alternating between UL and DL at different time intervals.

2.4 5G Control Procedures

The establishment of a mmWave communication link for data transmission between UE and gNB requires control-plane procedures such as initial access, Radio Resource Controller (RRC) signaling, beam management and measurement procedures. Exchange of control messages results in a successful attachment of a UE to a specific serving gNB with aligned directional beams that make the mmWave communication possible. However, due to the propagation characteristics of mmWave channels described in the previous sections, 5G-NR has to provide additional procedures to continuously monitor the channel and adapt to its current state. These tasks are performed by beam management procedures that include:

- **Beam sweeping** - sequential transmission and reception of reference signals on each available beam with pre-defined time intervals.
- **Beam measurement** - evaluation of the quality of the received synchronization signals at the gNB or at the UE.
- **Beam determination** - selection of the best suitable beam pair on UE and gNB side that maximizes the signal quality.
- **Beam reporting** - feedback from UE to the RAN about the beam quality and beam decision.

2.4.1 Initial Access

Idle users that are not connected to a serving cell have to perform the Initial Access (IA) procedure to get registered and get allocated physical resources that will be used for data exchange between the UE and the gNB. IA requires a synchronization procedure that involves the Primary Synchronization Signal (PSS), Secondary Synchronization Signal (SSS), Physical Broadcast Channel (PBCH) and DeModulation Reference Signal (DM-RS). All of those signals are packed into a block that is called a Synchronisation Signal Block (SSB). An SSB allows the UE to discover and synchronize with a gNB. For FR2, SSBs are transferred on separate beams, which allows measuring the signal quality with each possible combination of beams at UE and gNB. This process is referred to as beam sweeping. Subsequently, the UE is able to select the best BPL and report this to the gNB. After this exchange, the communication link over the best BPL can be established. Several frameworks for beam management during IA exist in 5G systems.

2.4.1.1 Standalone-Downlink (SA-DL) IA Scheme

The Standalone-Downlink (SA-DL) configuration the network consists only of 5G components and does not rely on the LTE overlay. The beam sweeping is performed by an exhaustive search where all possible beam pairs are explored by the gNB and UE. Beam measurements for IA are based on SSBs. The UE selects the beam that delivered the highest SNR value and chooses the corresponding sector for the link establishment. After beam determination, the UE waits for a Random Access Channel (RACH) opportunity from the gNB to send its RACH preamble. This procedure is presented on the sequence diagram in the Figure 2.6. The gNB must perform another complete sweep to receive all potential responses from the UE [21]. If the UE is not able to maintain mmWave control channel and the link can not be recovered based on available Channel State Information Reference Signal (CSI-RS) information, the UE repeats the IA procedure, during which the user experiences the service unavailability. For a single IA procedure the total duration is dependent on the period of the Synchronization Signal (SS) burst and number of UE antenna sectors. An SS burst refers to a group of SSBs sent within first 5 ms of the 5G frame with a configurable periodicity T_{SS} [22].

2.4.1.2 Non-Standalone-Downlink (NSA-DL) IA Scheme

The Non-Standalone-Downlink Architecture (NSA-DL) architecture allows speeding up the beam reporting phase with help of the sub-6 GHz overlay. The LTE connection can be used to report the optimal set of beams from UE to gNB, avoiding the additional beam sweep of the gNB for the allocation of RACH resources. This procedure is presented on the sequence diagram in the Figure 2.7. Reports on RLF events may also be sent over the LTE connection, speeding up the recovery of the mmWave link. The delay due to a complete sweep of the gNB and UE still remains and, ignoring packet loss and blockage, is the only factor that prevents a near-immediate attachment of the user device to the network. For an SS burst periodicity of 20 ms and an UE codebook of 10 azimuth sectors and 3 elevation sectors, the total sweeping delay adds up to 600 ms. Depending on the mobility and environment, such delay may cause prolonged service unavailability to the end user. It was shown that for a particular configuration of UE and gNB antennas using analog beamforming the IA may take up to 5 seconds [23].

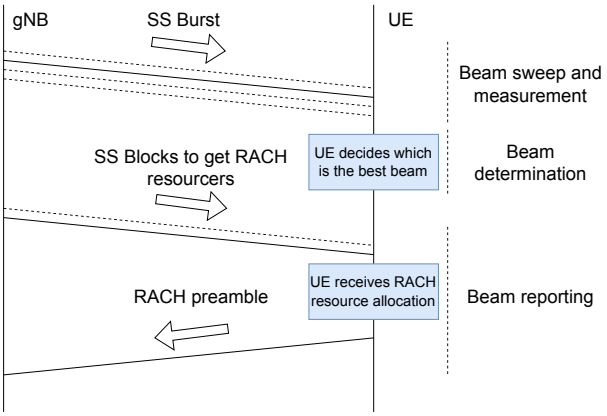

Figure 2.6: Signal and message exchange during the IA for SA-DL beam management. Adapted from [23].

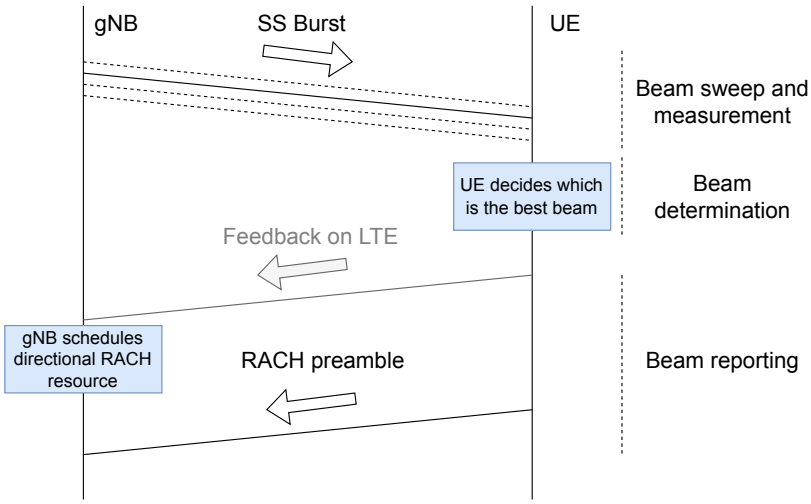

Figure 2.7: Signal and message exchange during the IA for NSA-DL beam management. Adapted from [23].

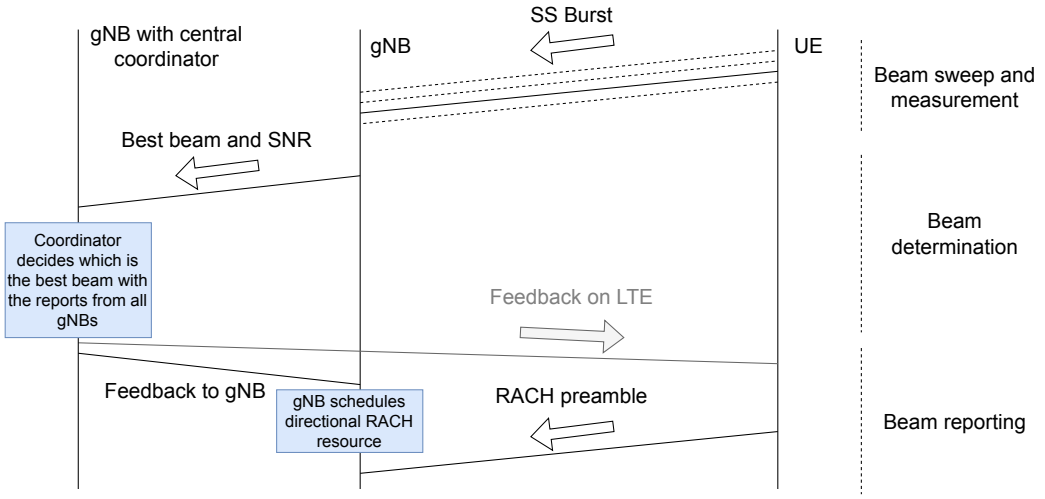

Figure 2.8: Signal and message exchange during the IA for NSA-UL beam management. Adapted from [23].

2.4.1.3 Non-Standalone-Uplink (NSA-UL) IA Scheme

The Non-Standalone-Uplink Architecture (NSA-UL) scheme is based on UL signals sent by the UE. Furthermore, the support of an LTE eNB as a central coordinator is required and the established LTE connection between UE and the coordinator is assumed. In such a configuration, the UE directionally broadcasts the Sounding Reference Signal (SRS) over mmWave frequencies while continuously sweeping over the angular space. A gNB scans all its angular space and monitors the signal quality of received SRSs. Thus, a report table is constructed for each receiving direction of the gNB. Once the table is filled, this information is sent by the gNB to the LTE eNB coordinator to accumulate the knowledge from all controlled cells about all detected UEs. As a result, the coordinator is able to detect the best beam pairs that provide maximum signal strength for each UE. This information is fed back to the UE over the LTE connection and to the gNB over the Xn interface. Thus, the gNB is able to schedule the directional RACH resource without an additional sweep compared to the SA-DL scheme. SSBs are not used in the NSA-UL scheme. This procedure is presented on the sequence diagram in the Figure 2.8.

2.4.2 Control Signals

This Subsection provides a brief overview of structure and functions of control signals that are used in 5G-NR.

2.4.2.1 Synchronization Signal Block

The structure of an SSB is presented in the Figure 2.9. An SSB carries the PSS, the SSS and the PBCH. SSBs are primarily used for IA for idle UEs, as they contain the most essential information about the PHY configuration of the network. SSB's PSS provides the

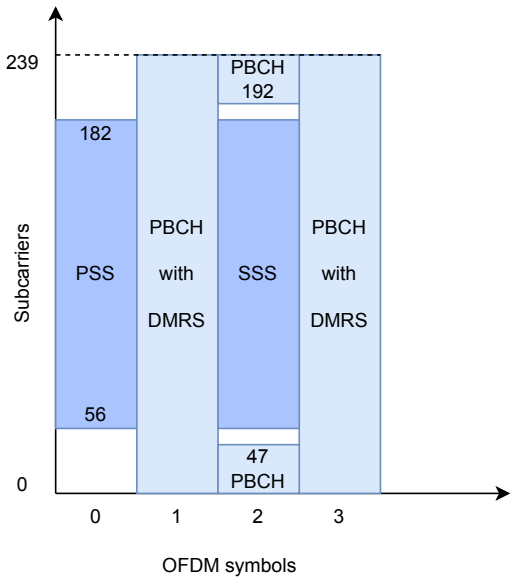

Figure 2.9: Structure of an SSB in time and frequency domain. Adapted from [23].

symbol-level synchronization and SSS provides the frame timing and cell ID. The PBCH carries the Master Information Block (MIB) that includes key system parameters such as System Frame Number, subcarrier spacing and SSB periodicity. An SSB consists of 4 OFDM symbols in time- and 240 contiguous subcarriers in frequency-domain [24]. An SS burst consists of several SSB that can be sent over different beams. Thus, at the receiver side, it becomes possible to measure the Reference Signal Received Power (RSRP) for a specific angular transmission. The maximum number of SS blocks in an SS burst is dependent on the used frequency [22,25]. SSB bursts can have different periodicity ranging from 5 to 160 ms and this parameter is controlled by the RRC [26]. When accessing the network, UE assumes the periodicity of SS bursts T_{SS} to be 20 ms.

For NR, the FR1 band allows the transmission of up to 8 SSBs every 20 ms. In the FR2 bands the maximum is defined as 64 SSB in a burst [24]. It has been shown that mmWave networks benefit from SSB configurations that allow to perform a complete sweep within a single burst of SS blocks [23]. That means that the optimal configuration would have the number of SS blocks being equal to the amount of possible beams at the gNB.

2.4.2.2 Channel State Information Reference Signal

CSI-RS are transmitted as DL control signals over Physical Downlink Shared Channel (PDSCH) from gNB to the UE, which is then able to assess the DL radio channel quality [27]. The most critical type of CSI-RS resource is Non-Zero Power (NZP) CSI-RS, which enables the UE to evaluate signals associated with specific beams. These measurements

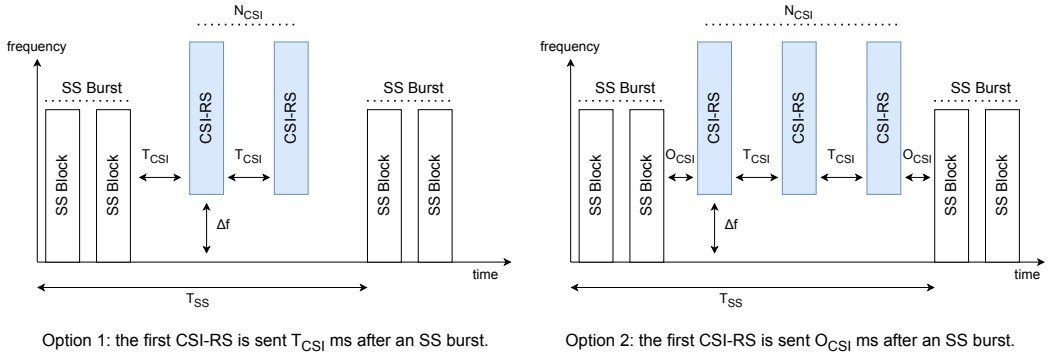

Figure 2.10: Two options for the CSI-RS scheduling with equidistant spacing T_{CSI} between transmission in Option 1, and reducing interval O_{CSI} between the last SSB and first CSI-RS signal in Option 2. Adapted from [23].

are used for Radio Link Monitoring (RLM) and can be utilized for link adaptation, beam refinement, and mobility management.

Limiting factor for the amount of CSI-RS messages is the T_{SS}, because signals are scheduled between SS bursts with either equidistantly spaced CSI-RS transmissions, or reduced delay between SS burst end and first CSI-RS O_{CSI} as can be seen in Figure 2.10. CSI-RS resources can be configured in three different transmission modes: periodic, semi-persistent, or aperiodic. In the periodic configuration, CSI-RS signals are transmitted at fixed intervals ranging in $T_{\text{CSI,slot}} \in \{5, 10, 20, 40, 80, 160, 320, 640\}$ slots, with the periodicity determined by RRC signaling [26]. The best beam can then be identified directly by looking at the highest signal quality of received CSI-RS. In semi-persistent mode the Medium Access Control (MAC) layer decides whether CSI-RS signals should be sent periodically or switched off. The aperiodic mode only enables individual CSI-RS signal transmission by using the MAC layer.

The ability to dynamically reconfigure CSI-RS resources ensures that the network can adapt to varying signal conditions, maintain link reliability, and enhance overall communication efficiency in 5G-NR deployments.

2.4.2.3 Sounding Reference Signal

The SRS is an UL signal transmitted by the UE.SRSs are essential for UL beam management as they allow the gNB to correlate the received sequence with a known reference signal and determines the attenuation and phase shift. The RRC layer specifies the periodicity and time-frequency resources for SRS, as well as directions in which the UE may send them.

2.4.2.4 Positioning Reference Signal

The Positioning Reference Signal (PRS) is a DL signal to facilitate support of positioning methods such as Downlink Time Difference of Arrival (DL-TDOA), Downlink Angle of Departure (DL-AOD) through a set of UE measurements and UE RX-TX time difference

[28]. The PRS supports the calculation of the geographical position of a UE to assist e.g. radio resource management functions and location-based services. The DL-AOD positioning method makes use of the measured DL-PRS-RSRP of DL signals received from multiple gNBs.

2.5 Positioning frameworks

First cellular positioning services were developed as early as in Global System for Mobile Telecommunications (GSM) networks and have significantly evolved with the addition of new control signals, procedures, algorithms and network components. Using more reference data for the position determination has helped to increase the accuracy of localization algorithms. The typical architecture and procedure of modern cellular positioning systems can be seen in Figure 2.11. As shown in the Figure 2.11, the procedure starts with a positioning request that originates either in the 5GC, or at the UE. In both cases, the AMF sends a service request to the Location Management Function (LMF), initiating the positioning procedure. The exact steps there depend on the positioning method used in the network. The result of the positioning procedure is then sent by the AMF to the initiator of the positioning request. 3GPP Release 17 defines the architecture for UE positioning, which involve the AMF, LMF, NG-RAN nodes [28]. The AMF receives and processes location service requests and forwards them to the LMF. The LMF is responsible for interacting with the UE or NG-RAN to obtain location-related data and transfers assistance data to the UE to support UE-based or UE-assisted positioning. The computed location estimate is then transferred back to the AMF. As a result, the AMF entity is able to provide the location service response to the 5G Core entity or assist other services that triggered the request. Positioning methods in modern networks can be classified into three categories:

- **UE-based**: using signals from GNSS satellites or radio measurements without relying on the network for computation. The network may provide assistance data, but the final position estimate is computed entirely by the UE.
- **UE-assisted, LMF-based**: UE collects and reports positioning measurements such as GNSS, PRS-based Reference Signal Time Difference (RSTD), or uplink timing to the LMF. The LMF processes the received data and computes the UE's final location, ensuring network control over positioning accuracy.
- **NG-RAN-assisted**: gNBs perform positioning measurements such as Angle of Arrival (AoA) or Time of Arrival (ToA) on UL signals from the UE. These measurements are sent to the LMF, which processes them to determine the UE's location, reducing computational overhead on the UE side.

5G proposed the usage of SRS signals not only for the channel state information provision to serving base stations as in LTE networks, but also for Uplink Time Difference of Arrival (UL-TDOA) and Uplink Angle of Arrival (UL-AOA) positioning methods. In addition to that, the DL PRS was designed for the UE positioning service for RAT-dependent methods such as Enhanced Cell-ID (E-CID), Observed Time Difference Of Arrival (OTDOA), Multi-Round-Trip-Time (Multi-RTT), AoA-based measurements. PRS allows the UE to estimate Angle of Departure (AoD) based of RSTD and report the results to the LMF.

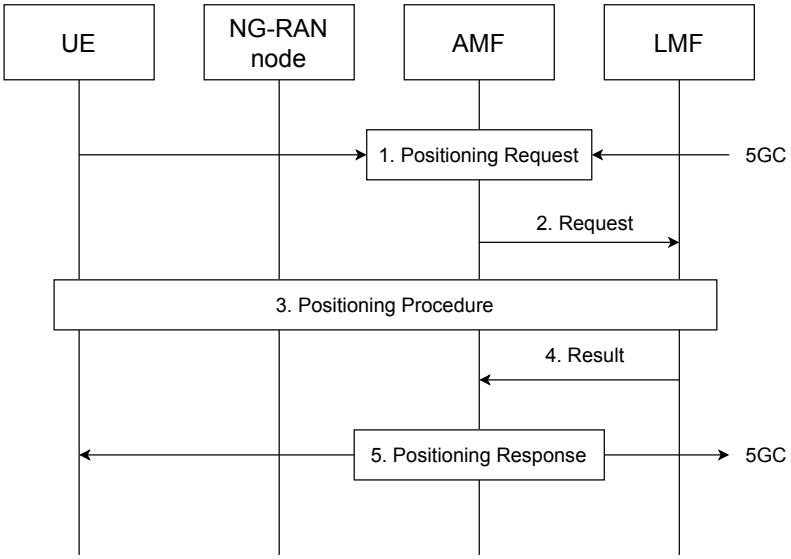

Figure 2.11: General location service procedure in 5G-NR. Adapted from [28].

2.5.1 LTE Positioning Protocol (LPP)

The LTE Positioning Protocol (LPP) defines the point-to-point communication between the location server and a target device to position it using measurements obtained from one or more reference sources as depicted in Figure 2.12 [29]. The source of location information may be the GNSS, the eNB with reference signals, or both. The measurements are then reported over the LPP to the location server, which is represented by the Enhanced Serving Mobile Location Centre (E-SMLC) or Secure User Plane Location (SUPL) Location Platform (SLP).

The LPP defines OTDOA, Assisted GNSS (A-GNSS) and E-CID positioning methods. The OTDOA method estimates the UE's location by measuring the Time Difference Of Arrival (TDOA) of PRS from at least three different gNBs/eNBs. Position is then derived from the relative arrival times of signals from different transmission points. The UE calculates RSTD and reports it to the serving gNB/eNB or LMF. The A-GNSS method allows the UE to request the assistance data from the LMF over LPP, which may provide satellite visibility, coarse time and position data as well as differential corrections. The UE is then expected to acquire the satellite signals faster for its GNSS-based positioning procedures. The E-CID method enhances the cell ID-based positioning by using timing advance, RSRP, Reference Signal Received Quality (RSRQ) and neighbour cell measurements. In contrast to OTDOA, E-CID does not require the usage of any additional signals, as the positioning data is extracted using existing radio measurements. However, the E-CID method is considered the least precise.

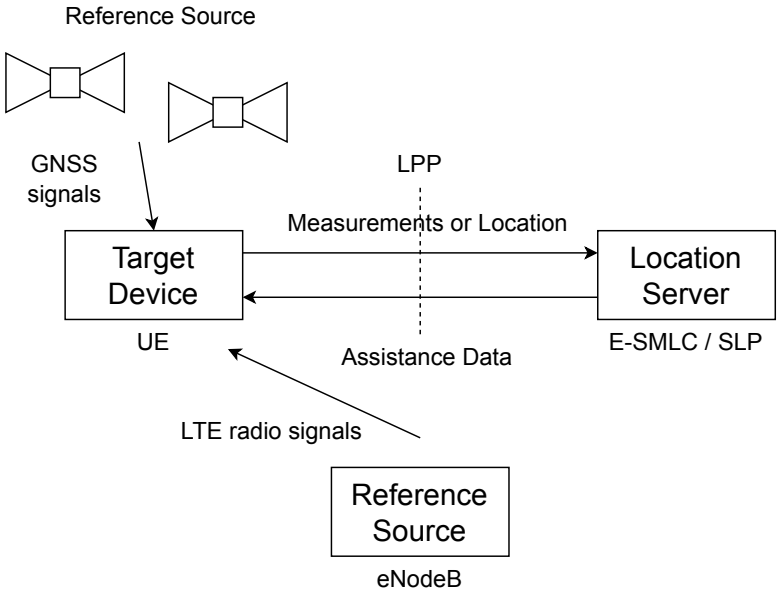

Figure 2.12: LPP configuration for control- and user-plane positioning in E-UTRAN. Adapted from [29].

2.5.2 NR Positioning Protocol A (NRPPa)

Unlike LPP, which defines the communication between the UE and LMF, the NR Positioning Protocol A (NRPPa) specifies the communication between gNBs and the LMF and is used exclusively for the core network signaling [28]. The NRPPa supports data collection processes for positioning-related traffic and operates exclusively on the control plane. NRPPa introduces the synchronization of RAN-based positioning signals such as PRS for UL SRS and UL-TDOA measurements and provides real-time coordination between multiple gNBs to improve positioning accuracy. NRPPa does not define any additional procedures and messages for the direct communication between the LMF and UE, but rather extends the LPP-based positioning services in the 5GC.

2.6 Beam Management with Additional Information

Maintaining perfect beam alignment during the communication is a difficult task due to the challenges of mmWave propagation and the dynamic mobile environment. In default 5G-NR deployments the network is not aware of precise UE locations and exact channel condition at every time point. Thus, the network has to perform beam sweeps and continuously monitor the channel state. SSB and CSI-RS are used to make this process possible, guiding the network in selection of correct BPLs according to performed measurements. In addition to that, lower frequency bands might be a further source of information for the mmWave beamforming process. As an example, the authors in [30] suggest leveraging the spatial information obtained from sub-6 GHz frequency bands to assist the beam selection process.

Lower frequency bands provide coarse AoA and AoD data that is used as input for the orthogonal matching pursuit algorithm, which helps to identify the optimal mmWave beam.

Modern smartphones and UEs are equipped with Inertial Measurement Unit (IMU), Global Positioning System (GPS), barometers, and magnetometers, which allow them to estimate their position and orientation. These sensors can be leveraged for location-assisted beam management, providing valuable information about UE motion trajectories and orientation to predict beam handovers before link degradation occurs.

However, pure location-based methods have inherent limitations, as GPS accuracy can degrade in urban environments due to multipath effects and obstructions, leading to errors on the order of tens of meters. For example, the GPS system might report positions within tens of meters of the actual position in highly urbanized environments. Such large positioning errors may lead to significant signal quality degradation and frequent radio link failures [31]. Additionally, location information alone is insufficient for robust beam management since it does not account for dynamic obstacles or real-time channel variations [32]. A multitude of studies have been performed trying to leverage various types of sensors that could be deployed on infrastructure side such as LiDARs, cameras that would track the actual physical environment over time. In such way the network would be able to keep a digital twin of the environment, helping to identify potential obstacles, predict blockages, and optimize beam selection proactively rather than reactively.

A key tool for improving the environmental awareness is a REM. REM is a site-specific database that contains georeferenced channel-related information [32, 33]. The REM provides information about the received signal power at different locations, helps identifying areas blocked by buildings trees or other obstacles. In addition to that, the REM allows to store information about the presence of LOS, number of paths with their propagation delays, AoAs and AoDs. Such information is highly valuable, as it enables the determination of optimal BPLs that result in the best signal quality at the UE and gNB. The construction of REM relies on multiple sources, such as pre-existing geographic databases and elevation maps, simulation-based ray tracing models that predict radio wave propagation, and empirical data from measurement campaigns. The offline REM construction offers a more cost-effective solution, but the quality and usefulness of data strongly depends on the granularity of the environment model and selected channel models. Ray-tracing-based simulation methods were shown to provide accurate propagation data and thus may be considered a viable tool for the offline creation of REM [34]. The REM can also be constructed and updated online by information from sources such as measurement reports of UEs about the currently used BPLs, keeping the knowledge about the environment as fresh as possible. One further option is using the offline method to provide a coarse estimation of the radio propagation environment and then refine it with help of online updates. An important aspect in the online construction and updates are localization errors that are introduced by uncertainties in positioning systems that provide location tags for collected spectrum measurements. Depending on the online update method and localization accuracy, the resulting spectrum measurement report might represent a location shifted by multiple meters from the real measurement point. In challenging channel propagation environments where the LOS between TX and RX is frequently lost, such localization inaccuracies might cause significant network signal quality degradation in REM-based beam selection algorithms in mmWave communications. A further challenge in REM handling might be posed by the granularity of data, size of the covered area and amount of captured information for each location. Depending on

those factors, the REM might become quite demanding in terms of required storage and processing resources. Thus, it is typically stored in centralized cloud-based servers, which are then accessed by network controllers.

2.7 5G-NR Network Simulation

Network simulators are widely used in research to evaluate and analyze the performance of communication systems in a controlled, repeatable, and cost-effective manner. They enable the study of network protocols, radio propagation models, mobility patterns, and interference effects without requiring expensive physical infrastructure. There are two main types of network simulators: discrete-event simulators and emulation-based simulators. Discrete-event simulators, such as ns-3, OMNeT++, model network operations at a high level, focusing on protocol behavior and system interactions over time. Emulation-based simulators, such as Mininet, interact with real hardware or software stacks to provide a more realistic representation of network behavior.

The network simulator ns-3 is an open-source discrete-event simulator that allows to evaluate protocols, routing and scheduling algorithms, network designs and traffic models without the need for physical hardware. ns-3 provides a set of software libraries that help to model specific aspects of communication systems. The user may then assemble the desired scenario by using those libraries as "building blocks" with desired parameters. ns-3 libraries in their current state contain modules to simulate Bluetooth, LTE, Transmission Control Protocol (TCP), User Datagram Protocol (UDP), Wireless Local Area Network (WLAN), mobility and related error models. Due to the fact that the code is open-sourced, user is able to extend or modify existing libraries to tailor the simulation scenario for his own needs.

With the standardization of 5G-NR and continuous testing and improvement of the new generation network, developer groups implemented new modules for ns-3 that simulate the mmWave propagation and the 5G network components. The work in this thesis extends the NR module provided by the CTTC [1]. It is based on the implementation from the New York University and University of Padova [35], but adds modifications that make the components compliant with the 3GPP 5G-NR specifications. The CTTC NR module enables end-to-end simulations of the complete 5G network. It reuses modules from the ns-3 LTE (LENA) module for all the higher level protocols such as Radio Link Controller (RLC), Packet Data Convergence Protocol (PDCP), RRC, Non-Access Stratum (NAS) and EPC [36]. As a result, the CTTC NR module represents the NSA implementation that includes 4G EPC and 5G RAN with the main contributions being:

- Extended configuration of the NR frame structure with support of numerologies.
- Orthogonal Frequency Division Multiple Access (OFDMA)-based access with variable Transmission Time Interval (TTI)s.
- Redesign of the MAC layer to include flexible MAC schedulers that consider time- and frequency-domain resources for TDMA and OFDMA-based with variable TTI.
- Bandwidth Part Manager.

The ns-3 CTTC NR module enables the end-to-end simulation, where the remote host is attached to the Service Gateway (SGW) and Packet Data Network Gateway (PGW).

SGW/PGW use the GPRS Tunneling Protocol (GTP) to encapsulate the packets. The GTP packet is received by the gNB over the IP connection and after decapsulating the payload, the packet may be transmitted over the RAN. The *NrGnbNetDevice* is the entry point to the mmWave channel. The packet is then received by the *NrUeNetDevice* on the UE side and passed to higher layers for further processing. *NrGnbMac* and *NrUeMac* classes implement the LTE Service Access Point (SAP) interfaces with "user" and "provider" roles, enabling further message passing to and from the RLC layer. *NrPhy* class is used to implement the directional communication for DL and UL.

In CTTC's module it is possible to divide the available bandwidth into Bandwidth Part (BWP)s, where each part can have its own PHY and MAC parameters such as numerology and scheduler strategy to multiplex services for different QoS traffic classes.

2.7.1 Physical Layer

The ns-3 LTE model supports FDD and defines subframes as two slots of 0.5 ms length. Seven OFDM symbols with CP are defined per slot. The ns-3 NR module's frame structure splits each subframe in the time domain into a variable number of slots with 14 OFDM symbols and CP defined per slot or 12 OFDM symbols with extended CP per slot. The amount of slots depends on the numerology, and makes their duration flexible. Furthermore, the CTTC module introduces the slot-level granularity in its processing controlled by *StartSlot()* and *EndSlot()* methods at both UE and gNB side, which are executed every 14 OFDM symbols. The first and last OFDM symbols are reserved for DL and UL control respectively, whereas other symbols can be allocated as needed. The processing delays of MAC-to-PHY layer is set to 2 slots and the gNB side and 100 μs on the UE side.

2.7.2 MAC Layer

The MAC layer was extended by CTTC to support the new OFDMA-based scheme with variable TTIs in addition to the TDMA and pure-OFDMA that was implemented for the ns-3 LTE module. The new scheme offers additional flexibility for the resource assignment, as it allows allocation of variable amount of OFDM symbols to different users within a slot. As a result, a more optimal resource allocation and lower latency can be achieved.

The *NrMacSchedulerNs3* class is the foundation for scheduling operations in the NR module, implementing UL and DL scheduling. For OFDMA-based scheduling, the procedure distributes OFDM symbols across multiple beam directions, as single-beam capability is assumed. Since analog beamforming limits transmission to a single direction at any instant, UEs requiring different beams must be served in separate time slots. The Ressource Block Group (RBG) allocation follows either an equal distribution between all UEs with the **Round Robin (RR)**, balanced throughput and fairness with **Proportional Fair (PF)**, or the **Maximum Rate (MR)** method that prioritizes UEs with the best channel condition. Once resources are assigned, Downlink Control Information (DCI) messages are generated. These messages ensure that RBGs assigned to different UEs do not overlap. All OFDMA schedulers operate using a variable TTI strategy, allowing them to define flexible TTI durations. For TDMA-based schedulers, it is directly determined how many OFDM symbols to allocate per UE.

2.7.3 Bandwidth Part Manager

The concept of numerologies adds an additional level of flexibility in the frequency domain. As a result, it becomes possible to support different slot lengths simultaneously on different sets of frequencies - BWPs. This configuration is done statically in order to define parameters for the PHY layer before the simulation starts. In contrast to LTE, where various carriers have the same OFDM symbol, subframe and frame boundaries, NR alligns only the subframe and frame boundaries of different BWPs. Everything else, including OFDM symbols, may be different. The MAC and Hybrid Automatic Repeat Request (HARQ) processes are individual for each BWP. The bandwidth part manager is then responsible for multiplexing of data based on traffic type and intended QoS rules.

2.7.4 Radio Link and Radio Resource Control

The RLC layer handles data transmission between the MAC layer and higher layers, providing error correction, segmentation, reassembly and retransmissions. The RLC layer is inherited from the LTE LENA module [36] and is based on 3GPP LTE RLC specification [37]. The RRC layer manages the connection between UE and gNB. It handles the transition between idle and connected states, establishes radio bearers for data transmission, supports handover procedures by managing cell selection and tracking area updates. The RRC configures Signaling Radio Bearer (SRB)s and Data Radio Bearer (DRB)s for control- and user-plane data, respectively. The RRC is also aware of channel quality from Channel Quality Indicator (CQI), RSRP, RSRQ from UE measurement reports that assist scheduling and mobility decisions.

2.8 Related Work

Directional communication is the key enabler for mmWave frequencies in 5G-NR networks. However, directional communication is not possible without beam management procedures that determine the optimal BPL during IA and track the signal quality to continuously update BPLs. As explained in previous Section 2.2, 5G networks can be deployed in several ways, affecting the way the IA procedure is performed. The authors in [23] investigate in detail possible network architectures that facilitate directional transmission and reception, concluding that the NSA deployment is the most efficient through faster reactivity to RLF events, higher experienced throughput and lower packet loss. This claim is supported by the work in [19], where authors show that the DC setup enabled by the NSA architecture helps to reduce the latency by up to 50% during handover events due to the availability of an additional LTE control link. Additionally, the probability of packet loss caused by overflow of PDUs during buffering was shown to be decreased for DC setup [19].

The authors in [38] suggest improved beam management strategies for 5G NSA-DL networks. They show that initially discovered BPL quickly become outdated due to the UE mobility if the BPL adjustments are solely based on information provided by SSBs from the beam sweeping procedure. The authors investigate the performance gains achieved by employing RLM with help of the CSI-RS signals, transmitted at higher frequency than SSBs. It was shown that the amount of RLF events is reduced in comparison to SSB-only beam management, improving the overall achievable throughput and increasing the link stability.

However, due to the fact that the more frequent RLM attempts to keep the connection to the current serving cell for longer, RLF events are still occuring.

One further challenge, is that specific network setups with higher amount of possible beam orientations may experience long delays before the beam sweeping procedure can be finalized. For example, the gNB and UE using analog beamforming with 64 and 16 beam orientations respectively, may take up to 5.2 seconds for the beam sweeping process, making it impossible to use in real-world scenarios with highly dynamic environment and moving receivers [23].

Location information is one of the key candidates for assisting the beam management process, as it provides additional information that may speed up the IA process and simplify beam tracking [39]. The main source of positioning information is usually assumed to be GPS data generated by the UE and transferred to the network over LPP. As the usage of NSA architecture provides a reliable LTE control link that can be leveraged for the transmission of additional data, it enables the transmission of positioning data to network core components. The authors in [40] perform a real-world test with off-the-shelf GPS and mmWave communication system to evaluate the position-aided beam alignment method. Authors investigate the performance of lookup table-, K-Nearest Neighbor (KNN)- and Neural Network (NN)-based approaches for the selection of most optimal BPL. The authors identify GPS inaccuracies to be one of the main reasons that make the learning process of selected models more difficult. The overall overhead saving of 70% compared to an exhaustive beam search was reported for 95% beam prediction accuracy. The authors in [41] leverage location information transferred over LPP in the NSA architecture to train Support Vector Machine (SVM)s for beam mapping by supplying the georeferenced SINR data. As a result, the IA latency was reduced by 38% with 11% reduction of control overhead. A neural network-based approach was suggested in [42]. It accepts position as input and provides a subset of estimated optimal beams as the output, resulting in an improvement of up to 10% in the received power ratio at the UE side. Aggregation of reported measurements with location tags is suggested by the authors in [43] and enables prediction of AoD information, which can then be mapped to a specific codebook entry and direct selection of a beam that should be used for communication. Thus, the knowledge of UE location was shown to contribute to a higher spectral efficiency and data transmission rates. The authors also conclude that a less accurate positioning is acceptable for UEs located further from the base station. The work in [44] has shown that the prior knowledge about AoD and AoA may help to avoid the channel estimation procedure completely and directly provide BPLs.

A further key component that is providing additional information for beam management procedures is the REM. The authors in [32] present the concept of REM and highlight its role as an enabler of environment-aware wireless communication, which contains geo-referenced channel-related information such as significant paths, AoD, AoA of the most optimal BPLs. Such as database is able to reflect the radio propagation environment, providing valuable context information to location-based beam management procedures. Several studies base their algorithms on the assumption of an available REM, that is queried at reported positions and either helps to refine the beam selection in a hierarchical manner [42, 45–48], or directly provide the optimal BPLs [31, 44]. The authors in [45] leveraged a database with georeferenced measurements and a hierarchical beam selection approach, where wider beams are selected based on previously reported measurements from the database and refined by scanning a restricted angular space. Such method helped to

achieve up to 9.5 dB higher antenna gain due to a better alignment of beams. The authors also demonstrated that the resolution of the database may be decreased with no significant degradation of network performance, saving the required storage resources. The authors in [46] leverage the sparsity and spatial correlation of mmWave channels. They use a database with a coarse knowledge of the channel state referred to as path "skeleton". Pilot signals are sent over the skeleton path to find the optimal BPL instead of performing a beam sweep over complete angular range. The authors demonstrated that their algorithm was able to reduce the effect of beam misalignment, contributing to a more stable connection. Furthermore, the interdependence of location errors and beam width was explored, showing that the usage of wider beams allows tolerating a higher positioning error. The work in [49] defined the beam management as a Markov Decision Process with Policy Iteration and a goal of maximization of RSRP and minimization of beam reselections. Authors assume the availability of a REM with RSRP measurements related to specific locations. During the communication process, they obtain the UE location from an external localization server and round it to fit to the closest point in the REM. The decision algorithm is then used to select the best BPLs. As a result, an improvement of up to 8.5 dB in the RSRP was achieved, while avoiding RLF events completely for some configurations of the algorithm.

As mentioned previously, the main source of positioning information is usually assumed to be GPS data generated by the UE. However, such service does not perform efficiently in urban areas due to blockage of its signal, significantly decreasing the localization accuracy. Thus, it is vital to consider the effect of positioning errors on location-aided beam management procedures. Previous paragraphs have already briefly mentioned that the positioning accuracy was identified to affect location-aided beam management algorithms. The authors in [31] investigated the importance of accurate modeling of realistic positioning errors. It was shown that modeling of correlated GNSS positioning errors modeled with the Ornstein-Uhlenbeck process has amplified the beam misalginment for highly urbanized scenarios. Another important aspect is that the construction of REM is also prone to positioning errors, as reported measurements get shifted from their original ideal location. The REM affected by measurement errors will be referred to as a *measurement REM*, and its error contribution amplifies the performance degradation of the network. As a result, realistic positioning errors were shown to cause a significant throughput degradation, up to 30% more outage events and up to 40% more frequent beam misalignments in comparison to the baseline with uncorrelated errors and ideal REM, unaffected by measurement errors.

The main building blocks for an efficient and precise beamforming algorithm that can be identified from previous works are the location data for the UE, beam-selection algorithm in a centralized network component, and a database that stores previous measurements. This thesis focuses on leveraging two sources of information for assisting the beam management process. Similar to the work in [31, 45, 46, 49], it is assumed that the REM is available in a centralized network component and can be used as a database for beam selection. The REM contains the channel data for each geographical location from each gNB, whose signal is received there. The source for the location information will be assumed to be the GPS module on the UE. In this work the focus will be made on the investigation of the effect of localization errors that affect the UE location reporting, as well the influence of error-affected *measurement REM* on the location-aided beam management.

To the knowledge of authors, there are no implementations of location-aided beam management algorithms in ns-3 that investigate the end-to-end 5G-NR network perfor-

mance. Thus, this work provides the possibility to simulate REM-based location-aided beam management algorithm that is able to model the contribution of errors caused by imprecise UE localization and REM querying errors. The work in [2, 50, 51] is used as the initial state of the code base. The authors in [2] implemented the realistic 3GPP compliant beam management procedures and incorporated the dual connectivity capability for the NSA-DL network architecture. The authors in [50] extended the work from [2] to include the support the simultaneous simulation of multiple UEs. The authros in [51] have implemented a flexible RLM procedure that allows to monitor candidate BPLs from other candidate gNBs and not only from the serving one. However, these RLM capabilities are not explicitly used for this thesis. The work in [51] is rather used as the initial state of the code base for further extensions for the implementation of the location-aided beam management scheme. With the addition of REM-based beam selection algorithm in this thesis, an extension of ns-3 simulator is presented, that is able to perform pure REM-based beam management with realistic GNSS error models applied to UE location information.

3

Simulation Framework

In this thesis the full-stack ns-3 framework extensions are based on the work in [2, 50, 51]. The authors in [2] implemented a 5G standard-compliant beam management procedure for the 5G-NR NSA mmWave network based on the CTTC 5G-NR module. The state was extended by authors in [50] to support simultaneous simulation with multiple users and uses a ray-tracing model for capturing realistic mmWave channel effects. The authors in [51] extended the simulator with a coordinator-based RLM framework for multi-user DL mmWave networks that allows monitoring candidate BPLs from other candidate gNBs and not only from the serving one.

Similarly to [51], the LTE Coordinator eNB node that assists specific control procedures in the network of mmWave gNBs is assumed to be present in the network. The DC feature implemented by the authors in [2] allows to exchange RRC messages between the UE and an LTE eNB. The current state does not model the actual message transmission of RRC PDUs over LTE PHY. UEs are connected to the LTE coordinator node, which is the only network entity that stores the REM of the simulation area and hosts the algorithm that manages the LABM operations. The main modifications required for the implementation of LABM relate to PHY and RRC layers of UE and gNB classes.

In Section 3.1 an overview of the changes introduces to the ns-3 classes in PHY and RRC layers is provided. This section also explains the implementation of the REM and error model that is applied to UE mobility data. Section 3.2 introduces the flow diagram and details of the implemented LABM algorithm. Additionally, this section describes and visualizes the relation between antenna orientation parameters and orientation of resulting sectors in azimuth range in the Global Coordinate System (GCS). In Section 3.3 the additions to the tracing system of ns-3 are described.

3.1 Modifications to ns-3 NR and LTE modules

The overview of affected and related classes for the LABM algorithm can be seen in Figure 3.1. The UE and gNB include their own instances of PHY, MAC, and RRC entities, interconnected by SAPs. SAP classes such as the *LteUeRrcSapUser*, the *LteUeRrcSapProvider*, the *LteEnbRrcSapUser* and the *LteEnbRrcSapProvider* allow the UE and LTE Coordinator (CO) eNB to exchange control information. Interfaces between RRC and PHY classes are implemented in the class *LteUeCphySapProvider* and the *LteEnbCphySapProvider*, allowing to adjust beamforming vectors for corresponding target UEs and gNBs according to information provided by the LTE coordinator, referred to as beam commands. The *LteEnbRrc* class of the LTE coordinator node is responsible for the management of LABM algorithm logic and hosts the REM.

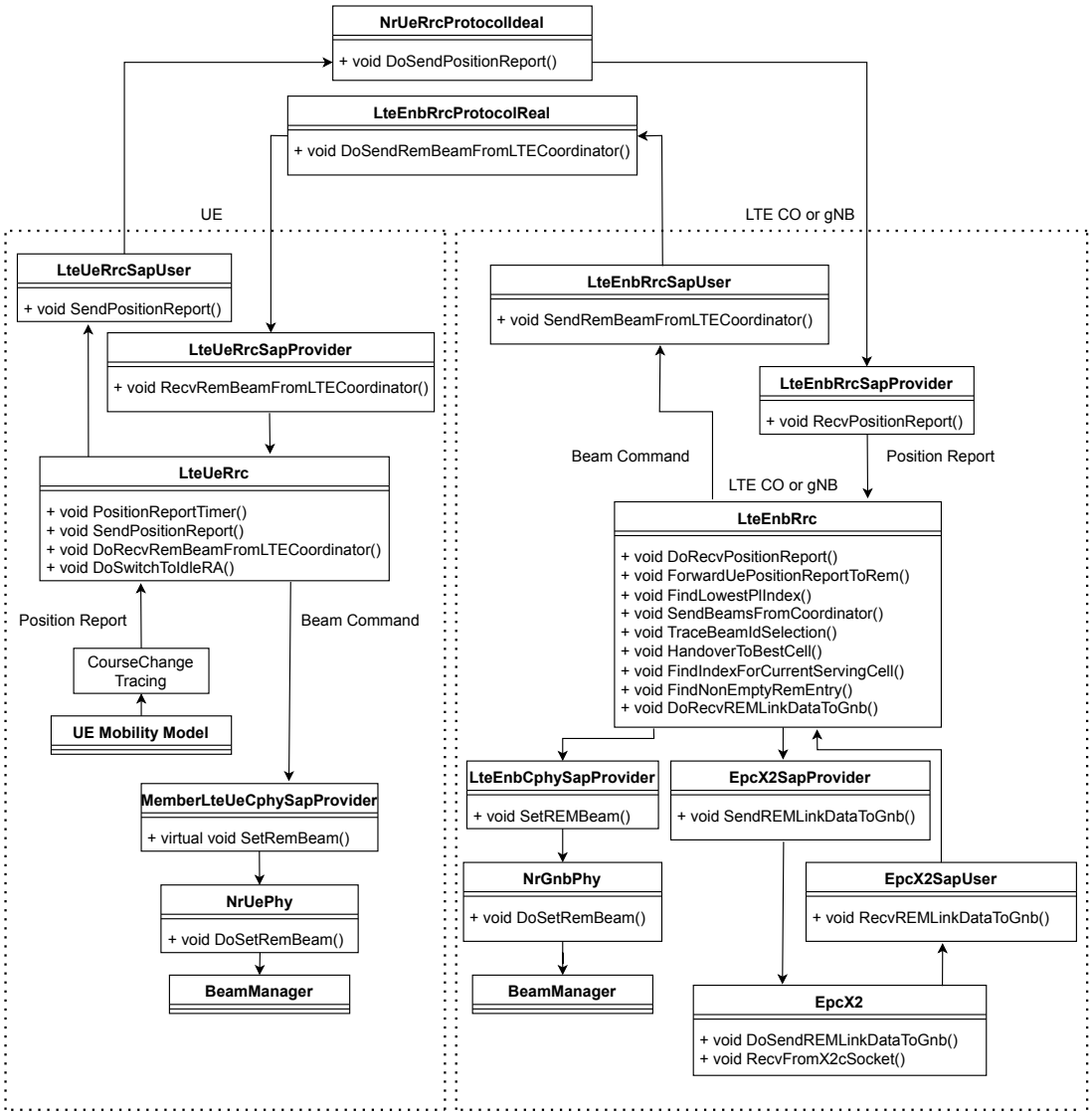

Figure 3.1: Structural overview of ns-3 classes related and extended for LABM algorithm.

3.1.1 Modifications to the PHY Layer

3.1.1.1 NrPhy

NrPhy provides base functionality for the UE and gNB PHY layers. Its main tasks include managing the slot allocation, control messages and processing of MAC PDUs. The *NrPhy* class configures the fundamental PHY parameters such as amount of slots in a subframe, slot length, numerology, subcarrier spacing and symbol duration. In addition to that, its members are responsible for antenna configuration and beam management. The *BeamManager* instance manages beamforming vectors for the antenna. Each beam is represented by a set of complex weights mapped to a beam ID. The *BeamManager* allows configuring and saving beam IDs that are meant to be used for communication with specific *NetDevice*, where a *NetDevice* represents a network interface that is connected to a UE's or gNB's radio interface. Additionally, the *NrPhy* class manages the RLM process by keeping track of beams to be monitored by UE and gNB in the *m_noOfBeamsTbRLM*, *m_noOfBeamsTbReported* variables and the per-International Mobile Subscriber Identity (IMSI) vector for beams to be monitored in *m_beamsTbRLM* [51].

3.1.1.2 NrGnbPhy

The *NrGnbPhy* and *NeUePhy* classes are derived from the *NrPhy* class. Both classes were extended with new methods that are able to change and save beamforming vectors of network devices through the *NrPhy*'s instance of the *BeamManager* class.

The *DoSetREMBeam* methods shown in the Figure 3.1 are responsible for receiving the commanded beam ID from the LTE coordinator and using them for communication with the specific UE or gNB. The *NrGnbPhy::DoSetREMBeam* method fetches the *NetDevice* which corresponds to a specific IMSI. Then, *NrGnbPhy::m_sectorDegreeMap* and *NrGnbPhy::m_elevationDegreeMap* are used to map the azimuth and elevation angle to a corresponding antenna sector, producing the *BeamId* structure, that can be passed to the *BeamManager* class instance. If the gNB is already using this *BeamId* for the communication with the specific UE, the *NrGnbPhy::DoSetREMBeam* method terminates. When the *BeamManager* receives a *BeamId*, it converts it to a *BeamformingVector* and passes to *BeamManager::SaveBeamformingVector* method along with the target *NetDevice* that represents the intended receiver or transmitter. The *BeamManager* updates the appropriate entry of its *m_beamformingVectorMap*. As a result, the underlying antenna array receives complex weights that need to be applied for the communication with specific target device.

LABM algorithm takes the full control of the beam selection process on both gNB and UE sides during the communication, excluding cases where IA has to be performed as a fallback if the LABM algorithm fails. Thus, for the purpose of investigating the performance of the LABM scheme, the queueing of CSI-RS signals is disabled. *NrGnbPhy::DICtrl* method with help of the *m_useLABM* variable. As a result, CSI-RS messages are not sent by gNBs.

3.1.1.3 NrUePhy

The *DoSetREMBeam* method of the *NrUePhy* class needs a slightly different implementation due to additional case differentiation that depends on the IA procedure. The procedure

on the UE side is slightly different, as the UE might be in the IA state. This happens in the beginning of the simulation and after a RLF event. If the UE is undergoing the IA procedure represented by *m_IAperformed* being set to *true*, it can be concluded that the UE is not connected to a gNB. Due to the fact that the UE is periodically receiving a beam command from the LTE coordinator that also contains the information about the best serving gNB, the UE does not need to continue the beam sweeping process to determine the best gNB candidate. Thus, the IA procedure is directly aborted by setting *m_IAperformed* to *false*. After that, similarly to the process in *NrGnbPhy*, the beamforming vector is created and saved for the target serving cell by changing the *m_currBeamformingVector* for the *m_registeredEnb* entry that corresponds to the target gNB. Finally, the UE has to be transferred to the *Connected* state of its RRC state machine. This is done by calling the *SwitchToIdleRA* method that will switch the UE RRC state to *IDLE_RANDOM_ACCESS* if the current state is *IDLE_START*, which is the case in the beginning of the simulation or when an outage takes place. If the state change was successful, the connection to the gNB is progressed with the *ReEstablishConnectionWithCell* method, which sets the target gNB *NetDevice*, notifies the MAC layer to start the Random Access (RA) procedure and clears existing handover events at the LTE coordinator. Additionally, the variables related to RLM have to be initialized. This is done via the new *RlmInitAfterRemIA* method that initializes the *NrUePhy::m_beamsTbRLM, NrUePhy::m_txSSBCounterPerRx* as well as *NrUePhy::m_ssbRMCounter* variables and deactivates the IA state of the *NrSpectrumPhy* class by calling *m_spectrumPhy->SetIAState (false)*. Lastly, the SSB Processors are created for each available gNB in the simulation by inserting into the *NrUePhy::m_cellIDSSBMap*.

If the UE was not performing the IA procedure when it received the BPL information from the LTE coordinator, it follows the same procedure as described in the Section 3.1.1.2.

The *NrUePhy::UpdateSinrEstimate* method was adjusted to prevent initiating a sweeping procedure. Whenever the currents SINR level for the serving cell is detected to be lower than the *m_beamSweepThreshold*, the UE would increment a counter. If the counter value surpasses the *m_n310* threshold that is set to 2 events, the IA flag might get set, which will initiate the beam sweeping and cell search procedure. When the LABM algorithm is enabled, the UE should instead wait for information from the LTE coordinator. Thus, the processing is aborted as soon as the current SINR is detected to be below *m_beamSweepThreshold*.

3.1.2 Modifications to the RRC Layer

The RRC layer is the key for transmission of UE location reports, BPL information and it also hosts the LABM algorithm. This layer is represented by the *LteEnbRrc* class adapted from the LTE LENA to support the 5G-NR NSA architecture. Interaction between gNBs and the LTE coordinator happens through the X2 interface, allowing the information exchange between all base stations and consequently enabling the beam commanding to mmWave gNBs. The *LteEnbRrc* class is responsible for mobility management, RRC connection establishment, reconfiguration and handovers. With the extensions of the RLM implemented in [51], the LTE coordinator is also aware of existing UE connections to gNBs and signal quality levels, which are also relevant for the LABM algorithm.

With the current state of implementation of the DC scheme, the communication between the UE and LTE eNB happens over the *ideal RRC protocol model*. This means that the connection is established at the beginning of the simulation and is available without in-

terruptions throughout the whole runtime. This also means that all RRC messages are transmitted by directly scheduling the reception of the corresponding message, without the actual transmission of RRC PDUs over MAC and PHY layers of the LTE connection and without any delay. The LTE coordinator is represented by an additional connection via SAP. The UE is able to send its messages via the *nrUeRrcProtocolIdeal::m_lteEnbRrcSapProvider*, which represents the RRC connection to the LTE coordinator, whereas *nrUeRrcProtocolIdeal::m_enbRrcSapProvider* is responsible for the connection to gNBs.

The *LteEnbRrc* class is re-used as the RRC layer for both LTE coordinator eNB and gNB nodes. Thus, the same class contains mixed set of member variables and methods to support both use-cases. In the LTE coordinator role, the UEs have an Radio Network Temporary Identifier (RNTI) assigned to each of them, and each has a corresponding entry in *m_lteRnti* map, that keeps track of mapping between IMSIs and RNTIs. In contrast to that, the *LteEnbRrc::m_imsiRntiMap* keeps track of the 5G-NR RNTIs used for connections to gNBs.

In order to support location reporting from UEs over the LTE RRC connection, the *LteEnbRrc* class was extended with new methods and member variables. Firstly, the *PositionReport* structure in *lte-rrc-sap.h* was added to store the UE IMSI, current serving gNB ID and the *ns3::Vector3D* that contains x,y,z coordinates of the UE's location from its mobility model. This data structure is used to inform the LTE coordinator about the UE's location in each reporting step. The actual location updates are fetched from UE's mobility model's tracing source *CourseChange* and then forwarded to UE's RRC layer. *LteUeRrc::SendPositionReport()* receives the tuple of x,y,z coordinates and prepares a *LteRrcSap::PositionReport* structure. The report is sent if the newly added Timer *m_positionReportPeriodSeconds* has expired. Its period is configurable via the attribute *PositionReportPeriodSeconds* and defines how often UE location reports are sent to the LTE coordinator. This allows to subsample the reporting from the frequency in the UE's mobility model to values that are closer to consumer-grade GNSS modules installed in typical smartphones.

3.1.3 Radio Environment Map

ns-3 provides a REM module that manages UE and gNB *NetDevice*s and stores SNR, SINR, Interference Power Spectral Density (IPSD) values at each REM point, that represents a unique location [52]. The 5G-LENA REM module introduces the *NrRadioEnvironmentMapHelper* that receives channel condition model, propagation loss model and keeps information about nodes such as *NetDevices*, *MobilityModels* and *AntennaArrayModels* in the *NrRadioEnvironmentMapHelper::RemDevice* structure. REM entries are represented by the *NrRadioEnvironmentMapHelper::RemPoint* structure that stores location, average SNR, SINR and IPSD values. Overall, the module helps to provide valuable insights into the channel state and allows visualizing it in form of coverage and beam shape maps. However, the *NrRadioEnvironmentMapHelper* does not provide methods to perform REM queries during the simulation runtime. Moreover, available structures do not convey detailed-enough information about AoD and AoA from specific gNBs for each possible location of the receiver. Such information is crucial for the LABM algorithm, but it can not be provided by the 5G-NR REM module from CTTC.

One important aspect in the code from work in [51] is that instead of 3GPP channel model, a ray-tracing channel model is used to acquire realistic site-specific propagation data.

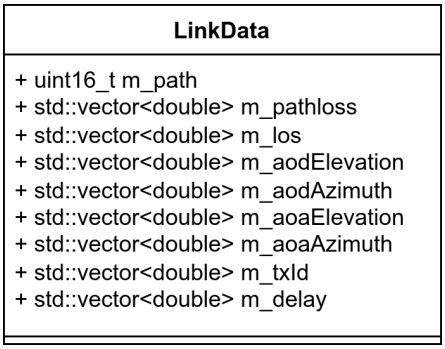

Figure 3.2: *ns3::LinkData* structure that represents a single REM entry on a specific grid point.

This allows to achieve higher accuracy in spatial and angular domains, allowing a more realistic end-to-end simulation of the 5G-NR network. The ray-tracing channel model is represented with help of the *ns3::LinkData* structure. It is used for PHY layer computations in the *ThreeGppChannelModel* class. The content of the *ns3::LinkData* structure can be seen in Figure 3.2. This structure represents the propagation data from all TX devices for a single location of the RX device with following meaning for each field:

- ***m_path*** - Number of paths.
- ***m_pathloss*** - Path loss in dB of each path.
- ***m_los*** - Line of Sight information for each path.
- ***m_aodElevation*** - Departure elevation angles in degrees for each path.
- ***m_aodAzimuth*** - Departure azimuth angles in degrees for each path.
- ***m_aoaElevation*** - Arrival elevation angles in degrees for each path.
- ***m_aoaAzimuth*** - Arrival azimuth angles in degrees for each path.
- ***m_txId*** - Cell ID of transmitting gNB for each path.
- ***m_delay*** - Delay spread in nanoseconds for each path.

As can be seen from the list, the *ns3::LinkData* structure provides per-path information about AoA and AoD, and it also contains the corresponding path loss value and the gNB cell ID. This data allows identifying the best path in terms of path loss and can be easily mapped to a specific antenna sector of a selected gNB. This completely satisfies the input requirement for the LABM algorithm. Thus, it was decided to re-use the *ns3::LinkData* structure for the representation of a REM. A single entry of the REM is represented by the *ns3::LinkData* instance, paired with the *ns3::Vector*, which represents the location of the REM entry in Cartesian coordinates in GCS.

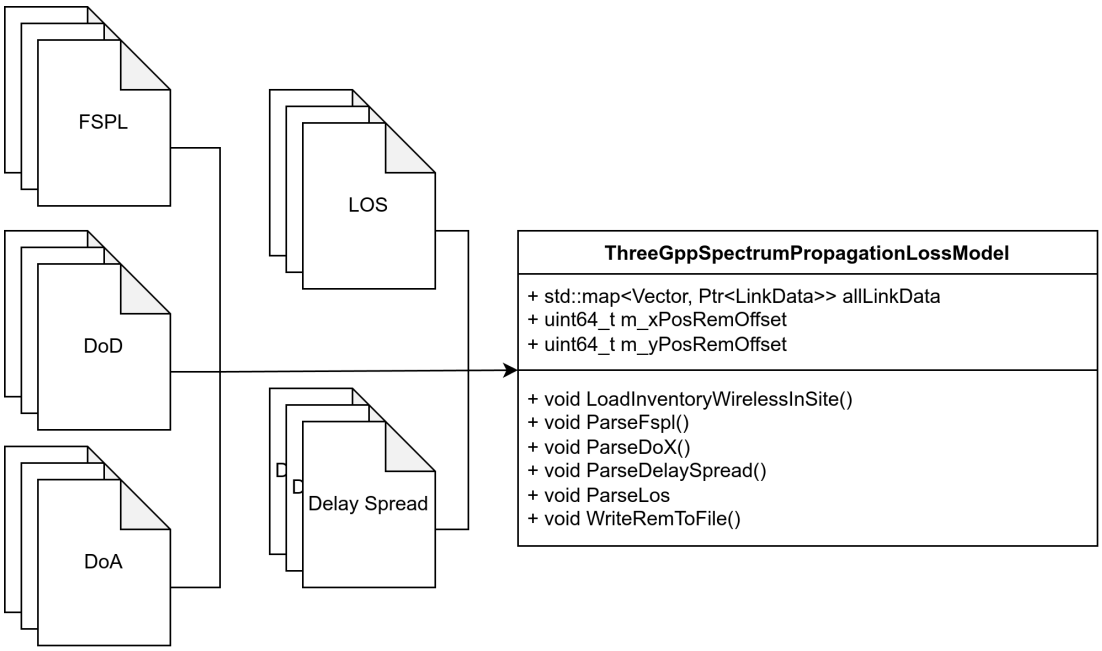

Figure 3.3: Relevant files and methods for parsing Wireless InSite REM data.

3.1.3.1 REM Parsing

The *ThreeGppSpectrumPropagationLossModel::allLinkData* member variable stores an instance of *ns3::LinkData* for each location of the simulated area. Thus,it is possible to store the channel state data for a particular setup of gNBs in a given topology for each geographical location. The data was originally generated with ray tracing software implemented by authors in [53]. Reading of ray traycing data was implemented by setting the *RaySourceType* attribute to the value *Inventory*. This would result in a call to the *LoadInventory* method of the *ThreeGppSpectrumPropagationLossModel* class, that would read the input file and instantiate the *ns3::LinkData* structure for each defined location. The inventory is a file that contains the entries of *ns3::LinkData* structure for each location on the simulation area. Thus, inventory file provides the required information for calculations of channel parameters in the PHY layer.

The tool in [53] was replaced by the Wireless InSite software to create a site-specific 3D wireless propagation data. Thus, it was necessary to modify existing procedures of loading the propagation data to support data generated by the Wireless InSite. One of the major differences in working with the Wireless InSite data is that Direction of Departure (DoD), Direction of Arrival (DoA), FSPL, delay spread, TX and RX power are generated separately for each gNB. Thus, the parsing method had to be extended in such way that it is possible to read multiple files and combine them all into a vector of entries for each of the *ns3::LinkData* fields. Figure 3.3 shows relevant files, new members and methods that were added to the *ThreeGppSpectrumPropagationLossModel* class, which is originally responsible for loading the inventory file.

Apart from simple parsing of files, a few changes of how exactly the data is interpreted were necessary. The original inventory file inherited from the work in [51] had several conventions in terms of ranges of values for elevation and azimuth data. Azimuth values are expected to be in the range $[0, 360)$ degrees, whereas Wireless InSite provides them in $[-180, 180)$ degrees. Elevation values in the original inventory file are negative for the cases when the ray is pointing downwards in relation to the horizon, whereas Wireless InSite provides values larger than 90 for that direction. Thus, both elevation and azimuth parsing had to be normalized before writing the data into the *ns3::LinkData* structure. Additionally, the interpretation of LOS data had to be modified. Default inventory defines value 1 as LOS, 2 as NLOS, whereas Wireless InSite had 1 for LOS and 0 for NLOS. Further challenge was the fact that path loss values were not provided per-path in Wireless InSite files. This is a critical downside, as this make it impossible to differentiate the signal quality between several paths of a single gNB, which is the basic building block for the LABM algorithm. As a workaround for this problem it was decided to calculate the path loss from the known and fixed transmission power of a gNB and the received power value, that is available for each path in the DoA and DoD files. To make this possible, a new member variable *m_txPower* was added to the *ThreeGppSpectrumPropagationLossModel* class to represent this parameter for all gNBs in the simulation.

Another important aspect in Wireless InSite REM parsing is the possible offset between the ray-tracer coordinate system and the one in which UE walk paths were defined. The newly introduced *XposRemOffset, YposRemOffset, ZposRemOffset* attributes for the *ns3::ThreeGppSpectrumPropagationLossModel* allow configuring offsets applied to the location of the parsed REM entry. In this thesis it was necessary to shift the parsed REM because of the misalignment of walk paths due to the usage of different coordinate systems.

Finally, aggregated REM data is written to a new inventory file *Inventory_WiIS.txt* in the *WriteRemToFile* method. Thus, it is not necessary to parse the output data from the Wireless InSite in each simulation run. The user may make use of the inventory file produced by the *WriteRemToFile* method.

3.1.3.2 REM Storage in the LTE Coordinator

With the ability to parse Wireless InSite output files and convert them into a structure that stores complete channel data for each location, the complete REM is received. The resulting file can be considered a *central database* for the LTE coordinator. However, there are no direct interfaces that would allow the *LteEnbRrc* to access the *ThreeGppSpectrumPropagationLossModel::allLinkData* directly. Moreover, such a connection would violate the layering and separation of concerns principles. Thus, it was decided to duplicate the file loading routines in the *LteEnbRrc* class and store a second instance of the REM.

At this point a differentiation between two use-cases is necessary. As will be discussed in further sections, simulation using the *measurement REM* implies that channel measurements are reported for *wrong* or *moved* locations. During the loading of REM into the LTE coordinator, a normally distributed error with the mean set to 0 and variance set to 10 is applied for the x- and y- components of the coordinate, where the REM entry is supposed to be saved. As a result, the REM contains gaps in locations, where originally valid non-empty REM entries were stored. One way to implement that is to apply an error directly while loading the previously prepared inventory file. To support this case, the *LoadInventory* method was added to the *LteEnbRrc* class to read the data and apply a normally distributed

error with hard-coded values set for its mean and variance. The disadvantage of this method is that every simulation run will generate different error values applied to the location data, making the result non-deterministic and hard to compare against other simulation runs. Alternative solution is to run the simulation until the parsing routing finalizes and generates the *measurement REM* file, and then stop the simulation execution. In such way a file is produced, that can later be re-used for all subsequent simulations to make sure that the underlying *measurement REM* is exactly same in each simulation run. The *LoadMeasurementRemFromFile* attribute was provided in the *LteEnbRrc* class to implement such behavior. Simple plain loading without applying normally distributed errors to REM entry locations is made possible with the *LoadRemFromInventory* method.

3.1.4 UE Mobility Error Model

The commercial pedestrian walk simulator *Viswalk* was used to generate realistic walk paths within the simulation area in previous works [2, 50, 51]. In this thesis not only the mobility of UEs is investigated, but also the impact of localization errors on the performance of the LABM algorithm. For this purpose an error model that shifts the latitude and longitude components of the generated walk path was implemented.

The study in [31] has proven the importance of realistic location error models, as even small localization errors were shown to lead to severe performance degradation and outages in specific cases. The authors highlight that a correlated error is a more appropriate model for the real-world performance of GNSS receivers that do not have any kind of error correction features, that could compensate localization errors with help of external sources of information. The Ornstein-Uhlenbeck process, originally defined in [54], was used to model correlated GNSS errors by authors in [31]. Thus, the process was implemented as a ns-3 class in the mobility library. The new *OrnsteinUhlenbeckErrorModel* class implements the discretized Ornstein-Uhlenbeck process estimation through the Euler-Maruyama approximation [55] by the following formula:

$$X_{n+1} = X_n + \theta(\mu - X_n)\Delta t + \sigma \Delta W_n, \tag{3.1}$$

where θ describes the rate of mean reversion, μ represents the long-term average, σ characterizes the volatility, and $W_n \sim \mathcal{N}(0, t)$. The rate of mean reversion θ describes how fast the process tends to its long-term average, whereas the volatility parameter σ determines the magnitude of the random variation in the process. $\Delta W_n \sim \mathcal{N}(0, \Delta t)$ and Δt denotes the time increment. The underlying normal distribution of W_n is configured to have the mean at 0, and the variance set to 0.25, which corresponds to the period of UE location updates in the mobility model. The *m_deltaT* parameter of the *OrnsteinUhlenbeckErrorModel* that represents the time difference between each consecutive step is also hard-coded to 0.25. The *GetNextValue()* method returns the X_{n+1} value that is then used as an error value applied to the x- or y- component of the UE location. The *OrnsteinUhlenbeckErrorModel* also provides a trace source *InternalStateTrace* that delivers the *OrnsteinUhlenbeckErrorTraceParams* structure, containing values of all internal parameters for debugging purposes.

3.2 Location-aided Beam Management Algorithm

The core of this thesis's contribution is the algorithm that implements location-aided beam management. The algorithm is hosted on the RRC layer of the LTE coordinator node. It accepts UE location reports and the REM as inputs. The output is the BPL that should provide best signal quality for the reported location according to the available data in the REM. The BPL information is distributed to UEs over the direct LTE RRC connection and to gNBs over the X2 interface. The LABM also schedules handover events in the case when they are needed for proper serving of an UE with the best possible connection quality. The following core procedures are relevant for the algorithm:

- **UE location reporting and error modeling** - The LTE coordinator receives the real, unmodified location of the UE originated in its mobility model. The *LteEnbRrc* is then able to optionally apply the error model to the reported location to simulate the GNSS localization inaccuracy.
- **REM querying** - The REM is queried using the reported UE location. The possible results are:
  - **Query failure** - The REM does not contain an entry that is saved for the queried location.
  - **Query success** - The REM contains a valid non-empty entry for the queried location.
  - **Empty query result** - The REM entry exists, but does not contain any paths.
- **Commanding BPLs to UE and gNB** - The LTE coordinator sends messages to both entities to set the specific antenna configuration and target *NetDevice* for further communication between each other.
- **Handover to the target gNB** - The LABM algorithm may force the UE to connect to a gNB that it considers the best serving cell.
- **Recovery procedure** - When the REM query fails or returns an empty entry, the algorithm might optionally execute a recovery procedure by trying to find the closes non-empty REM entry and using it for further processing.

3.2.1 Algorithm Flow

Figure 3.1 shows the flow diagram for the LABM algorithm implemented in the *LteEnbRrc* class. Green boxes show steps that terminate the algorithm, red boxes mean that the algorithm execution was aborted due to a specific condition, and blue boxes present steps that do not affect the logic, but only perform operations related to the ns-3 tracing mechanism. The starting point is the reception of the UE location report by the *LteEnbRrc::ForwardUePositionReportToREM*. The next step is then defined by the new *m_useErroneousUePosition* variable controlled by the attribute *ApplyErrorModelToUePositions* of the *LteEnbRrc* class. Depending on the value, the algorithm applies the error to the x-, and y- component of the location vector. The error value is calculated from the Ornstein-Uhlenbeck process so that the correlated error is simulated for the UE's location. Due to the fact that the resolution of the REM used for simulation is $1m \times 1m$, the resulting

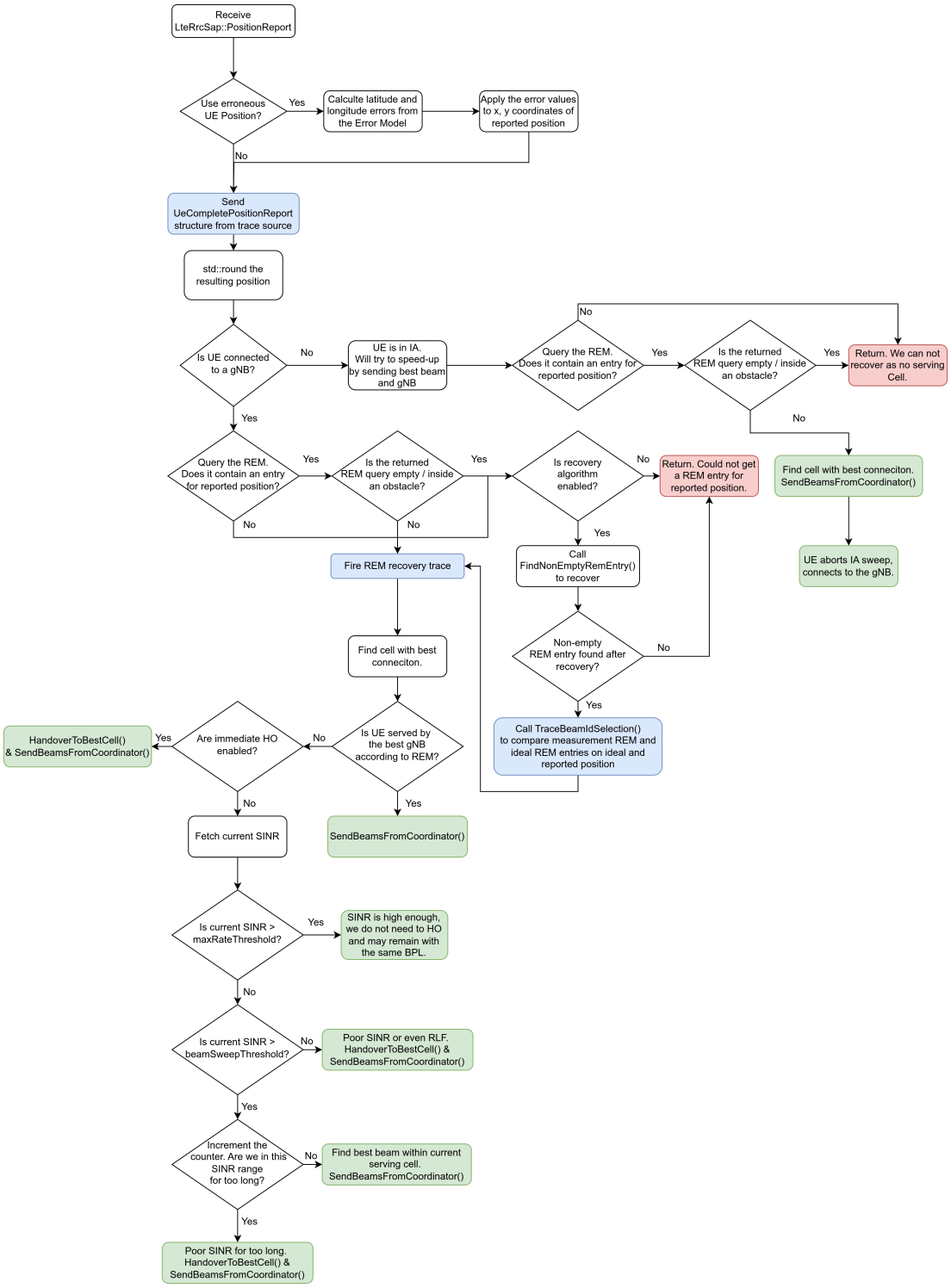

Figure 3.4: Location-aided beam management algorithm.

UE location has to be rounded to the closest integer value. This is done with the same method that is used in the *ThreeGppChannelModel*'s calculations - namely, *std::round()* function. The resulting value may now be used to query the REM.

The next step depends on the current state of the UE. The LABM algorithm exploits the fact that the LTE RRC connection is assumed to be established directly at the beginning of the simulation. This implies that the LTE coordinator is able to assist in the initial access process by notifying the UE which gNB and BPL are the most optimal to establish the connection. The *LteEnbRrc* class of the LTE coordinator is aware of the current state of the connection setup, as gNBs send a notification upon the successful attachment. The coordinator keeps track of gNB and associated IMSI's with help of the *m_lastMmWaveCell* map, where the IMSI is the key and gNB cell ID is the value. The *m_mmWaveCellSetupCompleted* is a similar structure with the difference that it provides the information whether the IMSI is already associated with a gNB in form of a boolean value. Thus, it is possible to use the *m_mmWaveCellSetupCompleted* to check whether the specific UE is still in the IA process.

3.2.1.1 UE Reports Location during Initial Access

If the UE is in IA, the algorithm queries the REM on the reported location. At this point there are three possible outcomes. Firstly, the query might either fail because the REM does not contain an entry for such location. This may happen if the queried location happens to be outside of the geographical area covered by REM, or if the error applied to the *measurement REM* moved the data to another grid point, leaving a gap in the original grid point. Secondly, the query might fail because the REM entry for the location exists, but is empty, meaning that *ns3::LinkData::m_paths* is 0. Such outcome is possible when the location happens to be inside an obstacle or building. Lastly, the query returns a non-empty entry. In this case, the *ns3::LinkData::m_pathloss* vector of the returned entry can be traversed and the index of the smallest path loss value can be identified with help of the *FindLowestPlIndex()* method. The calculated index, IMSI and the REM entry in form of *LinkData* are then passed to the *SendBeamsFromCoordinator()*. This method is responsible for the transmission of BPLs to gNB and UE. Transmission towards gNB happens over the X2 interface. The new structure *EpcX2Sap::LinkDataToGnb* contains the REM entry, target Cell ID and IMSI, for which the adjustment of beamforming vectors on thegNB side should be made. The *SendREMLinkDataToGnb* method of the *m_x2sapProvider* takes care of transmitting the complete message to the *EpcX2* class, where it is sent to the receiving X2 socket of the target gNB.

For the transmission of BPL to UE, the *LteRrcSap::LinkData* structure is used. It contains the target IMSI as well as relevant fields of the *ns3::LinkData* structure. The populated *LteRrcSap::LinkData* is then transferred as an RRC message via the new *SendRemBeamFromLTECoordinator* method of the *LteEnbRrcSapUser*, which represents the interface to send messages to UE over the RRC protocol. In order to derive the correct target RNTI, the *m_lteRnti* map is queried for the IMSI of interest. As a result, the *LteRrcSap::LinkData* structure is directly scheduled for reception on the UE RRC by the *LteEnbRrcProtocolReal* with a delay value of *RRC_REAL_MSG_DELAY*. It is left at 0 milliseconds, implying a direct latency-free scheduling of the message.

3.2.1.2 UE Reports Location in the Connected State

The LTE coordinator is informed about UE's location with help of the newly implemented *LteRrcSap::PositionReport* structure. This structure represents the actual error-free location of the UE and is referred to as reported error-free location. Depending on the simulation configuration, the LTE coordinator may apply a location error to the *LteRrcSap::PositionReport* structure, simulating the localization error for the UE. The data about the UE location affected by the error is referred to as reported erroneous location. The final knowledge of the LTE coordinator about the UE's location is referred to as reported location, meaning either error-free or erroneous location report. The actual location of the UE according to its mobility model is referred to as real location.

There are three main branches that are followed for the case when UE reports its location while being connected to a gNB. The exact branch depends on the success of the REM query and on whether the recovery procedure is enabled. Due to localization errors and stored entries of the *measurement REM*, the query on the reported erroneous location might fail in exactly same manner as described in the beginning of section 3.2.

When the REM query is successful and the returned entry contains valid data, the algorithm checks whether the current serving cell for this particular IMSI is the same as the cell ID of the gNB that has the lowest path loss value for the queried location. This check is enabled by the *m_lastMmWaveCell* variable of the *LteEnbRrc* that stores the *std::map* with IMSI as key and currently serving gNB as value. If the UE is already served by the best gNB, the algorithm simply commands the best BPL to gNB and UE with help of the *SendBeamsFromCoordinator()* method.

If the UE is not served by the best gNB, further actions depend on the configured handover behavior. The attribute *UseLabfImmediateHandovers* is a boolean value that defines whether the algorithm should immediatelly tell the UE to handover to the best serving gNB if the REM query detects that its current serving cell is not the most optimal one. Thus, if *m_immediateLabmHandovers* is set to *true*, the coordinator executes *HandoverToBestCell()* followed by the *SendBeamsFromCoordinator()* to make sure thatUE is connected to the bestgNB. In the opposite case, the algorithm follows a threshold-based decision on whether to execute the handover. If the current SINR level surpasses the maximum rate threshold *m_maxRateThreshold* of 22.7 dB, coordinator considers the link to be sufficiently good and stops the algorithm execution. If the signal quality is below the maximum rate threshold but is still higher that what is considered the *beam sweep threshold* of 10 dB [51], the algorithm transitions to the following threshold-based step. The *m_handoverHysterisisMaxCounter* controlled by the *LabmHandoverThreshold* attribute defines the maximum amount of algorithm iterations or received location reports from this particular UE that the UE may remain served by the sub-optimal gNB. If this number is exceeded, the algorithm forces the handover. The current amount of iterations spent at the sub-optimal gNB is tracked for each IMSI with help of the *m_imsiHandoverHysterisisCounter* variable. Until the *m_handoverHysterisisMaxCounter* is surpassed, the coordinator will still try to find the best possible BPL for the current serving gNB. *FindIndexForCurrentServingCell()* method extracts the best BPL for the current serving gNB of the IMSI. Coordinator then executes *SendBeamsFromCoordinator()* with the resulting data. However, if the signal quality was detected to be below $10\ dB$, the algorithm considers the SINR level to be too low and forces the handover to the best cell by calling *HandoverToBestCell()* and *SendBeamsFromCoordinator()*.

In the case when the UE query failed or returned an empty entry, the LABM will abort further processing in its default configuration. However, there is an option to try to recover from such situations, which can be enabled by setting the *EnableRemRecoveryAlgorithm* attribute to *true*. In this case, the initially failed query or the empty query for a reported UE location will lead to a call to the *FindNonEmptyRemEntry()* method. The *FindNonEmptyRemEntry()* method does not guarantee a successful recovery procedure. Thus, if the method returned a *nullptr* instead of the valid value for *ns3::Ptr<LinkData>*, the LABM algorithm is forced to abort its execution. In the contrary case, it continues with the *LinkData* entry that was found to be in proximity of queried location.

3.2.2 Recovery Algorithm

The *FindNonEmptyRemEntry()* method is the entry point for the recovery algorithm that tries to find a geographically close location that contains a valid non-empty REM entry if the REM query for reported UE location was not successful. As mentioned previously, such situations occur when the UE location error moves the query point inside an obstacle or when measurement errors during REM creation leave a *gap* for the queried location.

A simple approach for recovery from such a situation could be to iterate over neighboring locations, increasing the radius until the first matching entry is found. However, such an approach would require a significant amount of iterations when the REM query ends up in a large obstacle, as the amount of points to be checked will increase following a quadratic progression as the radius increases. Moreover, it is not guaranteed that the recovered point will not end up on the wrong side of an obstacle where no LOS connection can be established or the propagation paths are completely blocked. To overcome the inefficiency of such iterative algorithm, it was decided to leverage the knowledge about the current serving cell of the UE and its location. Due to the fact that locations of gNBs are static, it is acceptable to assume that their exact coordinates are known to the network infrastructure components. Thus, it can be assumed that the LTE coordinator is aware of gNB locations. Furthermore, the *m_lastMmWaveCell* variable allows to fetch the serving gNB for the IMSI of interest. Given the reported location of the UE, its serving gNB ID and gNB's location, it becomes possible to draw a virtual line between these two points that would ideally represent the LOS path. For the suggested implementation, it is assumed that no obstacles should be on such a virtual path between the gNB and the UE, as in an alternative case the cell would have probably not been chosen by the LABM algorithm.

The core of the recovery algorithm is the iterative testing of REM entries that lie on the virtual line that connects the UE's and gNB's locations. Bresenham's Line Algorithm [56] was selected as the implementation due to the similarity of the problem that it solves to the REM query recovery use-case. Bresenham's Line Algorithm is widely used in computer graphics to draw a straight line between two points in a raster display. It also finds application in robotics for navigation in discrete grid-based environments. The key idea of the algorithm is to determine which pixel should be plotted at each step to approximate a straight line in a best way. Instead of computing expensive multiplications or divisions, it uses incremental integer calculations based on decision variables.

The original application of Bresenham's Line Algorithm is meant for a grid-based system and the REM fits to such a description. However, instead of iterating from the starting UE grid point to the gNB grid point, the algorithm execution is aborted as soon as the underlying point contains a valid *LinkData* entry. The pseudo code for Bresenham's

Algorithm 1 Pseudo-code for the `FindNonEmptyRemEntry()` function.

```
1: procedure FindNonEmptyRemEntry(servingBS, UEPosX, UEPosY)
2:     bsPosX ← m_gNBpositions.at(servingBS).x
3:     bsPosY ← m_gNBpositions.at(servingBS).y
4:     Δx ← std :: abs(bsPosX − UEPosX)
5:     Δy ← std :: abs(bsPosY − UEPosY)
6:     stepX ← UEPosX < bsPosX ? 1 : −1
7:     stepY ← UEPosY < bsPosY ? 1 : −1
8:     D ← 2Δy − Δx
9:     D2 ← 0
10:    while true do
11:        if Reached position of the BS then
12:            Return nullptr; // Failed to find the entry
13:        end if
14:        D2 ← D ∗ 2
15:        if D2 >= Δy then
16:            D+ = Δy
17:            uePosX+ = stepX
18:        end if
19:        if D2 <= Δx then
20:            D+ = Δx
21:            uePosY+ = stepY
22:        end if
23:        Query REM atUEPosX,UEPosY
24:        if REM entry m_path != 0 then
25:            return REM entry
26:        end if
27:    end while
28: end procedure
```

algorithm integrated with REM querying checks is presented in Algorithm 1. In each iteration the algorithm checks whether the underlying REM entry contains at least 1 path. If this is the case, the algorithm stops and returns the found REM entry, that lies on the direct virtual line between the UE andgNB's location. If the algorithm reaches the end point represented by the gNB location, the recovery failed to find a suitable REM entry.

3.2.3 Mapping of AoA and AoD to BeamIDs

The REM stores AoA and AoD in the range of $[0, 360)$ degrees. For the mapping of AoA and AoD data to a specific combination of sector and elevation values, the information about the angular range of the underlying antenna model as well as its default orientation is needed.

The *NrPhy* class holds a reference to the *BeamManager*, which in turn holds a reference to the *ThreeGppAntennaArrayModel*, that represents the antenna array instance implemented according to the definition in [57]. *NrPhy* provides the *AntennaConfiguration* attribute that affects the number of horizontal and vertical antenna elements. Depending on

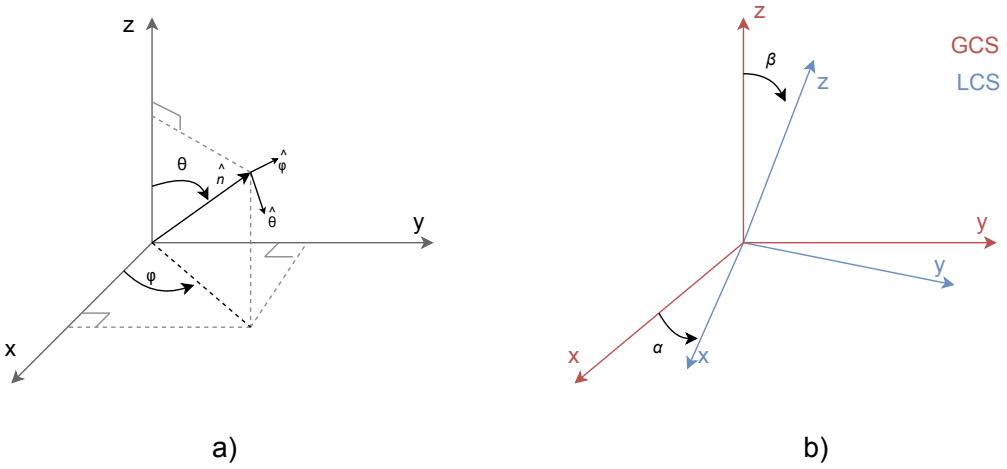

Figure 3.5: a) Definition of spherical angles and spherical unit vectors in a Cartesian coordinate system for the 3GPP antenna model. b) Relation between the antenna LCS and GCS. Adapted from [57].

that attribute, the *NrGnbPhy* and *NrUePhy* create appropriate beamforming vectors that will be used for controlling the antenna transmission and reception patterns. As can be seen in the Figure 3.5 a), in the Local Coordinate System (LCS) of the antenna, ϕ defines the angle in the X/Y plane as the rotation around positive Z axis starting from the positive X axis in the counter-clokwise direction towards the Y axis. The angle θ in LCS is the angle from the positive Z axis towards the X/Y plane in clockwise direction. According to [57], θ of 0 degrees point to zenith and θ of $+90$ degrees points to the horizon. The ϕ angle is measured starting from the X axis. For the GCS, the *ThreeGppAntennaArrayModel::m_alpha* controls the bearing angle in radians, which defines the α angle in the X/Y plane. As can be seen from the Figure 3.5 b), the α angle defines the rotation around positive Z axis starting from the positive X axis in the counter-clockwise direction towards the Y axis. The *ThreeGppAntennaArrayModel::m_beta* controls the downtilt angle in radians, defining the β angle from the positive Z axis towards the X/Y plane. α and β define the transformation from the antenna LCS to the GCS.

In the default state, the *m_alpha* and *m_beta* parameters of the *ThreeGppAntennaArrayModel* are set to 0. For validation purposes, a gNB was placed in an open area. A UE was placed at fixed coordinates south, east and north to the gNB. For each case, theUE did an exhaustive beam sweep and determine the appropriate beam IDs for the link establishment. Such experiments has shown that sector 0 corresponding to the gNB beamforming azimuth angle of -90° was chosen for the UE located south, sector 10 with gNB beamforming azimuth angle of 0° for the UE located east and sector 20 with gNB beamforming azimuth angle of $+90$° for UE located north. From this result, it can be concluded that the default orientation of the antenna has its normal vector pointing east. It is also known that the data generated by the Wireless InSite ray tracing software aligns

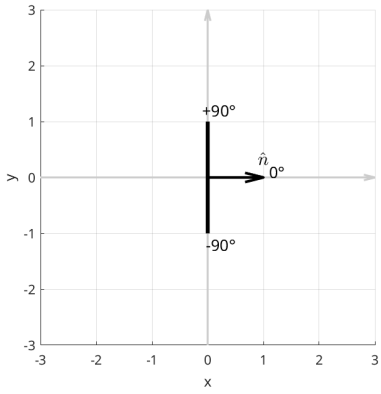

Figure 3.6: Default antenna orientation in the GCS.

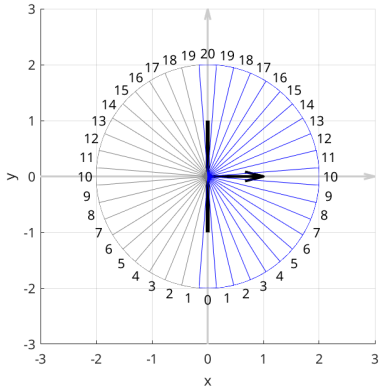

Figure 3.7: gNB antenna azimuth sectors.

with the normal vector of the antenna, having 0° at the X-axis. Figure 3.6 shows the default orientation of the antenna array from the top view with respect to the GCS.

A further aspect that had to be validated is how sectors are mapped for angles beyond 180° in the X/Y plane. According to [2], the gNB antenna has 8×8 elements with 21 sectors and 9° of angular resolution. Such model covers only 180 degrees of angular space, but the REM-based operation implies angular ranges of 360°. With the same approach of placing the UE in specific spots behind the antenna, it was possible to see that for an AoD of 211°, the gNB creates a beamforming vector at -27°, mapping to sector 7.

This allows to conclude that the beamforming vector angles and sectors wrap around in the second and third quadrants as if the antenna is virtually mirrored to serve the region that is behind it. With all of the information above, the mapping of the REM AoD/AoA to azimuth sectors of the antenna was derived and is shown in Figure 3.7 and 3.8. Figure 3.7 presents the layout of sectors on the gNB's antenna according to the configuration with 8×8 elements and angular resolution of 9°. Figure 3.8 shows the layout of sectors on the UE's antenna with 4×4 elements and an angular resolution of 18°. Blue sectors

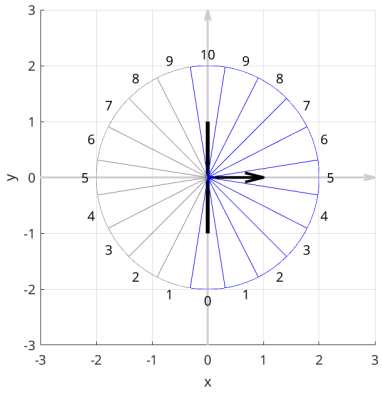

Figure 3.8: UE antenna azimuth sectors.

are the ones that are matching to the expected physical antenna layout, where the beams are pointing away from the virtual backplate. The antenna sectors depicted in grey were observed to be arranged in this configuration through empirical testing, utilizing adapted UE walk paths designed to compel the beam to orient behind the backplate of the antenna.

3.3 Tracing Modifications

The ns-3 tracing system enables users to collect and analyze simulation data efficiently. It provides an event-driven architecture that allows to monitor various network parameters, such as packet transmissions, receptions, and protocol interactions. The tracing system in ns-3 is built on two main components: trace sources and trace sinks. Trace sources are predefined hooks within the simulation modules that generate events when specific actions occur, while trace sinks are user-defined functions that capture and process these events. ns-3 supports both ASCII and Packet Capture (PCAP) tracing, making it a versatile tool for debugging and performance evaluation in network simulations.

As this thesis includes the work in [50, 51], it inherits extensions to the tracing system provided by modified *RxPacketTraceParams* and *BeamSweepTraceParams* structures. Both of them provide valuable insight into the PHY layer throughput and events related to beam management such as exhaustive sweep initiation, outcome and beam adjustments as a reaction to CSI-RS control signals. In addition to available tracing information, new sinks and sources were added to provide more insight about the effect of UE localization errors, failed REM queries, and recovery events.

3.3.1 UE Location Report Tracing

Tracing of the real and reported UE location allows plotting both walk paths to easily see the effect of the applied error model. The *UeCompletePositionReport* structure was added to keep IMSI-specific information about the real location derived from its mobility model, the error values applied to x- and y-coordinates, and the resulting location that the LTE coordinator uses to query the REM. The structure is filled and triggered via the *UePositionTrace* source upon reception of the UE location report in the *ForwardUe-*

PositionReportToREM() method. Due to the fact that the error model is applied by the coordinator, both real and erroneous locations are known at this point. This information allows investigating the resulting walk path and visually highlights potentially problematic cases where UE gets shifted into an obstacle for prolonged periods.

3.3.2 REM Query Tracing

The availability of both real and reported UE locations allows comparing the REM queries for both locations and identifying beam offsets caused by the UE location error and/or *measurement* REM errors. The logic for this process is implemented in the *TraceBeamIdSelection()* method, that accepts the *LteRrcSap::PositionReport* and the *ns3::LinkData* structure that was returned by the REM query. The main purpose of the *TraceBeamIdSelection()* method is to compare BPL that would have been reported for real UE location from the *ideal REM* to the BPL that will be returned by the LABM algorithm. Querying the *ideal REM* requires that it should be also stored at the coordinator in addition to the *measurement REM*. Thus, the *LteEnbRrc* class has received the *m_idealLinkData* member variable, that stores the *ideal REM* unaffected by measurement errors. This structure in only used for tracing purposes. Even though it poses additional overhead in terms of memory consumption, it helps to provide valuable insights about the algorithm. After the resulting *BeamId*s of the *ideal REM* query are available, the function continues with querying the *m_allLinkData* that is used for the LABM algorithm and represents the *measurement REM*. The outcome of this query are *BeamId*s for the reported location, which can then be subtracted from ideal results to derive beam offsets. Due to the fact that azimuth sectors wrap around and have duplicating IDs for different angles, the offset can not be simply derived from the subtraction operation. In order to uniquely identify each azimuth sector, the mapping between angle ranges and sectors was extended to contain a unique index for each azimuth sector. The *LteEnbRrc::SectorDegreeIndex* structure was introduced for this purpose and allows keeping the lower and upper bounds for angular data together with an index. This structure is then used as a *std::map* key and the azimuth sector number is stored as value. The offset is then calculated by taking the difference between indices of azimuth sectors and applying the normalization operation to derive the closest distance between ideal and actual azimuth sectors. Ideal and erroneous beams along with offsets are logged into a file with help of the *AsciiTraceHelper* for further post-processing with external software.

3.3.3 REM Measurement Error Tracing

If the *UseMeasurementREM* attribute of the *LteEnbRrc* class is set to *true*, a normally distributed error will be applied to the position, at which a REM entry gets inserted. This results in REM entries being shifted and gaps, where no data is present. The *RemQueryErrorTrace* source provides *std::map<Vector, std::pair<double, double»*, which represents grid entries where a non-empty REM entry was inserted, as well as the error value that was applied for its position. The trace source is sending the structure *m_remPositionErrors*, which is filled in the *LteEnbRrc::LoadInventory* method. The new *LogRemMeasurementError()* method writes the received data into a file for further post-processing. The *RemNonEmptyEntriesTrace* source provides the vector of REM entries that contain valid data. The tracing source *m_measRemNonEmptyEntries* sends the *m_remNonEmtpyEntries* variable that is also filled in the *LteEnbRrc::LoadInventory* method

if the amount of paths for currently parsed REM entry is not 0. The main simulation file contains a new trace sink *LogRemNonEmptyEntries()* that writes positions into a file, allowing to plot the resulting *measurement REM*.

3.3.4 Recovery Algorithm Tracing

The recovery algorithm tries to find the non-empty REM entry on the path towards the serving gNB. As a result, the reported UE location gets shifted. A new structure *RemQueryRecoveryAlgorithmTraceParams* was introduced to keep track of the recovery events. It keeps track whether the original query of the REM was successful and records the reported UE location. If the UE had to be recovered, this is indicated by setting the *remPointRecovered* to *true* and the coordinates of the new location are saved into the *recoveredCoords*. Such events may correlate with sudden SINR changes and provide additional context when analyzing the output data. The *LogRemQueryRecovery()* method in the main simulation file logs all fields from the *RemQueryRecoveryAlgorithmTraceParams* structure and additionally calculates the euclidian distance between the reported and recovered location. In post-processing, this data allows visualizing the effect of the recovery algorithm and matching its events to SINR or beam offset.

4

System Model and Simulation Scenarios

In this Chapter the details of the system model and simulation setup are presented. Section 4.1 describes the system model, including antenna parameters and network models with its core simulation parameters. Additionally, the UE mobility pattern and details about the configured error models are presented. The overview of simulated scenarios is presented in Section 4.2. The key performance metrics that will be used for the evaluation of simulation results are described in Section 4.3.

4.1 System Model

4.1.1 Antenna Model

Antennas on the UEs and gNBs are using analog beamforming with a planar antenna array based on the 3GPP antenna array model [57]. The individual antenna elements are arranged in both horizontal and vertical dimensions with a spacing of half the wavelength of the carrier frequency. Beam alignment in any direction is achieved by applying complex phase shifts to the analog signals, allowing the antenna array to steer the beam in the desired direction. In this work, beam steering and scanning are implemented by selecting specific beamforming vectors from a predefined codebook [58]. Each vector in the codebook corresponds to a beam that covers a specific angular region around the antenna.

The *ThreeGppAntennaArrayModel* class of the ns-3 *antenna* module is used to represent the antenna in both *NrUePhy* and *NrGnbPhy* classes. In this thesis, the antenna arrays of size 8×8 at gNB and 4×4 at UE are used. The granularity of the UE and gNB antennas in the azimuth plane is set to 18° and 9°, resulting in 21 and 11 sectors in the azimuth range, respectively. gNB and UE sectors in the azimuth range were visualized in Figure 3.7 and Figure 3.8. The vertical plane granularity is set to 30° for both gNB and UE antennas. The angles in the vertical plane for the gNB are 90° for pointing the beam in horizontal direction, 150° for pointing the beam downwards toward the ground, and 120° for an intermediate range. The angles in the vertical plane for the UE are 90° for pointing the beam in horizontal direction, 30° for pointing the beam upwards toward the sky, and 60° for an intermediate range. The Figure 4.1 depicts the elevation sectors of the UE and gNB antennas. Such configuration results in codebooks consisting of $N_{\text{gNB}} = 63$ and $N_{\text{UE}} = 33$ individual beams at the gNB and UE, respectively. Given the 5G-NR numerology $\mu = 3$, the maximum number of SSBs in a single SS burst is 64 [22]. Due to the total amount of gNB sectors N_{gNB} being 63, it is possible to sweep across all sectors of the gNB within a single SS burst duration T_{ss} of $20\ ms$. As a result, the exhaustive beam search procedure has a duration of $T_{\text{ss}} \times N_{\text{UE}} = 660\ ms$.

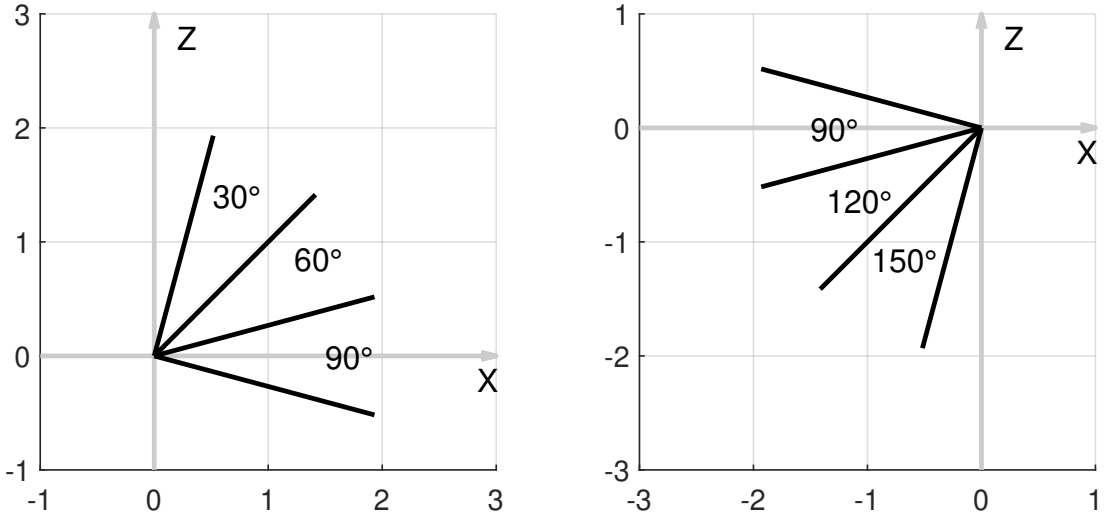

Figure 4.1: Elevation sectors of UE antenna on the left and elevation sectors of gNB antenna on the right.

4.1.2 Channel Model

In this thesis, ray-tracing data for the site-specific mmWave channel model was obtained using the Wireless InSite software. The ray-launching granularity is set to 0.1°. The maximum number of reflections is set to 4 with no scattering and diffraction due to carrier frequency being 28 GHz. The material of buildings present in the simulation area is set to be glass. As the result, for each gNB the Wireless InSite ray-tracer outputs all propagation paths from the gNB to every potential UE location. For each provided path *k*, the following data is generated:

- Type of path - LOS or NLOS.
- Path loss
- AoA $\{\phi_k^{\text{UE}}, \theta_k^{\text{UE}}\}$ in azimuth and elevation
- AoD $\{\phi_k^{\text{gNB}}, \theta_k^{\text{gNB}}\}$ in azimuth and elevation
- Received power level
- Delay spread

The ray-tracing data is imported into the simulation by the *NrHelper* class, allowing the *ThreeGppChannelModel* and *ThreeGppSpectrumPropagationLossModel* classes to retrieve required information for the current UE location.

4.1.3 Network Model

The area east of the main train station of the city of Frankfurt am Main, Germany is used for the simulation setup and presented in Figure 4.2. It presents the region with medium

	Parameter	Value
PHY and Link Layer	TX power	20 dBm
	Center frequency	28 GHz
	Bandwidth	400 MHz
	Numerology	3
	SCS	120 kHz
	Number of RBGs	264
	Number of SSBs per SS burst	64
	SS burst period	20 ms
	gNB antenna size	8 x 8
	UE antenna size	4 x 4
	gNB horizontal granularity	9°
	UE horizontal granularity	18°
	gNB vertical granularity	30°
	UE vertical granularity	30°
	gNB sectors	63
	UE sectors	33
	Beam search duration	660 ms
MAC & Upper Layers	RLC mode	UM, HARQ: enabled
	Transport layer protocol	UDP
	P2P link delay	5 ms
	Scheduler policy	TDMA: RR

Table 4.1: Fundamental simulation parameters.

urbanization level, where all buildings have a height of $10\ m$. The network is composed of 15 mmWave gNBs placed at $10\ m$ height within a $500m \times 500m$ area. The black square outlines the simulation area. Yellow dots represent the locations of mmWave gNBs. The NSA 5G-NR network architecture is used and the LTE coordinator is co-located with gNB 7. Every potential RX location represents a $1\ m^2$ grid point of the simulation area. gNBs transmit at the central frequency of $f_c = 28$ GHz with power of $20\ dBm$. The total bandwidth of the system is set to 400 MHz. The 5G-NR numerology is set to be $\mu = 3$, resulting in the Subcarrier Spacing (SCS) of 120 KHz. The number of RBGs in the frequency domain equals to 264 and the SS burst is set to contain 64 SSBs. The summary of all fundamental simulation parameters is provided in Table 4.1.

The location is fetched from the provided walk path information as detailed in Section 4.1.4. The RLC layers are set to operate in the Unacknowledged Mode (UM) with HARQ enabled. The MAC scheduler is set to operate with in TDMA with the RR policy. The simulation time was set to 240 s for all simulation scenarios.

The UE traffic model is the Constant Bit Rate (CBR) of 400 Mbit/s sent over UDP with packet size of 1400 bytes. The UDP source is located at the remote host and connected to the EPC with a latency of $5\ ms$ to model routing and computation delays.

4.1.4 UE Mobility Model

The UE walk paths are inherited from the work in [2,50,51], where they were generated with the help of the commercial pedestrian path simulator *Viswalk* [59]. The motion information

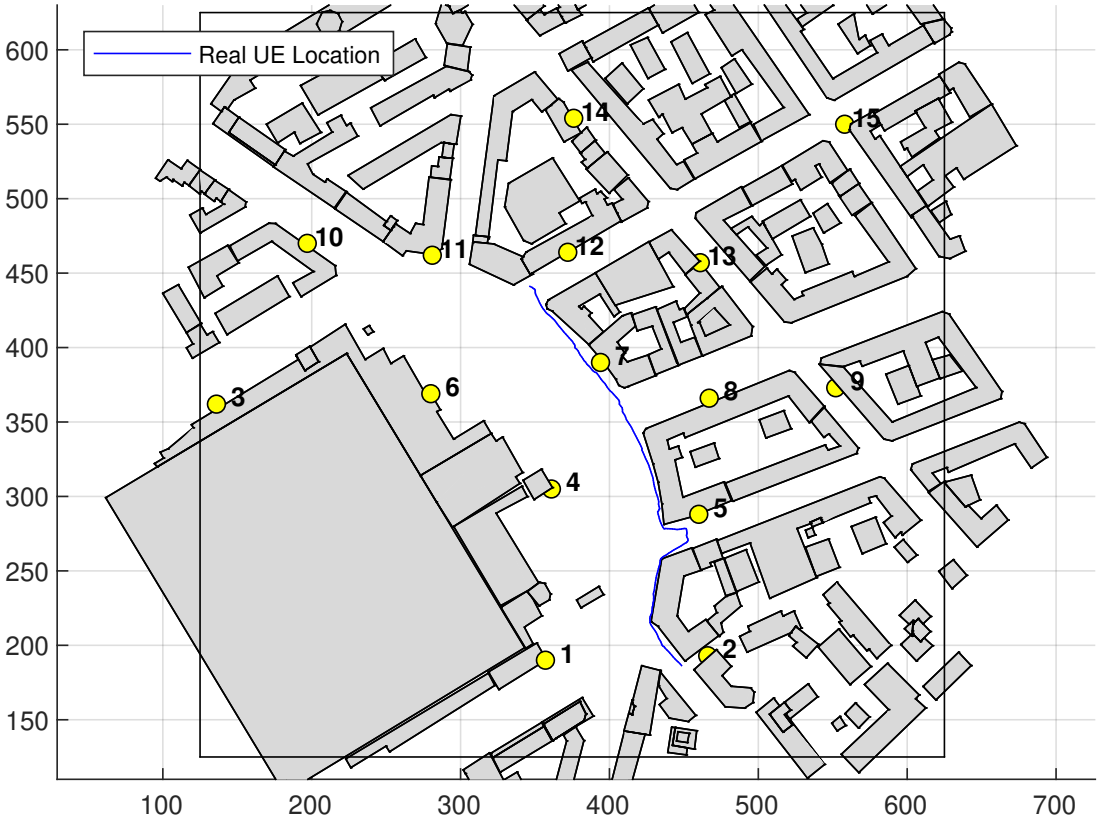

Figure 4.2: The building layout (grey), the real UE walk (blue), and deployed mmWave gNBs (yellow) in the urban area in Frankfurt. The simulation area is bounded by the black square.

	Medium Urbanization			High Urbanization		
Error Component	Θ	μ	σ	Θ	μ	σ
Latitude	6.2	1.5	3.8	6	8.1	8.6
Longitude	3.9	2.4	4.2	4	-1.7	4

Table 4.2: Ornstein-Uhlenbeck model parameters for latitude and longitude error in the medium and high urbanization scenarios.

was generated with a resolution of 4 samples per second with an average movement speed of $1\ m/s$. In this thesis a single walk path is used for all simulation scenarios and it can be seen as a blue line in the Figure 4.2. The selected walk path can be considered challenging in terms of the propagation environment and LOS, NLOS conditions.

The Orsntein-Uhlenbeck process is used to model the correlated error for the UE location information. Parameters that are used to model the longitude and latitude errors were fitted from the measurement dataset by the authors in [60]. Given the type of the simulation area, parameters for a correlated error in medium urbanization were selected for most of performed tests. The relevant parameters applied to the error model implemented

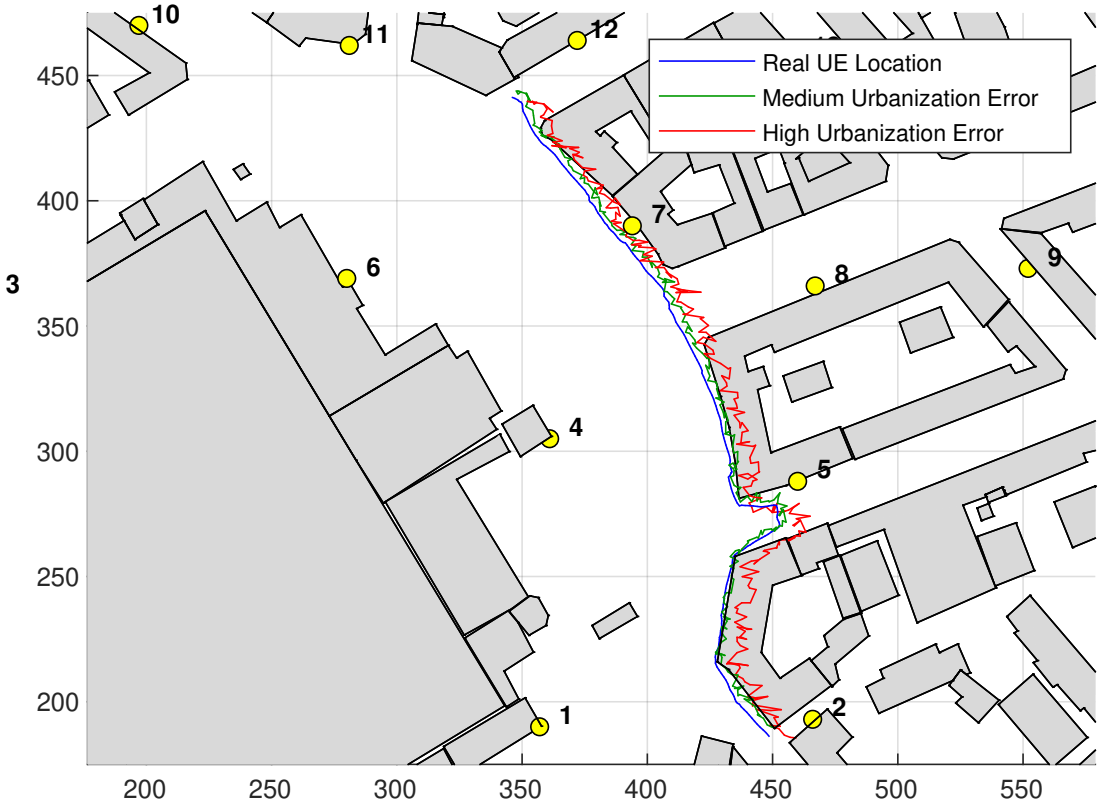

Figure 4.3: Real UE location (blue), location affected by medium urbanization error (green) and location affected by high urbanization error (red). The error model parameters are set according to the Table 4.2. gNB locations represented as yellow dots.

according to Equation (3.1) are listed in Table 4.2. Additionally, one set of testing scenarios investigates the effect of high urbanization on the LABM algorithm and the parameters are selected according to the relevant entries of the Table 4.2. Those parameters were derived by authors in [60] from the measurement data from Frankfurt city blocks with skyscrapers that significantly obstruct the LOS between a GNSS receiver and satellites, leading ot severe multipath and consequent increased inaccuracy in the location estimation. The real UE walk and erroneous realization of the medium and high urbanization are presented in the Figure 4.3 with blue, green and red lines, respectively.

4.2 Simulation Scenarios

The main points that are investigated in this thesis are the individual and combined contributions of REM query errors due to inaccurate UE locations being reported to the LTE coordinator and the effect of using the *measurement REM* in an end-to-end 5G-NR network simulation. In addition to that, the variation of available parameters of the implemented LABM algorithm are applied. Seven main configurable parameters can be identified that

affect the network behavior and performance. Considering the expected effect of each of available parameters, scenarios defined in Table 4.3 were selected for simulation.

- **Activation of LABM algorithm**: When LABM algorithm is enabled, the beam management is exclusively controlled by the LTE coordinator with the help of REM. The only exception is the IA procedure if the REM query fails for the reported location while the UE is not yet connected to a gNB.
- **UE location report frequency**: If set to a lower value than the actual location updates, the coordinator has a coarser knowledge about UE location, increasing the risk of selection of an outdated BPL.
- **Error model for UE location reports**: A correlated error may be applied for the UE location, causing the coordinator to query the REM for the wrong location. Depending on the situation, this might lead to severe beam misalignment.
- **Measurement error in REM**: This parameters aims to simulate the case, when BPL measurement reports tagged with an UE location are used to populate the REM. If the UE location estimate is not accurate due to GNSS errors, the REM likely stores the reported BPL measurement for an incorrect location during the REM construction. This is modeled by introducing this parameter, that affects the loading of REM into the coordinator. If the parameter is enabled, a normally distributed error will be applied on top of the location, for which the REM entry should have been saved, causing it to be moved into a random direction. As a result, the coordinator either selects a wrong REM entry, or can not query at all, as the data is missing completely. If the parameter is disabled, the coordinator uses *ideal REM*, which stores REM entries for actual locations unaffected by errors during the construction of the REM.
- **Immediate handover to the best gNB**: If UE is not served by the best gNB according to the information in REM, the UE might be scheduled for a handover in the same iteration where the query is performed. This might lead to an increased amount of handover events and ping-pong handovers, where the UE unnecessarily jumps between gNBs. However, in ideal case this should always lead to the best possible signal quality.
- **Handover hysterisis threshold**: If immediate handovers in the LABM algorithm are disabled, the UE may remain connected to the gNB that REM considers sub-optimal based on provided SINR level. The handover hysterisis threshold sets the amount of reported UE locations, defining the amount of algorithm iterations during which the UE may remain served by the sub-optimal gNB. Such threshold may help to reduce the amount of handover events and eliminate ping-pong handovers, but may also lead to significantly degraded SINR level if the environment changes drastically since the last BPL update.
- **LTE RRC delay**: This parameter allows simulating the communication delay that affects UE locaiton reports and BPL commands from the coordinator. If this parameter is activated and a large-enough value is set, the coordinator will receive outdated location information.

- **Recovery Algorithm**: This parameter enables the usage of the implemented recovery algorithm that tries to find an alternative REM entry if the REM query on the reported location has either failed or delivered an empty REM entry.

	Enable LABM	UE Location Report Frequency	Error Model for UE Location Reports	Use Measurement REM	Use Recovery Algorithm	Immediate Handover to the Best Cell	Hadnover Hysteresis Threshold	Additional parameters
0.a	No	-	-	-	-	-	-	Realistic IA.
0.b	No	-	-	-	-	-	-	Realistic IA. SSB RLM.
1	Yes	4	-	-	-	+	-	-
2	Yes	1	-	-	-	+	-	-
3.a	Yes	1	+	-	-	+	-	-
3.b	Yes	1	+	-	-	-	1	-
3.c	Yes	1	+	-	-	-	2	-
4.a	Yes	1	-	+	-	+	-	-
4.b	Yes	1	-	+	-	-	1	-
4.c	Yes	1	-	+	-	-	2	-
5.a	Yes	1	+	+	-	+	-	-
5.b	Yes	1	+	+	-	-	1	-
5.c	Yes	1	+	+	-	-	2	-
6.a	Yes	1	+	-	+	+	-	-
6.b	Yes	1	-	+	+	+	-	-
6.c	Yes	1	+	+	+	+	-	-
7.a	Yes	1	+	+	+	-	1	-
7.b	Yes	1	+	+	+	-	2	-
7.c	Yes	1	+	+	+	-	3	-
8.a	Yes	1	+	+	+	+	-	high urbanization error
8.b	Yes	1	+	+	+	-	1	high urbanization error
8.c	Yes	1	+	+	+	-	2	high urbanization error
8.d	Yes	1	+	+	-	+	-	high urbanization error
9.a	Yes	1	+	-	-	+	-	LTE RRC Delay: $\mu = 250, \sigma = 300$
9.b	Yes	1	-	+	-	+	-	LTE RRC Delay: $\mu = 250, \sigma = 300$
9.c	Yes	1	+	+	-	+	-	LTE RRC Delay: $\mu = 250, \sigma = 300$
9.d	Yes	1	+	+	+	+	-	LTE RRC Delay: $\mu = 250, \sigma = 300$

Table 4.3: Overview of the performed simulation scenarios with applied parameters.

Scenario 0.a and 0.b represent the default 5G-NR configurations of the NSA architecture and are meant to provide baselines that can be compared to any configuration of the LABM algorithm. In a default 5G-NR network deployment according to the standard, the network does not have the location-aided BPL selection. *Scenario 0.a* is configured to use the realistic IA, forcing the simulation to perform realistic beam sweeps with associated delays and affecting the experienced application-level IP throughput and latency. The radio link monitoring is enabled with the *rlmOn* parameter in the *main.cpp* file, enabling queueing of CSI-RS messages and performing the RLM procedures [61]. CSI-RS signals monitor alternative beams from the serving gNB. The set of these beams is determined based only on the information from the exhaustive beam sweep. That means that over time, the information gets stale. Such configuration would represent the basic configuration of the 5G-NR NSA network. Each time the UE performs an exhaustive beam sweep, the most optimal BPL is determined and used until the signal degrades below the RLF threshold of $-5\ dB$, or the LTE coordinator detects the signal level to be below the beam sweep threshold of $10\ dB$ and commands a switch to another beam, if a better beam of serving gNB is detected by measurements based on CSI-RS signals. If no alternative beam is known from CSI-RS signals, the UE has to perform an exhaustive beam sweep.

Scenario 0.b additionally makes use the SSB-based RLM, which helps to continuously update the beams that are monitored with help of CSI-RS signals. The periodic reception of SSBs from the serving gNB helps to update the information about beams that need to be monitored by CSI-RS signals, leading to the tracking based on much more fresh knowledge of short-term channel dynamics. Due to the fact that the SSB-based RLM is a standardized procedure that may be implemented and used in a real 5G-NR network deployment, the baseline *scenario 0.b* assumes the SSB-based RLM to be enabled. As a result, UEs are sending measurement reports based on periodic SSB sweeps to the serving gNB, which then forwards them to the LTE coordinator. This information can then be used by the LTE coordinator to update the monitored beams by the CSI-RS signals, resulting in a significantly more up-to-date knowledge of alternative BPLs and is able to react faster to the degradation of signal quality at the expense of the significantly increased overhead due to frequent measurement reporting.

Scenario 1 and 2 represent the ideal case for the LABM algorithm. *Scenario 1* represents the ideal case for the LABM algorithm, where UE location reporting frequency is identical to the frequency of actual location changes, which happen 4 times per seconds. In this configuration the coordinator does not apply an error on top of reported UE locations and uses the *ideal* error-free *REM*. In addition to that, immediate LABM handovers are enabled, making sure that the UE is always served by the best gNB. Such configuration should result in the best possible beam alignment. *Scenario 2* introduces subsampling to location reporting process. The UE is now able to send reports only once a second, which better reflects the real world capabilities of consumer-grade GNSS receivers in modern smartphones. With such configuration the coordinator is not able to follow the complete path of the UE. However, given the relatively slow average UE moving speed of $1\ m/s$ and the REM granularity of $1\ m^2$, the effect of this downsampling is expected to be insignificant. The 1 Hz location reporting frequency will be used for **all** following scenarios in order to provide a more realistic simulation.

Scenario 3 investigates the isolated effect of the REM query errors due to inaccurate UE locations being reported to the LTE coordinator. *Scenario 3.a* investigates the isolated effect of UE localization error on the performance of the LABM algorithm with enabled immediate handovers in the LABM algorithm. The error model implemented with help of the Ornstein-Uhlenbeck process with parameter set according to Table 4.2 is applied on top of real UE location. The resulting walk path is demonstrated as the green line in the Figure 4.3. It can be noticed that the starting point near the gNB 2 happens to be shifted into the building, meaning that there will be no corresponding non-empty REM entry for this location. In the first portion of the walk path, such events happen frequently and are expected to cause failures of the LABM algorithm and consequent RLF, as the recovery algorithm is not enabled for this scenario. Prolonged lateral movements inside obstacles are expected to have the strong impact on performance. *Scenario 3.b* and *3.c* investigate the impact of disabled immediate handovers and set the hysterisis threshold to 1 and 2, respectively. Intuitively, it is expected that larger threshold will cause more severe performance degradation due to the fact that the LTE coordinator may not perform a handover to the best gNB fast enough before a further signal degradation occurs. For the case when the threshold is set to 2, and given the frequency of location updates in the UE mobility model of 4 Hz, the UE manages to switch up to 8 locations according to its mobility model. Depending on the exact location, this may lead to situation where UE loses the LOS to its serving gNB earlier than the next BPL command arrives.

Scenario 4 investigates the effect of querying the *measurement* REM without UE location error in REM querying, and without the recovery algorithm. In contrast to the *ideal* error-free REM, the *measurement REM* does not provide a valid non-empty REM entry for each location that is not located within an obstacle. The resulting empty-entries are visualized as white dots in the Figure 4.4, whereas blue dots represent non-empty REM entries affected by the location error during the REM construction. With the *measurement REM*, it is expected that the LABM algorithm might fail to provide any BPL for relatively long periods of time, letting the UE to fall below the RLF threshold. Additionally, the algorithm might frequently choose the wrong BPL, resulting in lower SINR levels at the RX or even brief connections to NLOS gNBs. *Scenario 4.a* executes immediate handovers. Due to inaccurate REM entries, it is expected that the UE might experience increased amount of handover events, especially around regions with building corners. *Scenario 4.b* and *4.c* use hysterisis thresholds of 1 and 2 instead of immediate handovers, respectively. In this configuration, the delayed decision to switch to a different cell might be beneficial, as it may prevent ping-pong handovers, especially in areas where UE walks around building corners.

Scenario 5 investigates the combined effect or UE location error in REM querying and *measurement REM*. Intuitively, a significant decrease of signal quality is expected in this configuration due to the inaccurate location information both in REM querying and in REM construction. However, due to the fact that REM entries may be moved into buildings, the previously unsuccessful query on reported erroneous UE location might now deliver a non-empty REM entry. Thus, technically, the LABM algorithm may deliver a BPL in the cases where it would have failed in previous scenarios. However, it is still not guaranteed that the returned REM entry represents a data point that is close enough to the real UE location, but the effect of the error at those two stages might be compensated. *Scenario 5.a*

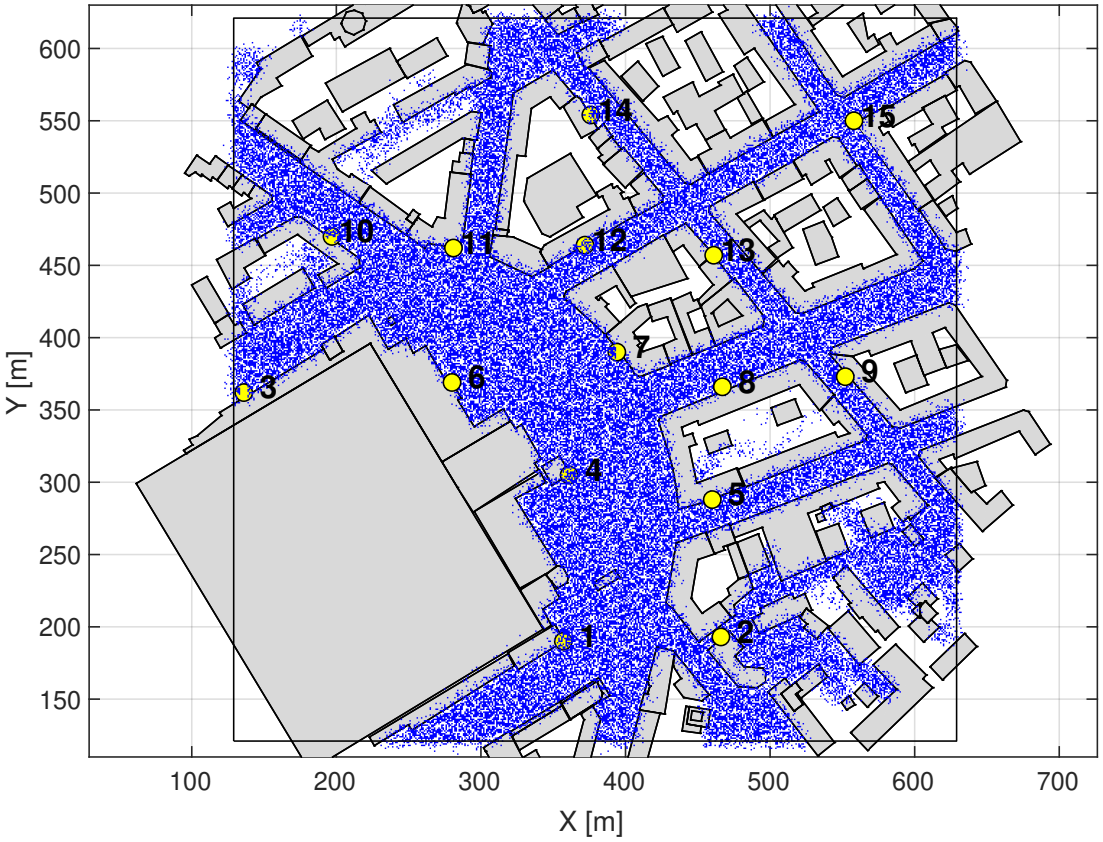

Figure 4.4: Locations of the non-empty entries of the measurement REM (blue). gNB locations represented as yellow dots.

uses immediate handovers and as in previous configurations, frequent connections to sub-optimal mmWave gNBs may be expected. Scenario *5.b* and *5.c* use hysterisis thresholds of 1 and 2 instead of immediate handovers, respectively. For these two cases it can not be confidently claimed that the delay in decision to handover may be beneficial. Normally, if the combined contribution of reported erroneous UE location and the *measurement REM* entry leads to the choice of a REM entry for a location that is far away from the real UE location, or on the wrong side of the building, resulting in a largely sub-optimal BPL choice. Thus, the signal quality might be degraded more significantly if the decision to execute handover to another cell is delayed.

Scenario 6 investigates the effect of the recovery algorithm with immediate handovers in case of individual and combined error of UE location errors in REM querying and of the *measurement REM*. The immediate handovers are enabled for all variations of the *scenario 6*. The scenario *6.a* can be compared to *3.a*, as it introduces the recovery for the case when only UE location error in REM querying is applied. Due to the fact that *ideal REM* is used, it is expected that the recovery algorithm corrects the UE's erroneous locations to locations, showing similar channel properties to the real UE location, thus returning a good

enough or even an optimal BPL. As a result, the BPL updates from the LABM algorithm are expected to always succeed after the first IA. Scenario *6.b* introduces recovery in cases where only errors due to the usage of *measurement REM* exist, and can be compared to the scenario *4.a*. In this case, the recovery will be triggered also in the cases when query fails due to empty entries in the *measurement REM*. However, the resulting data point will not necessarily improve the signal quality, as the data in the recovered location might cause a stronger beam offset or initiate the connection to NLOS gNBs. Scenario *6.c* investigates the effect of recovery algorithm on the combined contribution of UE location errors in REM querying and *measurement REM*. This configuration may so far be considered the closest to a possible real world deployment of the LABM algorithm. The motivation is that both error contributions will exist in the real world and the recovery algorithm is expected to improve the link quality in terms of SINR values on the RX side.

Scenario 7 investigates the effect of combined error contributions of the UE location errors in REM querying and *measurement REM* with recovery algorithm and **without** immediate handovers. *Scenario 7.a*, *7.b* and *7.c* investigate the effect of an increasing handover hysterisis threshold that is set to 1, 2 or 3 UE location reports, respectively. *Scenario 7.a, 7.b* and *7.c* can be directly compared against *6.c* to identify whether LABM handover hysterisis thresholds along with the recovery algorithm are able to provide a more stable and improved network performance. *Scenario 7.c* is intuitively expected to have the worst performance, as it delays the decision for transition to the best serving gNB by the longest period of time. However, it is unlikely that the counter will ever manage to reach the value of 3, as channel variations happening during such long periods of time are likely to affect the SINR strongly enough for the LABM algorithm to force a handover to another gNB.

Scenario 8 investigates the effect of the high urbanization error applied to the reported UE locations on REM querying and described in Section 4.1.4. *Scenario 8.a* is meant to show the effect of a stronger UE location error in comparison to *scenario 6.c*. As seen in Figure 4.3, high urbanization error causes the reported UE location to be moved deeper into obstacles for much longer periods. In the case when the UE location error moves it into the obstacle, but the UE is still relatively close to the edge of the obstacle, there is a higher chance that the *measurement REM* still has a non-empty entry in that location. However, due to a stronger location error, the UE is moved closer to the center of the obstacle and the error contribution of the *measurement REM* might be not high enough to "counteract" the erroneous UE location report. Thus, *scenario 8.d* should show, that lack of the recovery algorithm is having a more negative effect than in *scenario 5.a* due to the increased UE location error in REM querying. For completeness, scenarios *8.b* and *8.c* switch off the immediate handover and set threshold to 1 and 2 location reports, respectively.

Scenario 9 investigates the effect of a high delay for location reports by increasing the LTE RRC connection latency to hundreds of milliseconds. It should be noted that this scenario was introduced rather for academic interest as it most likely does not model a realistic scenario given that the typical LTE delays vary between 20 and 60 ms [62]. Such small values are not able to make a significant difference for the performance of the LABM algorithm in the current simulation setup, as the period of actual UE location updates is much longer that those delay values. However, it was decided to introduce a

normally distributed delay that will be high enough to cause the LTE coordinator to receive a location report that will be up to real 2 location changes old, which corresponds to 500 ms. The occasional delay of more than 500 ms implies that the location report may be outdated by up to 2 locations. Given the average speed of $1\ m/s$, this translates to at most the neighbouring cell, thus, simulating and error of only up to 1 meter. Even though the error is small, it may add an extra meter on top of the applied errors in REM construction and querying. Increasing the RRC delay to an even higher value would imply a very high congestion of the LTE link.

Each time the *LteRrcSap::PositionReport* structure reaches the *nrRrcProtocolIdeal* instance, an optional normally distributed value will be used to delay the scheduling of the reception method of the *LteEnbRrc*. It should be noted that the *LteRrcSap::PositionReport* structure is the only one that is affected by the configured delay. Scenario *9.a* extends *3.a* with a high RRC delay and causes the coordinator to receive an older location report for a wrong location. Scenario *9.b* extends *4.a* and causes the coordinator to query the *measurement REM* with an older real location. Due to the fact that query of the *measurement REM* may result in a BPL meant for a location that is geographically closer to the real UE location, the RRC delay may not have a significant impact. Scenario *9.c* and *9.d* are meant to be compared against *5.a* and *6.c*, respectively. These two scenarios are expected to highlight the effect of RRC delay in the presence of both error sources with and without the recovery algorithm, respectively.

4.3 Key Performance Metrics

The main metrics that reflect the end-user experience are presented in the following list:

- **Link quality** reflected in the SINR level in dB directly affects throughput and experienced latency.
- **Throughput** represents the rate of successful message delivery over the communication channel in $Mbit/s$. In the context of this thesis, it is represented by the DL UDP throughput from the gNB to the UE.
- **Latency** refers to the time difference between the generation of the packet on the remote host in the EPC layer and its successful reception at the UE in ms. The latency of the IP layer is used for the analysis.
- **Beam management events** represent the amount of adjustments of BPL on the gNB and UE side.

The simulation has been extended with new trace source described in Section 3.3. As a result, new performance metrics can be derived from the provided insights about the performance of the LABM algorithm.

- **Beam ID offsets** represent the difference in azimuth angular range between beam sector that would have been chosen for the ideal UE location with the *ideal REM* versus the actually selected beam sector by the LABM algorithm. This offset is expected to correlate with the behavior of SINR level and highlight the effect of the UE location error in REM querying and the effect of *measurement REM* on the overall performance.

- **Amount of handover events**, which is proportional to the signaling overhead. Due to the fact that handovers are mostly triggered by the LABM algorithm, it is possible to observe how different configurations of the algorithm influence the total amount of performed handovers.
- **Recovery events** provide information about how often the recovery mechanism had to be involved due to UE location or REM query errors. Those events also contain information about the cartesian length of the vector between the reported and recovered locations, indicating the magnitude of the recovery.

5

Results and Analysis

In this chapter the results of simulation scenarios are presented and analyzed. As mentioned in the previous chapter, simulation scenarios focus on a single UE walk path in the scenario with one UE present in the network. Such setup allows us to perform the direct comparison of performance indicators in each scenario. In Section 5.1 the performance of the default 5G-NR network with and without the SSB RLM is presented. Furthermore, the baseline performance of an ideal configuration for the LABM algorithm is presented, where the LTE coordinator has a perfect error-free knowledge of the UE location. In Section 5.2 the individual and combined effect of reported erroneous UE location for REM querying and of *measurement REM* is investigated. The Section 5.3 takes a look at the benefit of employing the recovery based on the Bresenham's Line Algorithm presented in the Section 3.2.2. The Section 5.4 investigates the variation of threshold levels in the LABM algorithm for the case when the recovery is enabled. In Section 5.5 the effect of a tuned Ornstein-Uhlenbeck model for a higher UE positioning error is investigated, causing prolonged sections of the walk path to be reported inside of obstacles, while recovery and threshold level parameters are varied. The Section 5.6 investigates the effect of a significant delay for the position reporting process by introducing a non-zero delay for the transmission of RRC messages over the LTE connection. Lastly, the Section 5.7 provides a summary of performance of selected simulation scenarios in terms of defined Key Performance Indicator (KPI)s.

5.1 Baselines

In this section the baseline simulation scenarios *0.a, 0.b, 1* and *2* are presented and analyzed.

5.1.1 Default 5G-NR

The Figure 5.1 presents an overview of the simulation area and the best serving gNB for each location of the simulation area according to the error-free *ideal REM*. From the Figure 5.1 it can be expected that with the given walk path, the UE will be served by gNB 2 in the beginning of the simulation. Then, the LOS will be interrupted and the UE will have to execute a handover either to the gNB 1. Later, the UE will be in proximity of the gNB 5 and most probably be served by this gNB. The remaining walk path is expected to be covered by gNBs 4 or 7, as they have the LOS to the UE.

Scenario 0.a simulates the UE walk in the default 5G-NR NSA network setup with realistic IA and no SSB RLM. The realistic IA means that the beam sweep does not happen immediately, but rather the complete exhaustive beam search is done. As described previously in the Section 4.1.3, this process takes $660\ ms$ with current simulation parameters.

The Figure 5.3 presents the SINR experienced by the UE during the complete simulation run time. Lines at $22.7\ dB$, $10\ dB$ and $-5\ dB$ represents maximum rate, beam sweep and

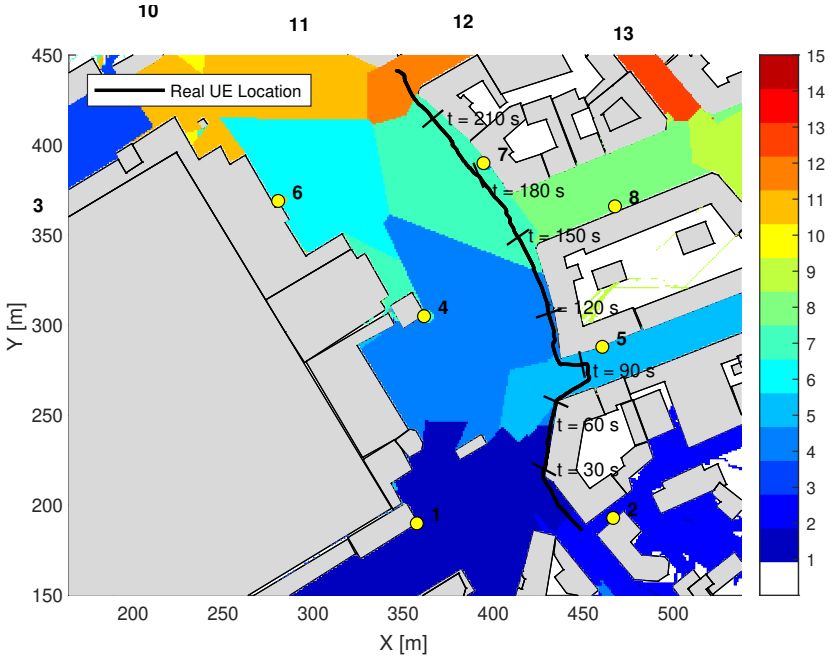

Figure 5.1: Best serving gNB according to the *ideal REM*. Black line represents the real UE location. Lines orthogonal to the walk path mark the locations at 30, 60, 90, 120, 150, 180 and 210 seconds. gNB locations represented as yellow dots.

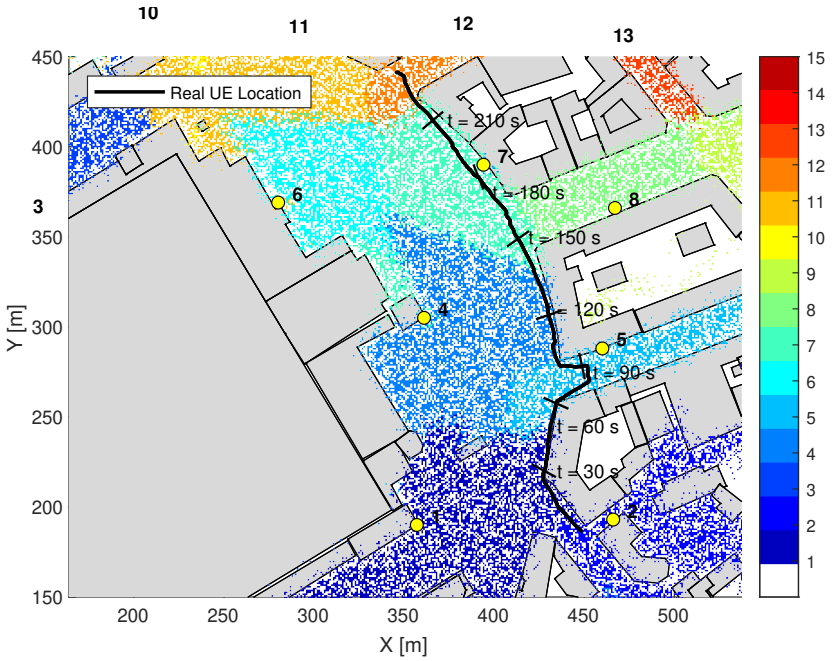

Figure 5.2: Best serving gNB according to the *measurement REM*. Black line represents the real UE location. Lines orthogonal to the walk path mark the locations at 30, 60, 90, 120, 150, 180 and 210 seconds. gNB locations represented as yellow dots.

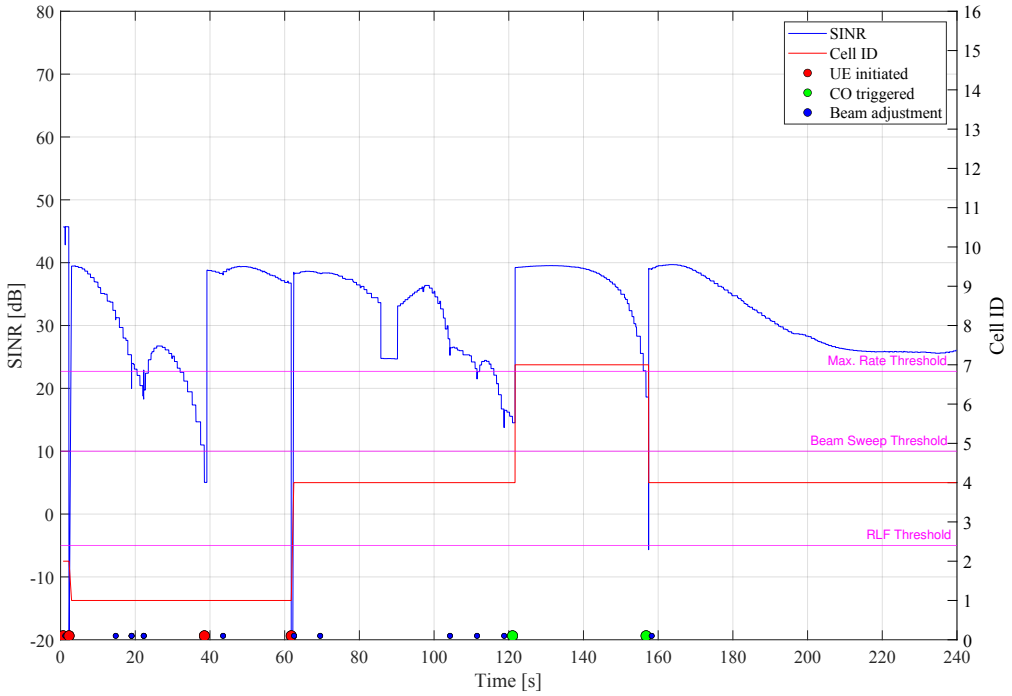

Figure 5.3: SINR in dB and serving gNB IDs for the UE in *scenario 0.a*, along with SINR thresholds, beam adjustment and beam sweeping events.

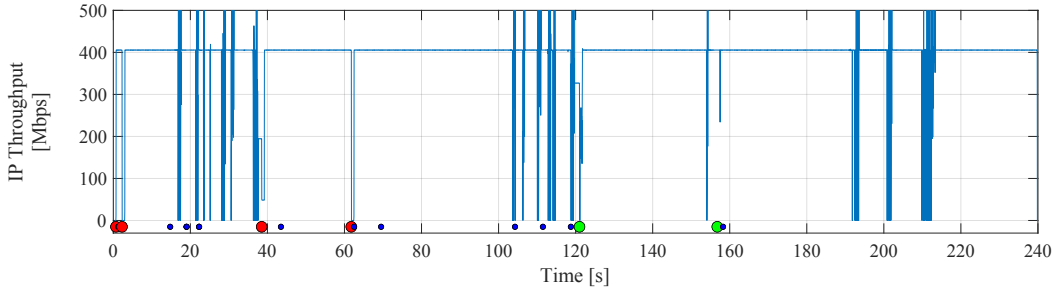

Figure 5.4: IP throughput in Mbit/s for the UE in *scenario 0.a*. Red dots represent exhaustive beam sweep events and blue dots represent beam adjustments.

RLF thresholds for the SINR level. These thresholds are relevant for the logic of the LABM algorithm and the evaluation of network performance. The Figure 5.3 also presents the IDs of serving gNB, to which the UE is connected at every time point of the simulation. Additionally, the figure plots events such as UE-initiated exhaustive beam sweeps as red dots, CO-initiated exhaustive beam sweeps as green dots and beam adjustments at UE or serving gNB as blue dots. From the Figure 5.3 it can be observed, that at the beginning of the simulation the UE performs an exhaustive beam sweep to determine the best serving gNB and identifies the gNB 2 as the best candidate. However, due to the fact that the UE moves out of the LOS of gNB 2 within several seconds of the simulation, the initially chosen BPL becomes invalid and the signal quality falls below the RLF threshold. As a result, the UE has to perform another exhaustive beam sweep to identify the new serving gNB. After the sweeping at $t = 2.25\ s$ procedure the UE connects to the gNB 1 and additionally monitors 3 other beams from this gNB. As the UE continues moving along its walk path, the selected beam from the gNB 1 becomes outdated enough to cause beam misalignment that leads to the signal degradation below the maximum rate threshold of $22.7\ dB$. Due to the fact that alternative beams monitored with CSI-RS signals were detected to provide a higher SNR, the UE and gNB adjust their beams at $t = 22.25\ s$, which leads to a temporary improvement of the received signal quality at the UE. However, the current BPL becomes outdated as the UE starts moving in a diagonal radially outward direction from the serving gNB, causing the SINR to fall below the beam sweep threshold of $10\ dB$ at $t = 38.3\ s$. As a result, an exhaustive beam sweep is performed to identify the new optimal BPL. The gNB 1 is still detected to deliver the highest SNR and the UE is served by it until at around $t = 61.7\ s$, where the UE moves around the building corner, losing the LOS to the gNB 1. As a result, yet another exhaustive beam sweep is triggered and the UE connects to the gNB 4. The gNB 4 remains to be the serving gNB until $t = 121\ s$. With help of the information from CSI-RS about alternative 3 beams that were detected to deliver high SNR, the gNB and UE are able to maintain a relatively high signal quality for a prolonged period of time. However, due to the SINR level being below the maximum rate threshold for long enough, the LTE coordinator initiates a beam sweep to identify a better BPL at $t = 121\ s$. As a result, a handover to the gNB 7 is executed. Due to the proximity to the serving gNB 7 and seemingly no alternative BPLs with high-enough SNR, the signal quality drops below the RLF threshold at $t = 157.4\ s$ and the coordinator commands a beam sweep. After this beam sweep, the UE re-connects to the gNB 4 and remains served by this gNB until the end of the simulation with slight degradation of the SINR level due to the radial outward movement of the UE away from the serving gNB.

Scenario 0.b adds the SSB RLM to *scenario 0.a*. The SSB RLM makes it possible to update the information about beams that are meant to be monitored by the CSI-RS signals based on the measurement reports sent by the UE based from periodic beam sweeps. Such network configuration provides high frequency updates about current channel conditions, allowing the UE and the LTE coordinator to react much faster on any potential signal quality degradation. As can be seen on the Figure 5.5, SSB RLM provides a vast improvement in the link quality and stability. Due to the fact that the network is now updating its knowledge about the current channel state every $20\ ms$, the network is able to maintain an almost constant SINR of around $40\ dB$ with only a couple of exceptions. In the beginning of the walk path, the UE loses the LOS to the serving gNB 2 and an exhaustive beam sweep has to be performed, as the SNR on the UE is detected to be $-25.89\ dB$. At $t = 61.7\ s$ the UE enters the LOS of the gNB 5 and leaves the LOS of its serving gNB 1, causing a strong

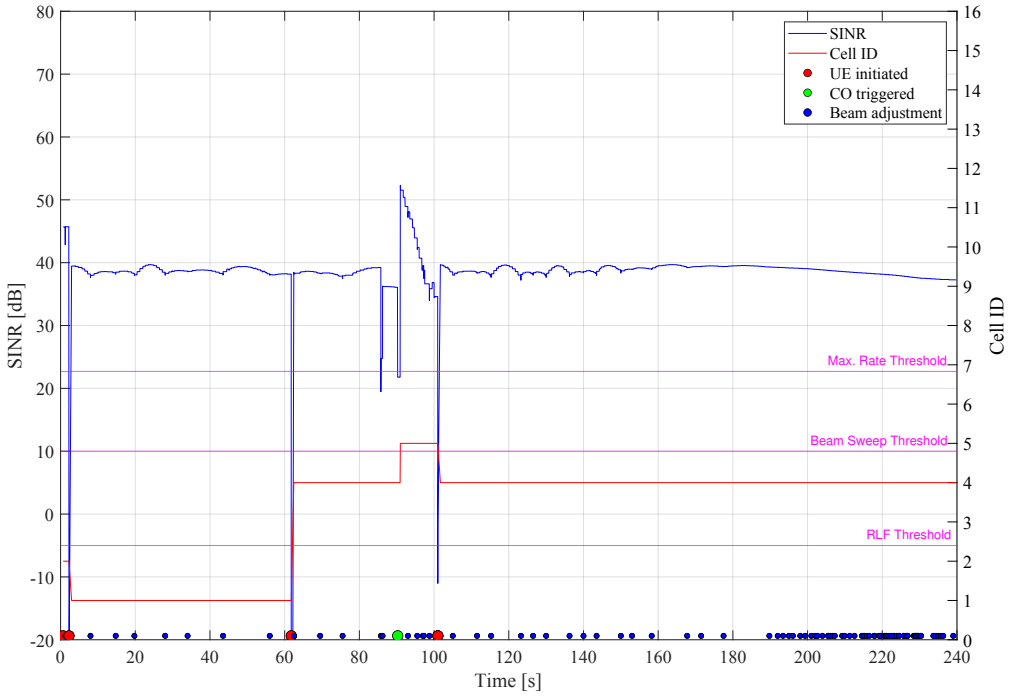

Figure 5.5: SINR in dB and gNB IDs for the UE in *scenario 0.b*, along with SINR thresholds, beam adjustment and beam sweeping events.

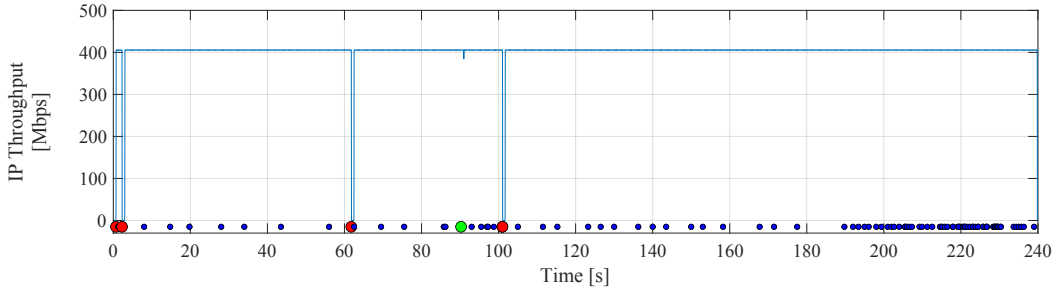

Figure 5.6: IP throughput in Mbit/s for the UE in *scenario 0.b*. Red dots represent exhaustive beam sweep events and blue dots represent beam adjustments.

signal degradation below SINR $= -111.8\ dB$. Due to such strong signal degradation below the RLF threshold of $-5\ dB$, an exhaustive beam sweep is initiated by the UE, resulting in a connection to the gNB 4. Due to the fact that theLOS to the gNB 4 is interrupted, the signal quality drops below the maximum rate threshold at around $t = 90\ s$. The LTE coordinator commands a beam sweep, which then identifies the gNB 5 to deliver the best SNR in the current area. After the UE leaves the LOS area of the gNB 5, the link is broken again, causing an exhaustive beam sweep. The result of this sweep is the re-connection to the gNB 4, which remains the serving the gNB until the end of the simulation. This is possible due to the fact that the information about beams that are meant to be monitored with CSI-RS signals is continuously updated, allowing the UE and gNB to continuously update the active BPL even with the lateral movement of the UE with respect to the serving gNB. The high amount of beam update events towards the end of the simulation is caused by the fact that the UE seems to continuously switch its antenna azimuth sectors as the gNB continuously toggles between its antenna azimuth sectors 19 and 20. In any case, the perceived SINR level at the UE side remains almost constant at $40\ dB$. The continuous RLM based on SSBs allowed to maintain real-time information about current propagation characteristics of the environment and maintain very stable connection to serving gNBs, with only 3 exhaustive beams sweeps, 3 short RLF events and 4 handovers. The Figure 5.6 provides an overview of the experienced IP throughput in Mbit/s on the the UE. The blue line presents the IP throughput, along with exhaustive beam sweeps as red dots and beam adjustments at UE or gNB as blue dots. As can be seen in the Figure 5.6, the resulting IP throughput is at its target $400\ Mbit/s$ during the most part of the simulation. Due to continuous high frequency monitoring of optimal beams, *scenario 0.b* is representing the best performance that can be achieved in all simulated scenarios.

In conclusion for *scenario 0.a*, 6 exhaustive beam sweeps were performed, where 2 were caused by RLF events. In total 4 handovers were executed during the simulation runtime. To further analyze these results, the Figure 5.4 shows that the IP throughput was negatively affected each time an exhaustive beam sweep was performed and each time the signal quality has dropped below the maximum rate threshold. This also leads to several seconds of severe degradation of the IP throughput at around $t = 37\ s$ and $t = 120\ s$ of the simulation time. From the SINR pattern it can generally be observed, that due to the movement of the UE, the selected BPLs gradually become outdated. As the beams monitored by CSI-RS signals are only updated directly after the beams sweep, this information is also not able to help to maintain a high SINR level. In contrast, *scenario 0.b* shows an extremely stable link quality throughout the most part of the simulation due to high-frequency updates of beams that are supposed to be tracked by the RLM procedure with CSI-RS signals. *Scenario 0.b* performs 5 exhaustive beam sweeps and 4 handovers with an almost constant SINR of almost $40\ dB$ throughout the most part of the simulation runtime. *Scenario 0.b* represents the upper performance bound for all the following scenarios achieved at the expense of the highest overhead from processing SSB signals

5.1.2 Ideal LABM

Scenario 1 represents the ideal case for the deployment of the LABM algorithm, where no UE location error in REM querying is present, the *ideal REM* is used and the UE reports its location to the LTE coordinator with the same frequency as its actual location updates managed by UE's mobility model. *Scenario 2* represents the case where the UE location is

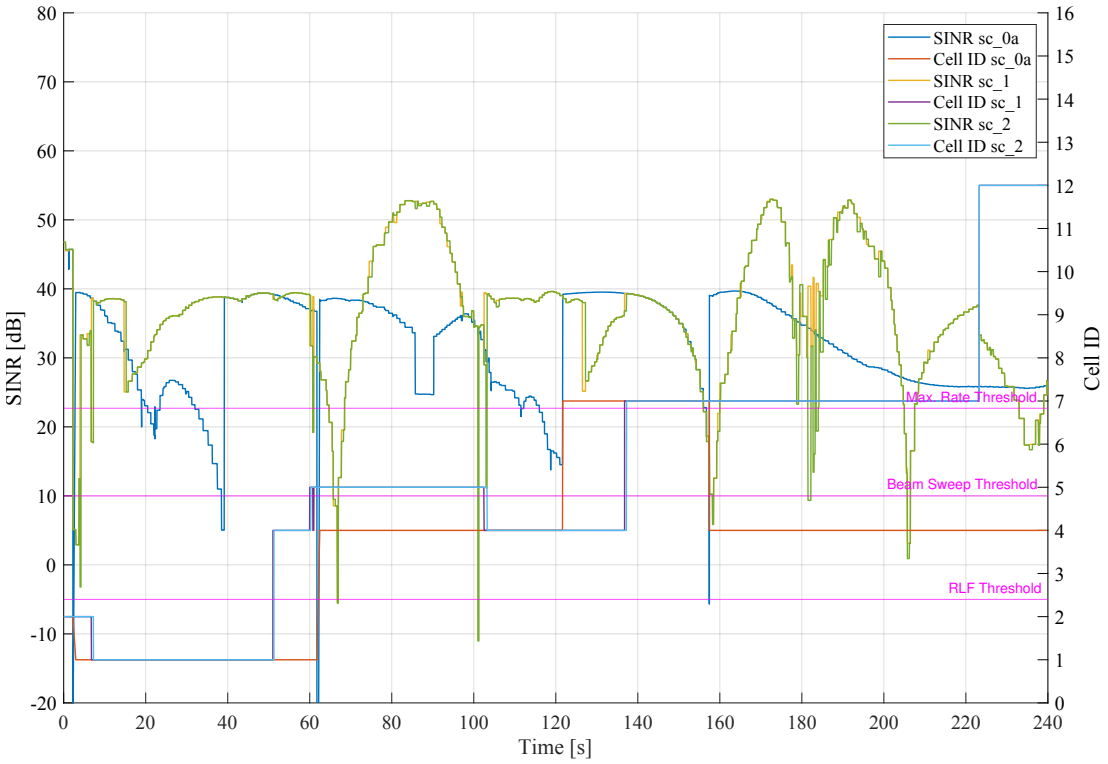

Figure 5.7: SINR in dB and serving gNB IDs for the UE in *scenario 0.a, 1, 2*. Blue and red lines represent SINR and gNB ID for *scenario 0.a*, respectively. Yellow and purple lines represent SINR and gNB ID for *scenario 1*, respectively. Green and cyan lines represent SINR and gNB ID for *scenario 2*, respectively.

reported with a more realistic frequency of 1 Hz. Also in *scenario 2* no UE location error in REM querying is present and the *ideal REM* is used. The Figure 5.7 shows SINR and serving gNB IDs for the UE in *scenarios 0.a, 1* and *2*, providing a comparison between the default 5G-NR configuration with no SSB RLM and ideal configurations of the LABM algorithm.

It can be observed that until $t = 157\ s$ of simulation runtime, the ideal configuration LABM in *scenario 1* is able to provide a higher signal quality in places where the identified BPLs in *scenario 0.a* were gradually becoming outdated. The LABM algorithm eliminates the requirement for exhaustive beam sweeping at the start of the simulation by providing the BPLs and target serving gNB over LTE control link. Thus, the initial delay of 660 ms is eliminated and the UE is able to receive the DL traffic almost immediately at the simulation start. Additionally, both in *scenario 1* and *scenario 2*, the signal quality is kept above the RLF threshold of $-5\ dB$ at around $t = 2\ s$, whereas *scenario 0.a* has to perform an additional exhaustive beam sweep due to the lost LOS to the serving gNB 2. It can be also observed that the LABM algorithm is able to capture a more up-to-date information about the current propagation characteristics of the channel by querying the *ideal REM* and

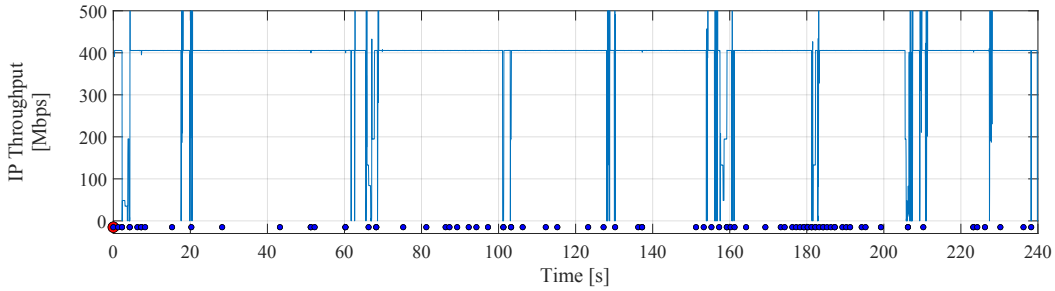

Figure 5.8: IP throughput in Mbit/s for the UE in *scenario 2*. Red dots represent exhaustive beam sweep events and blue dots represent beam adjustments.

providing an optimal BPL, avoiding the degradation of the signal quality below the beam sweep threshold compared to *scenario 0.a* at $t = 38.8\ s$, $t = 85.75\ s$ and $t = 127.25\ s$. Due to a different selection of serving gNB between $t = 60\ s$ and $t = 105\ s$, the LABM algorithm is also able to achieve higher peak SINR values at the expense of less stable connection. However, in some occasions the serving gNB selected according to the LABM algorithm is not able to provide as good SINR as the default 5G-NR network in *scenario 0.a*. The fluctuation of signal quality at around $t = 60\ s$ in *scenario 1* is caused by re-connections between the gNB 4 and 5. At around $t = 100\ s$ the UE approaches the corner of the building, where the LOS to the current serving gNB 5 ends. *Scenario 1* manages to keep the SINR above the maximum rate threshold by executing a handover to the LOS gNB 4 at $t = 102\ s$, while in *scenario 2* the coordinator has to wait additional $750\ ms$ until the next UE location report arrives. Thus, *scenario 2* does not manage to avoid a strong SINR degradation in this area, leading to a RLF event. Later, starting from $t = 157\ s$, another difference between the behavior of LABM algorithm and the default 5G-NR configuration can be observed. *Scenario 0.a* identifies the gNB 4 as the one that provides the best signal quality, while LABM remains at gNB 7. Due to the proximity to serving gNB 7, even slight beam offset might cause a severe signal quality degradation. This is highlighted by the difference between the performance of *scenario 1* and *2*, where *scenario 2* does not manage to update the BPLs fast enough to avoid degradation of signal quality below the maximum rate threshold, while *scenario 1* manages to remain above it. *Scenario 0.a* performs even worse in this region, as BPLs are not updated until a RLF occurs. Later, at $t = 223\ s$ both *scenario 1* and *2* identify the gNB 12 as the best serving candidate according to the path loss metric from the *ideal REM*. This cause a less stable SINR behavior in comparison to *scenario 0.a*.

It can be observed in Figure 5.7 that in general *scenario 1* and *2* have a very similar behavior in terms of time points where the handovers occur and selected target gNBs. The only difference is that in *scenario 1* handovers are executed approximately $250\ ms$ earlier do to the increased UE location reporting frequency. However, there are two additional handovers performed at $t = 60.77\ s$ and $t = 61\ s$ in *scenario 1*. This can be explained by the fact that the LABM detects a gNB that promises higher signal quality for the UE location, that is not reported in *scenario 2* due to the lower reporting frequency. In total, *scenario 1* and *scenario 2* perform 8 and 6 handovers, respectively. It can also be observed

that the number of times the signal quality degraded below the RLF threshold for both *scenario 1* and *scenario 2* is 1 and 2, respectively, which is an improvement in comparison to 3 RLF events that happen in *scenario 0.a*.

The Figure 5.8 shows the IP throughput for *scenario 2*. It can be observed that due to the eliminated exhaustive beam sweep in the beginning of the simulation, the UE is able to receive the date almost immediately after the simulation start in contrast to the $660\ ms$ delay in *scenario 0*. However, stronger fluctuations in the SINR level in that area still lead to a sub-optimal IP throughput. At around $t = 65\ s$ and $t = 100\ s$ the throughput degrades due to the usage of outdated BPLs in the area where the UE moves away from the LOS area of the serving gNB. Due to the fact that with the LABM a different gNB was selected as a serving gNB in comparison to *scenario 0.a*, the IP throughput is also negatively affected at around $t = 157\ s$ and $t = 180\ s$.

5.2 Effect of Error Models

In this section the individual and combined effect of erroneous UE locations for REM querying and the *measurement REM* are analyzed.

5.2.1 Reported Erroneous UE Locations for ideal REM Querying

Scenario 3.a extends *scenario 2* by incorporating the error model with medium urbanization level for UE location reports in REM querying. The scenario uses the *ideal REM* and immediate LABM handovers. The recovery algorithm is not enabled. The applied error model is derived from the Ornstein-Uhlenbeck stochastic process parametrized according to the Table 4.2 for medium urbanization scenario. The resulting walk path is presented as green line in the Figure 4.3. From the Figure 4.3 it can be seen that the applied error to the UE location reports causes the reported UE location to be moved into building directly at the beginning of the path.

Due to the fact that the *ideal REM* does not contain a valid REM entry for locations that are inside of buildings, the LABM algorithm is not able to provide a BPL and target gNB to which the UE should perform the initial connection. Thus, in this case the UE has to perform an exhaustive beam sweep for the IA procedure, delaying the link establishment and start of data transmission by 660 ms. The Figure 5.9 compares the SINR and serving gNBs of *scenario 2* and *scenario 3.a*. As can be seen in Figure 5.9, at $t = 1.25\ s$ the coordinator receives a new location report from the UE. The real location of the UE is still in the LOS conditions for the serving gNB 2. However, the reported erroneous location represents a location that is further to the north-west in the NLOS area of the gNB 2. As a result, the LABM queries the *REM* and returns a BPL that results in a strong beam misalignment of 8 azimuth sectors at the UE. This causes the UE's antenna beam to be pointed towards wrong direction, leading to the signal quality degradation from SINR $= 45\ dB$ to $5\ dB$. At $t = 3.25\ s$ the SINR drops to $-66\ dB$ as the UE reports an erroneous location that is further in the nort-west direction of its real location, causing the LABM algorithm to select a BPL that has a beam offset of 5 azimuth sectors for the gNB and 1 azimuth sector for the UE with respect to the ideal BPL for the real UE location. At $t = 3.7\ s$ the real UE location gets closer to the previously reported erroneous location. Thus, the previously selected BPL becomes optimal for the current real UE location and the SINR increases to $33\ dB$, similarly to what both *scenario 1* and *2* are able to achieve at the same UE location.

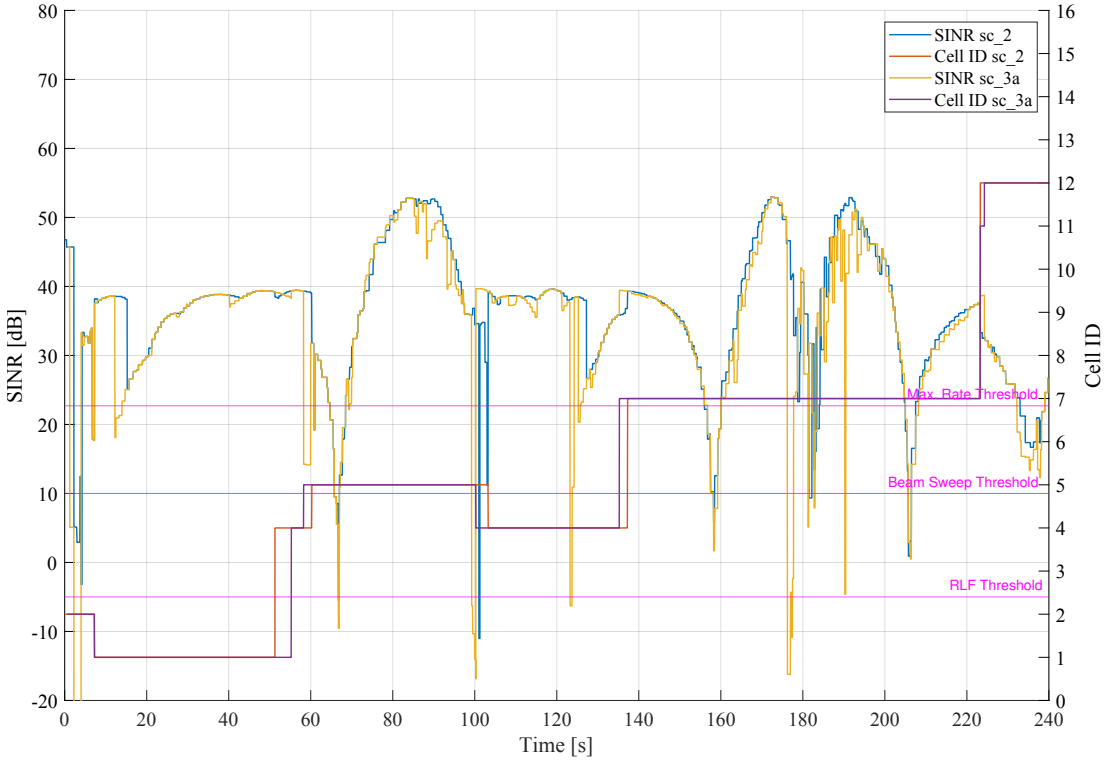

Figure 5.9: SINR in dB and serving gNB IDs for the UE in *scenario 2, 3.a*. Blue and red lines represent SINR and gNB ID for *scenario 2*, respectively. Yellow and purple lines represent SINR and gNB ID for *scenario 3.a*, respectively.

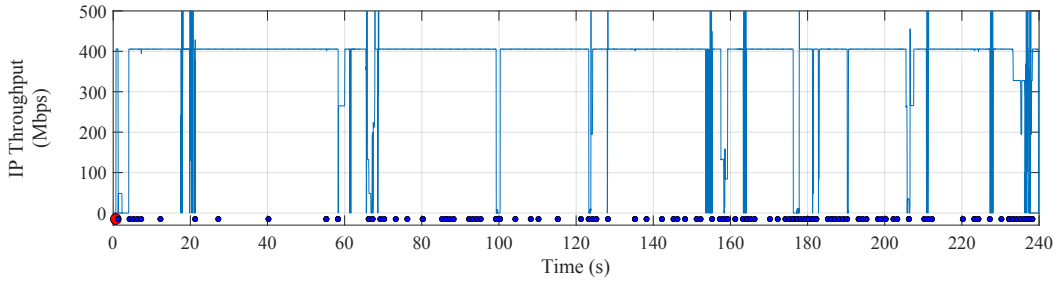

Figure 5.10: IP throughput in Mbit/s for the UE in *scenario 3.a*. Red dots represent exhaustive beam sweep events and blue dots represent beam adjustments.

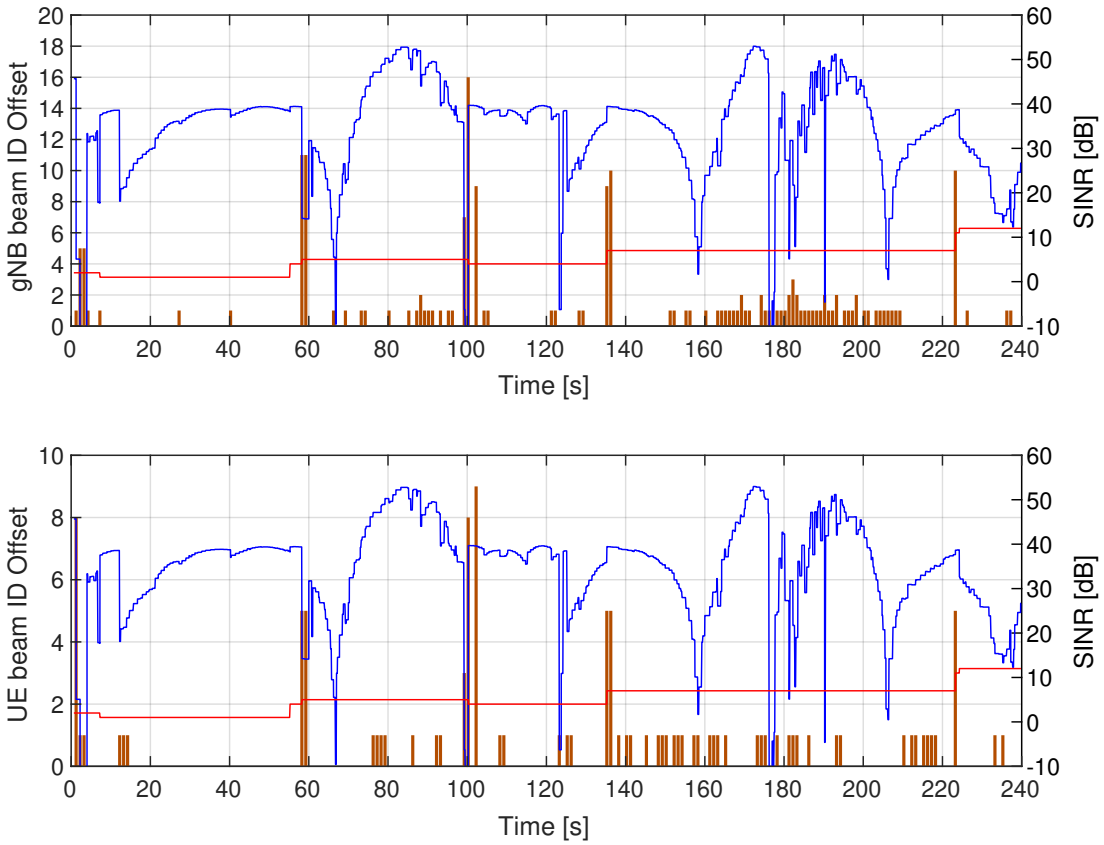

Figure 5.11: Beam ID offset of azimuth sectors with respect to the optimal beam ID for gNB (top) and UE (bottom) in dark orange, SINR in blue, current serving gNB in red for *scenario 3.a*.

It can also be observed that at $t = 67\ s$ and $t = 100\ s$, the erroneous UE location in REM querying causes more severe signal level degradation and increases the amount of RLF events. At $t = 123.25\ s$ the UE is served by the gNB 4 and due to the erroneous reported location has an offset of 1 azimuth sector for the UE antenna configuration, which was enough to cause a significant SINR degradation below the RLF threshold. In the further section the UE is served by the gNB 7 and move in its proximity in lateral direction with respect to the gNB's beam direction. As mentioned previously, the precise beam alignment in proximity of the serving gNB is crucial, as even small lateral movements are enough to move out of the coverage area of the currently active gNB beam. This fact is proven by the SINR degradation below the RLF threshold at $t = 176.25\ s$ after the BPL with beam offset of 1 azimuth sector was selected for the gNB due to the UE location error in REM query. Similar event can be spotted at $t = 190\ s$. Overall, total the amount of RLF events has almost tripled in comparison to the *scenario 2*.

The Figure 5.11 a) and b) shows beam ID offsets in azimuth sectors between the ideal configuration and the BPL delivered by the LABM algorithm for UE and gNB, respectively,

alongside the SINR level at the UE and serving gNB ID. It can be observed in Figure 5.11 a) and b) that even small beam offsets of 1-2 azimuth sectors may have a very strong influence on the signal quality in proximity of the serving gNB between $t = 170\ s$ and $t = 200\ s$ of simulation time. Other occurances of high beam offsets in the Figure 5.11 mostly correlate with handover events. This is explained by the fact that at time points when the coordinator receives a UE location report and detects that the UE should be served by a different gNB, the BPL of that gNB may be diametrically opposite to the currently used BPL. The high offset is then due to a big difference between the ideal azimuth sectors of the BPL of the ideal serving gNB to which the UE will execute a handover, and the BPL that is currently in use with the current sub-optimal serving gNB. At $t = 102.25\ s$ the beam offset is indicated to be 9 azimuth sectors for both UE and gNB as the ideal UE location is expected to be served by the gNB 5 at UEs ideal location, while the reported erroneous UE location in the REM query returned an optimal BPL for the currently serving gNB 4.

In *scenario 1* and *2*, each REM query with the reported UE location is successful due to the fact that the reported location corresponded to the real UE location. As the *ideal REM* is used, each REM query with the reported UE location is expected to succeed in *scenario 1* and *2*. However, this is not the case in *scenario 3.a*, as some of reported erroneous UE locations are inside of buildings. The *ideal REM* does not have valid entries for such locations. As the LABM recovery algorithm is not enabled in *scenario 3.a*, this has caused the total of 36 REM queries to fail and the LABM to terminate, without providing a BPL.

When compared to the IP throughput in *scenario 2* in Figure 5.8, it can be seen in Figure 5.10 that *scenario 3.a* has a significant throughput degradation in the first seconds of the simulation. Due to the exhaustive beam sweep, no data exchange is possible within first 660 ms. As mentioned previously, the severe beam misalignment in first seconds of the simulation resulted in the low and unstable IP throughput. Further behavior looks similar to *scenario 2* with longer outages and additional drops in the time interval when the UE is in proximity of serving gNB 7. In terms of handovers, in *scenario 3.a* the error in UE location report causes an extra handover to the gNB 11, as it is detected to be the best serving gNB for the reported location. Due to the fact that immediate handovers are enabled for *scenario 3.a*, the UE changes its serving gNB even though the SINR is above the maximum rate threshold. As a result, *scenario 3.a* execute one extra handover in comparison to *scenario 2*.

Scenario 3.b and *scenario 3.c* disable immediate LABM handovers and set the LABM handover hysterisis threshold to 1 and 2 location reports, respectively. As mentioned in the Section 4.2, for such configurations the signal quality may degrade significantly, as with the given UE location reporting frequency of 1 Hz, it delays the decision to perform a handover to the optimal gNB for 1 s or 2 s, respectively.

In terms of handovers, it can be noticed in Figure 5.12 that *scenario 3.b* delays the handover from gNB 1 to gNB 5 at around $t = 60\ s$, whereas in *scneario 3.a* the UE switches the serving gNB twice with an intermediate connection to the gNB 4. However, in *scenario 3.b* and *3.c* the UE does not perform a handover at $t = 55.25\ s$ as the signal quality is well above the maximum rate threshold of $22.7\ dB$. However, the decision to remain at the serving gNB 1 as long as possible causes an RLF event as the UE moves out of the LOS of the gNB 1, and the SINR drops significantly. Similar case occurs at around $t = 145\ s$, where the LABM handover hysterisis threshold prevents a connection to the most optimal gNB for the reported UE location and continues using the available BPL for the serving gNB 4. At $t = 143.5\ s$ the SINR level drops below the maximum

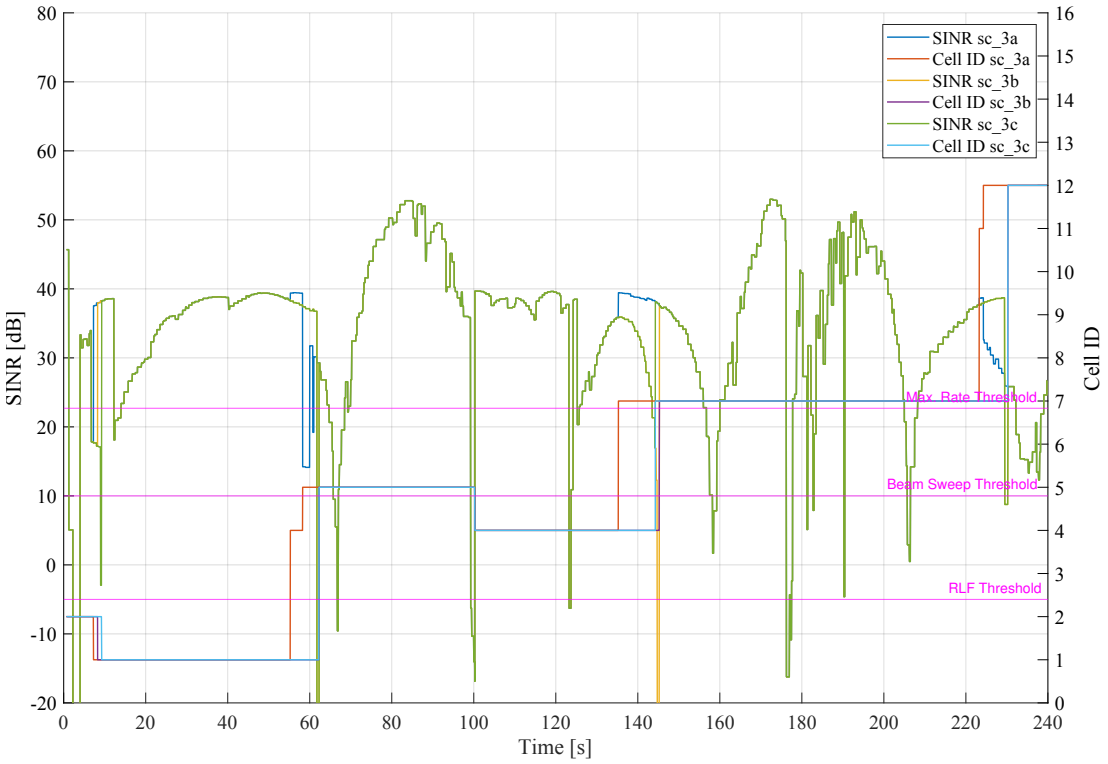

Figure 5.12: SINR in dB and serving gNB IDs for the UE in *scenario 3.a, 3.b, 3.c*. Blue and red lines represent SINR and gNB ID for *scenario 3.a*, respectively. Yellow and purple lines represent SINR and gNB ID for *scenario 3.b*, respectively. Green and cyan lines represent SINR and gNB ID for *scenario 3.c*, respectively.

rate threshold, but the LABM algorithm is not able to perform any action, as the next UE location report will arrive only at $t = 144.25\ s$. Once it arrives, the LABM detects a sub-optimal signal quality, but due to the configured hysterisis threshold delays the decision to switch to another cell until the next report arrives at $t = 145.25\ s$. However, the problem is that at $t = 144.75\ s$ the SINR drops strongly enough to get below the RLF threshold. Once this situation is detected by the LABM algorithm at $t = 145.25\ s$, the algorithm forces a connection to the optimal gNB with the best possible BPL. Later, at $t = 223.25\ s$, the hysterisis threshold delays the decision to perform a handover to gNB 12, thus, leading to stronger SINR degradation below $10\ dB$. As a result, in *scenario 3.b* two additional RLF events happened with respect to *scenario 3.a* due to a delayed decision to switch to an optimal gNB. As can be seen in the Figure 5.12, *scenario 3.c* shows a very similar behavior to *scenario 3.b* with an additional slight signal degradation at the beginning of the simulation at $t = 9\ s$ due to a delayed handover from the gNB 2 to gNB 1. The beam ID offsets for *scenario 3.b* and *3.c* have a very similar magnitude of azimuth sector offsets for gNBs and the UE as in the *3.a*, therefore the corresponding plots are omitted.

In summary, *scenario 3* demonstrates that UE location errors may lead to the failure of the LABM algorithm in speeding up the IA process, as the reported UE location may be inside of an obstacle, leading to unsuccessful REM querying. Additionally, the location errors in REM querying are shown to have the most significant impact in areas where the UE loses the LOS to its current serving gNB, as the LABM algorithm is not able to provide appropriate optimal BPL in this case. Furthermore, UE location errors are shown to have a strong impact on the network performance in proximity to the serving gNB, as such cases are more sensitive to even slight beam misalignments. As soon as the decision to execute a handover to the most optimal gNB gets delayed due to the introduction of LABM hysterisis thresholds, the performance degrades even further. Such behavior aligns with expectations.

5.2.2 Measurement REM

Scenario 4.a extends *scenario 2* with the UE location reporting frequency of 1 Hz. The reported UE locations in this case are not affected by location errors. However, instead of the *ideal REM*, the *measurement REM* is used. The scenario uses immediate LABM handovers, and the recovery algorithm is disabled. For the given scenario, the *measurement REM* will cause queries for the error-free reported UE location to fail in locations where the *measurement REM* does not have a valid data in the corresponding REM entry. Moreover, in the case when the query succeeds, it can provide the BPL information for a wrong location. This happens due to the fact that the creation of the *measurement REM* is affected by errors in locations, for which a measurement is reported, as explained in Section 3.1.3.2. As a result, even if the REM query succeeds, there is no guarantee that it will return an optimal BPL for the current real location of the UE. Additionally, as can be seen in the Figure 5.2, the virtual borders between areas most optimally served by specific gNBs are not as sharp as they were in the *ideal REM* in the Figure 5.1. This is expected to result in situations where the LABM might command a handover to a gNB that is not yet in the LOS of the UE or cause repeating re-connections to several gNBs within short periods of time.

Figure 5.13 demonstrates the SINR performance of *scenario 4.a* compared to *scenario 2*. It can be observed that at the beginning of the simulation at $t = 2.25\ s$ a significant signal quality degradation occurs in *scenario 4.a*. This happens due to the failure of the LABM algorithm to query the *measurement REM* at the reported error-free UE location. In this exact location, the UE happens to move out of the LOS of serving gNB 2, causing a severe beam misalignment and failing to switch to a NLOS BPL. The query also fails for the next reported UE location, thus, leaving UE and gNB 2 with a sub-optimal BPL for almost 2 seconds, leading to RLF. In the next segment of the UE walk path, the UE connects to gNB 1 in *scenario 2*, as this gNB is now in the LOS of the UE. The *measurement REM* in *scenario 4.a* delivers a REM entry that also causes the UE to connect to gNB 1. However, at $t = 8.25\ s$ the *measurement REM* entry falsely reports that the optimal gNB for the reported UE location is again gNB 2. Due to the fact that immediate LABM handovers are enabled, the UE switches back to the gNB 2. This causes the SINR level to drop from $15\ dB$ to $-4\ dB$, almost causing another RLF event. Once the UE moves further in the north-east direction, it reaches the area that is predominantly covered by the gNB 1 and gNB 4. Thus, the signal quality mostly remains above the maximum rate threshold of $22.7\ dB$ when the UE re-connects to the gNB 1. Once the UE approaches the building's corner, where the LOS to the closer located gNB 5 is about to appear, the

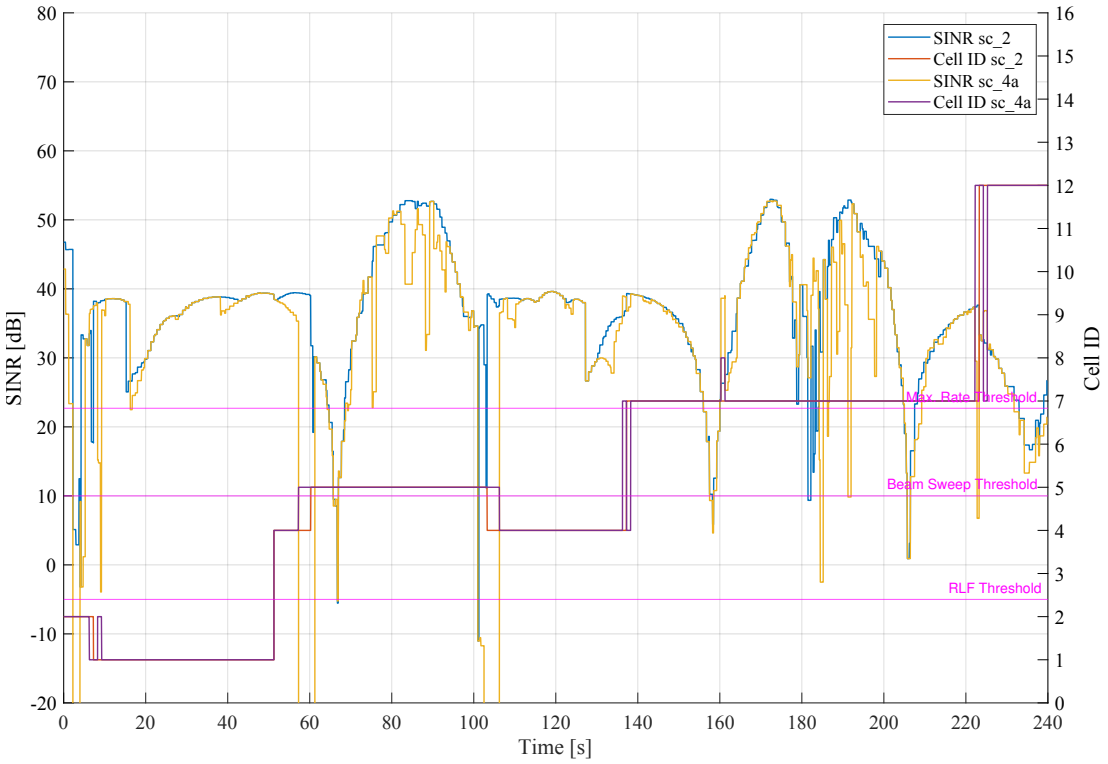

Figure 5.13: SINR in dB and serving gNB IDs for the UE in *scenario 2, 4.a*. Blue and red lines represent SINR and gNB ID for *scenario 2*, respectively. Yellow and purple lines represent SINR and gNB ID for *scenario 4.a*, respectively.

measurement REM causes an early handover to gNB 5 at $t = 57.25\ s$. This happens due to the fact that REM entries that are originally LOS locations closer to gNB 5 in *ideal REM* are moved behind the building's corner into NLOS area for gNB 5 in *measurement REM*. As a result, the SINR level drops immediately below the RLF threshold from $35.3\ dB$ to $-111.8\ dB$. Once the UE actually reaches the LOS area of gNB 5, the SINR improves significantly. Around $t = 105\ s$ of simulation time, the UE starts moving out of the LOS of gNB 5. Similar to the previous case, REM entries reported for wrong locations stored in the *measurement REM* cause the choice of a sub-optimal BPL, leading to beam misalignment and delaying the handover to the gNB 4, which is in a LOS. As a result, the UE spends more than 5 seconds with the SINR level below the RLF threshold. At later time points, the *measurement REM* again causes sub-optimal BPL choice in the proximity of gNB 7 at around $t = 185\ s$, leading to stronger SINR degradations than those that are observed in the ideal LABM configuration in *scenario 2* at the same time in the path.

In addition to more frequent SINR degradation below the beam sweep and RLF thresholds, Figure 5.13 shows an increased amount of handover events in *scenario 4.a*. Namely, 14 handovers were executed in total in *scenario 4.a*. The amount is doubled compared to 7 handovers in *scenario 3.a* and more than tripple compared to 4 handovers in *scenario*

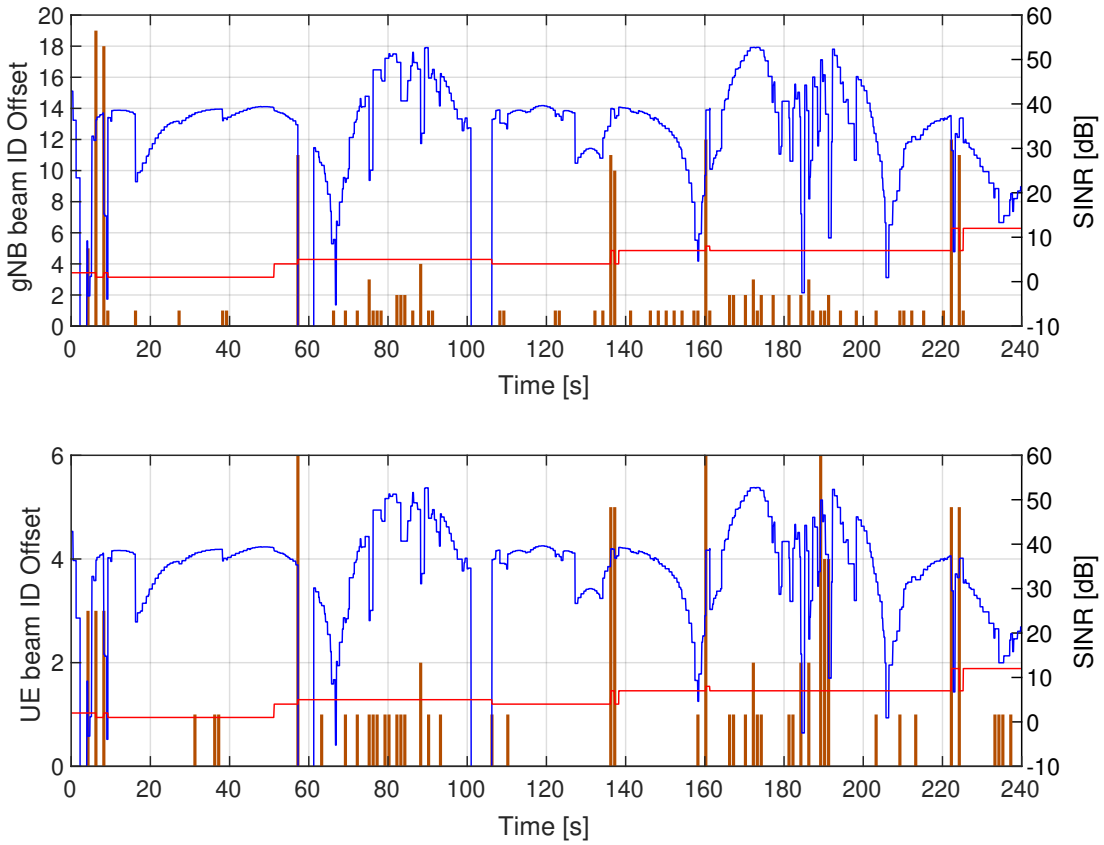

Figure 5.14: Beam ID offset of azimuth sectors with respect to the optimal beam ID for gNB (top) and UE (bottom) in dark orange, SINR in blue, current serving gNB in red for *scenario 4.a*.

2. It can also be seen that those additional handovers reflect the cases when the UE is disconnecting from its serving gNB for shorts periods of time, as the *measurement REM* is falsely reporting wrong gNB as the best candidate. This is leading to the frequent switching back and forth between gNBs that serve areas, where the LOS to one of them is lost or in regions when the UE happens to be on a virtual border between the serving areas of two or more gNBs.

From the Figure 5.14 showing gNB and UE beam ID offsets alogn the path in *scenario 4.a*, it can be seen that most of the cases where high beam ID offsets occur are correlating with handover events. This is an expected phenomenon as explained previously, as the beam IDs from two different gNBs are compared to each other. It can be observed that usually up to 4 azimuth sectors offset at gNB and up to 2 azimuth sectors at UE are present.

Scenario 4.b and *4.c* do not use immediate LABM handovers and introduce the LABM handover hysterisis thresholds of 1 and 2 location reports, respectively. As mentioned in Section 4.2, it is expected that the delayed decision to handover to another gNB might be beneficial due to that fact that it would prevent the previously mentioned toggling between

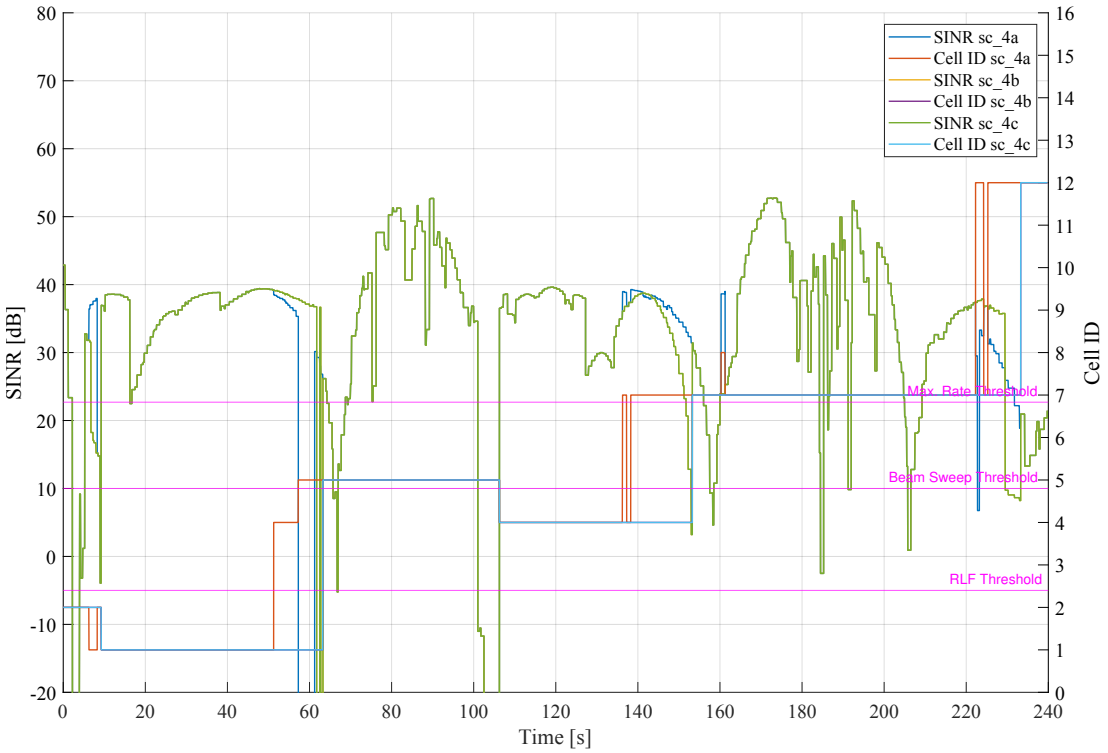

Figure 5.15: SINR in dB and serving gNB IDs for the UE in *scenario 4.a, 4.b, 4.c*. Blue and red lines represent SINR and gNB ID for *scenario 4.a*, respectively. Yellow and purple orange lines represent SINR and gNB ID for *scenario 4.b*, respectively. Green and cyan lines represent SINR and gNB ID for *scenario 4.c*, respectively.

two gNBs due to errors caused by querying the *measurement REM*. Figure 5.15 presents the SINR and IDs of serving gNBs for *scenario 4.a, b, c*. It can be observed that the amount of handovers is decreased for *scenario 4.b* and *4.c* with respect to *scenario 4.a*. In the beginning of the simulation at $t = 6.25\ s$, the delayed handover decision prevents from a temporary switch from the gNB 2 to gNB 1 and back, but rather maintains the connection to gNB 2. The behavior at around $t = 60\ s$ is now also different with respect to *scenario 4.a*, as both *scenario 4.b* and *4.c* try to maintain the connection to the serving gNB 1. This in turn results in a more stable SINR for a longer period of time, as the BPL is not adjusted from the one that serves the UE in LOS conditions gNB to a wrong gNB 5 that is still in NLOS conditions with respect to the current real position of the UE. This has a disadvantage that at $t = 61.7\ s$ the delayed decision to execute a handover still causes the UE to move out of the LOS of its serving gNB 1 without an updated BPL for the gNB 5, to which it should now get connected. At $t = 152.5\ s$, the delayed decision to handover lets the SINR to degrade stronger then in *scenario 4.a*. Additionally, the UE is still served by gNB 4 up to this point, whereas in *scenario 4.a*, the UE is already served by a closer gNB 7. Finally, at around $t = 230\ s$ of the simulation time, the delayed decision to execute

a handover to the best cell causes a stronger SINR degradation compared to *scenario 4.a* due to the maintained connection to the gNB 7, which might not be in LOS for the UE at its current locaiton. *Scenario 4.c* shows identical results to *scenario 4.b*.

In conclusion for *scenarios 4.a, 4.b* and *4.c*, querying the *measurement REM* results in a tripled amount of unsuccessful REM queries, leading to failures of the LABM algorithm to provide an optimal up-to-date BPL for the reported UE location. A higher amount of handovers that are executed during the simulation run time is observed in *scenario 4.a* compared to *scenario 0, 2* and *3*. The most significant difference is in the regions where the UE moves from LOS to NLOS area of the current serving gNB. As expected, the delayed decision for the handover execution with help of LABM handover hysterisis thresholds helps to reduce the amount of re-connections between gNBs, saving the associated control signal overhead. *Scenario 4.a* performed 14 handover events, while *scenario 4.b, 4.c* performed 5 handovers event each. Due to missing REM entries on the queried locations, 97 REM queries failed in each of three scenarios. Moreover, similarly to *scenario 3.b* and *3.c*, the SINR generally degrades in such configuration, causing lower IP throughput.

5.2.3 Effect of Combined Reported Erroneous Locations for REM Querying and Measurement REM

Scenario 5.a investigates the combined effect of reported erroneous UE locations in REM querying and the *measurement REM*. Recovery algorithm is disabled and the LABM immediate handovers are enabled. In such configuration, not only the reported UE locations are affected by errors, causing REM queries for a location different from the real UE location, but also the returned REM entry is itself affected by location errors during REM construction. As a result, the returned REM entry might either correspond to a location that is further away from the real UE location, or the UE location error and *measurement REM* may compensate each other, delivering a better performance then *scenarios 3.a* and *4.a* in some cases. Figure 5.16 shows the SINR and serving gNB IDs for the baseline *scenario 2* and *scenario 5.a*. In general, it can be observed that the SINR is less stable in comparison to all previous scenarios, as expected. In contrast to *scenario 3.a* with the same error applied to the first UE location report, the LABM is able to query the *measurement REM* on the reported erroneous UE location, delivering a target gNB and a BPL. As a result, the IA procedure with the exhaustive beam sweep is skipped and the UE is able to connect to gNB 2 within first milliseconds of the simulation time. The REM query in this location succeeds due to the fact that the previously empty REM entry from the *ideal REM* is now containing a valid REM entry, as it is saved for a wrong erroneous location during the creation of the *measurement REM*. This case is an example of how the reported erroneous UE locations in REM querying and the *measurement REM* may compensate each other's error contribution. The subsequent behavior of SINR values demonstrates that both sources of error contribute to a more degraded signal quality in the area, where the UE is moving out of the LOS of its current serving gNB. As can be seen in Figure 5.17 showing the beam ID offsets for *scenario 5.a*, selected BPLs in the first seconds of simulation cause beam offsets of 4 to 5 azimuth sectors for gNB and 1 to 7 azimuth sectors for the UE, leading to strong fluctuations of the SINR and degradation below the RLF threshold. The starting location of the UE's walk path was challenging for all previous configurations of the LABM algorithm, but *scenario 5.a* has the worst performance so far. At $t = 58.25\ s$ the combined error contributions cause the LABM to select a BPL for the gNB 5 and execute

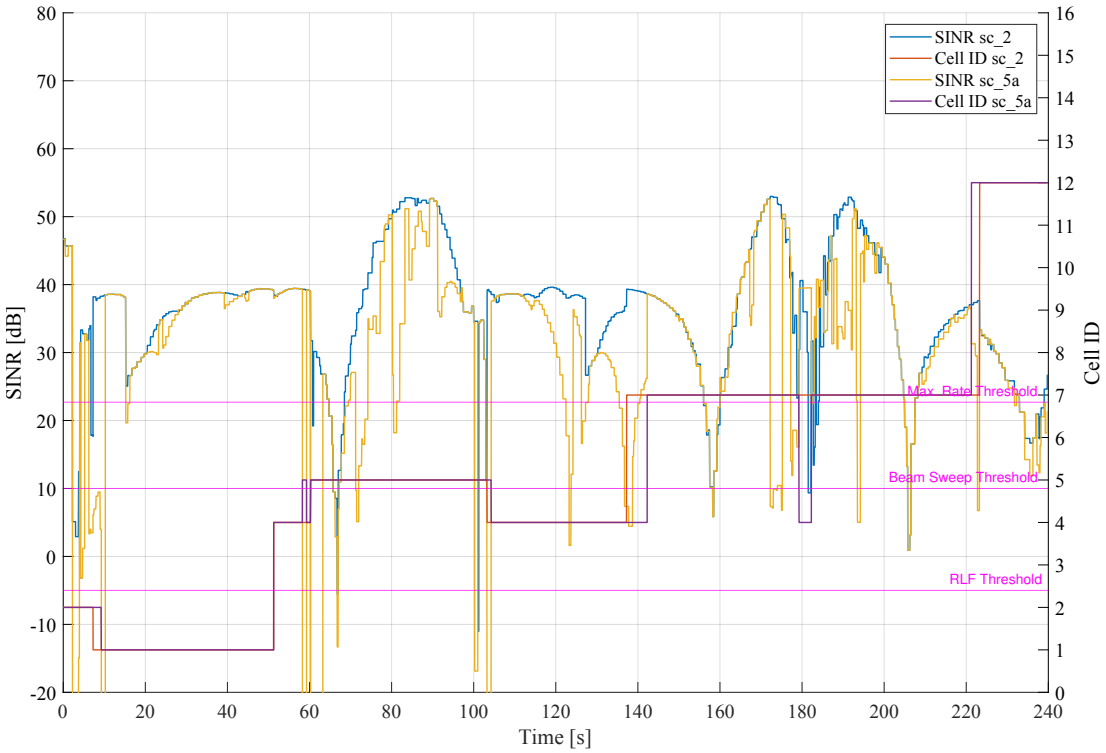

Figure 5.16: SINR in dB and serving gNB IDs for the UE in *scenario 2, 5.a*. Blue and red lines represent SINR and gNB ID for *scenario 2*, respectively. Yellow and purple lines represent SINR and gNB ID for *scenario 5.a*, respectively.

a handover from the currently serving gNB 4. As a result, the UE is commanded to be served by the gNB that is not in its LOS yet, leading to a severe signal degradation from $39.3\ dB$ to $-111.8\ dB$. The UE is served qith this BPL until the next location report arrives to the LTE coordinator and the LABM algorithm commands a handover back to the gNB 4 that is in LOS conditions, improving SINR above the maximum rate threshold of $22.7\ dB$. However, the same situation repeats at $t = 60.25\ s$, causing another RLF event. At $t = 61.25\ s$ and $t = 62.25\ s$ the combined error contributions lead to a REM query failure, leaving the UE to be served with a sub-optimal BPL until the next UE location report at $t = 63.25\ s$ improves the signal quality by selecting a BPL that has no beam ID offset with respect to the optimal BPL as can be seen on Figure 5.17. Now the UE is in proximity to its serving gNB 5. This is the area where even slight beam misalignment may cause severe signal degradation. This effect is present in *scenario 5.a* and magnified by the combined contribution of erroneous reported UE locations in REM querying and the *measurement REM*. Moreover, the Figure 5.17 shows an increased beam ID azimuth sector offset for gNB between $t = 60\ s$ and $t = 100\ s$, leading to a stronger fluctuation of the SINR level in comparison to previous scenarios. Similarly to how the SINR is strongly fluctuating when the UE is moving into the LOS conditions of gNB 5, the same strong

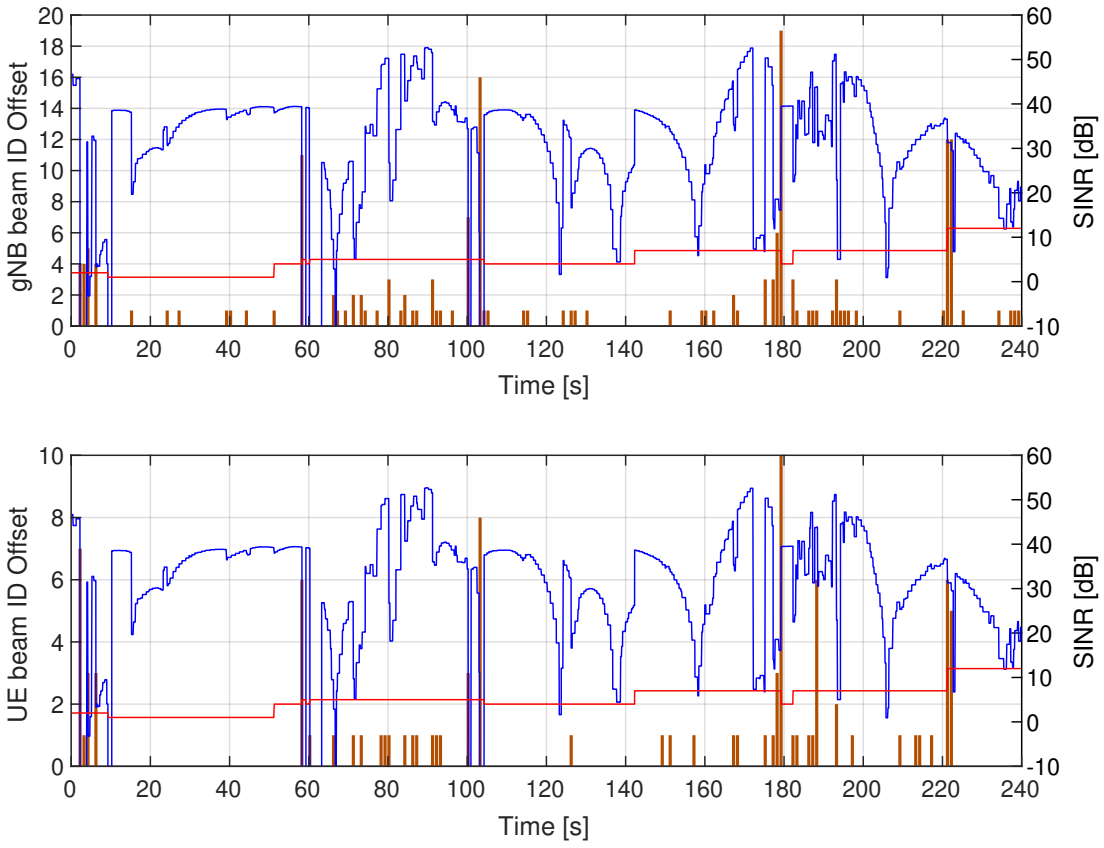

Figure 5.17: Beam offset of azimuth sectors for gNB (top) and UE (bottom) in dark orange, SINR in blue, current serving gNB in red for *scenario 5.a*.

fluctuations are also present when the UE moves out of the LOS of gNB 5. At around $t = 100\ s$ the UE location is moving around the building corner and enters the open area, optimally covered by gNB 4, but losing the LOS to serving gNB 5. Additional 2 RLF events happen in this area. Starting from $t = 116.25\ s$ until $t = 124.25\ s$ the LABM fails to query the *measurement REM*, as no valid REM entry can be provided for reported erroneous UE locations. As a result, the UE uses the BPL that gets more and more outdated with each step, causing the gradual decrease of the SINR level and falling below the beam sweep threshold of $10\ dB$. Same situation occurs between $t = 131.25\ s$ and $t = 139.25\ s$, leaving the UE with an outdated BPL for another 8 seconds. Later, in proximity of gNB 7 it can be observed on Figure 5.16 that the SINR fluctuation is the strongest when compared to *scenarios 3.a* and *4.a*. The combined error contribution even leads to a handover to gNB 4 for a brief moment of time at $t = 179.25\ s$.

Scenario 5.b and *5.c* disable immediate LABM handovers and set the LABM handover hysterisis thresholds to 1 and 2 location reports, respectively. From Figure 5.18 showing the SINR and serving gNB IDs for *scenario 5.a, 5.b, 5.c* it can be observed, that the behavior of the LABM algorithm does not change until around $t = 50\ s$ of the simulation

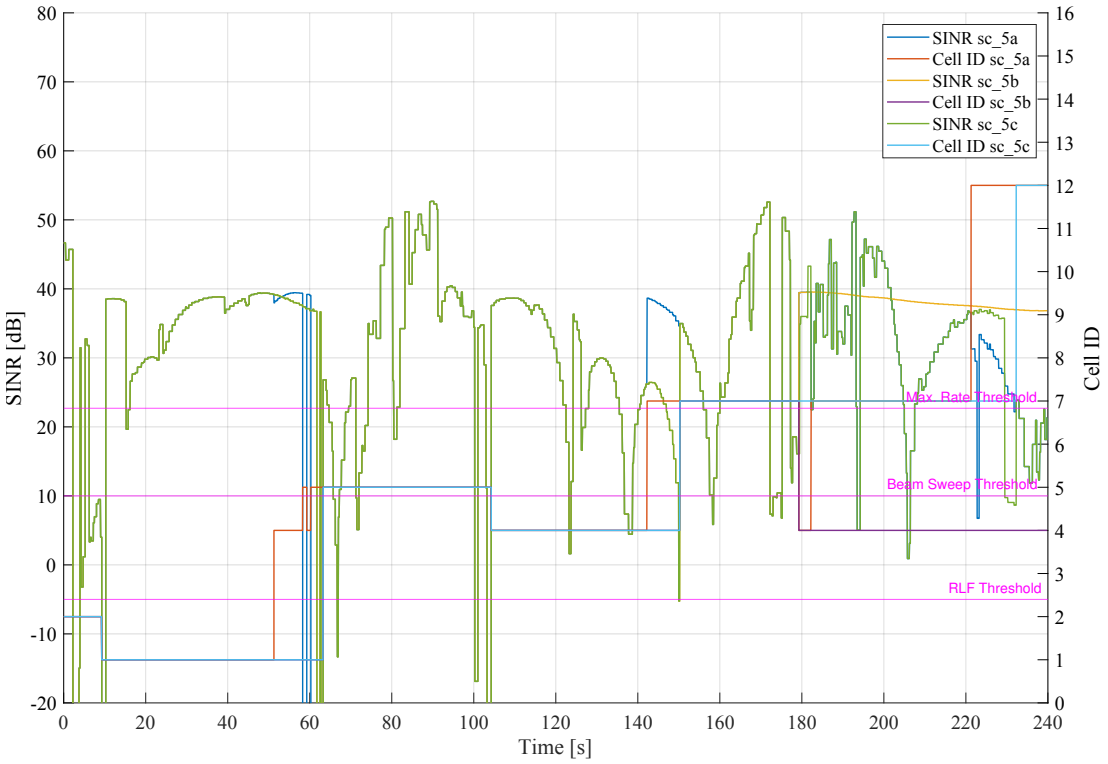

Figure 5.18: SINR in dB and serving gNB IDs for the UE in *scenario 5.a, 5.b, 5.c*. Blue and red lines represent SINR and gNB ID for *scenario 5.a*, respectively.Yellow and purple lines represent SINR and gNB ID for *scenario 5.b*, respectively. Green and cyan lines represent SINR and gNB ID for *scenario 5.c*, respectively.

time. At that point the hysterisis threshold keeps the UE connected to the gNB 1 in *scenario 5.b, 5.c*, preventing the ping-pong handover between gNB 4 and 5 and providing a stable SINR above the maximum rate threshold. However, the algorithm fails to execute a handover fast enough in *scenario 5.b, 5.c* when the UE moves out of the LOS of gNB 1 and needs to handover to the gNB 5, still causing RLF events at around $t = 62\ s$. The most significant difference in *scenario 5.b* with respect to the *scenario 5.a* is that the LABM algorithm decides to leave the UE being served by the gNB 4 starting from $t = 179.25\ s$. At $t = 189.25\ s$ *scenario 5.b* does not have necessity to handover to the best gNB reported by the *measurement REM*, as the SINR level is beyond the maximum rate threshold and remains in that region for the rest of simulation. The LABM algorithm in *scenario 5.b* does not schedule a handover and leaves the UE connected to gNB 4, similarly to how the default 5G-NR in *scenario 0* behaved. In contrast, *scenario 5.c* with hysterisis threshold being set at 2, keeps the UE connected to the gNB 7 at $t = 179.25\ s$, as the SINR level improves until the hysterisis threshold is exceeded. This is the reason why the behavior of *scenario 5.b* and *5.c* differs at this point of time. Similarly, towards the end of the simulation at $t = 221.25\ s$, *scenario 5.c* keeps the connection to the gNB 7 as the SINR is

above the maximum rate threshold. Only after the UE moves out of the LOS of gNB 7 and the signal quality degrades below the maximum rate threshold and remains at that level for 2 consecutive UE location reports, the LABM algorithm decides to execute a handover to gNB 12 at $t = 232.25\ s$ as it is considered optimal by the *measurement REM* at the reported erroneous UE location.

Overall, the combined effect of reported erroneous UE locations in REM querying and the *measurement REM* leads to a significantly increased amount of cases where REM queries fail. In the scenario *5.a* 118 REM queries failed out of 240 total location reports, meaning that in almost half of cases the LABM algorithm is not able to provide a BPL. This leads to situations where UE and gNB are using outdated BPLs for up to 8 seconds. In cases when UE moves laterally in relation to the serving gNB's beam, such period of time is long enough for the SINR level to decrease by up to $35\ dB$, which is shown in *scenario 5.a* around $t = 120\ s$. The amount of RLF events is 8 for *scenario 5.a*, and some of them are longer than in previous scenarios, as the LABM algorithm can not provide an alternative BPL due to failed REM queries.

5.3 Recovery Algorithm

Scenario 6 investigates the influence of the implemented LABM recovery algorithm that is described in the Section 3.2.2. *Scenario 6.a* repeats *scenario 3.a* with isolated contribution of the UE location error at *ideal REM* querying, but additionally enables the recovery algorithm. The LABM immediate handovers are enabled. From Figure 5.19 showing SINR and serving gNB IDs in *scenario 3.a, 6.a* it can be observed, that there is barely any difference in the SINR of between *scenario 3.a* and *scenario 6.a*. The exhaustive beam sweep at the simulation start still has to be performed in *scenario 6.a*, as the currently implemented LABM recovery procedure is not able to work without a serving gNB. The recovery algorithm is triggered only in cases where the UE location error in the *ideal REM* query to return an entry that is located inside a building. In *scenario 3.a* there are 36 location reports for which the *ideal REM* could not deliver a valid non-empty REM entry. In *scenario 6.a* all these 36 cases were successfully recovered and delivered a valid non-empty REM entry on the direction towards the serving gNB. As expected, in *scenario 6.a* the LABM algorithm is able to provide a BPL in response to each UE location report. Figure 5.20 visualizes the results of the recovery algorithm or erroneous reported UE locations. Green dots represent real UE locations, blue dots represent the reported erroneous UE locations that are reported to the LTE coordinator and that are used to perform the *REM* query. When the REM query fails, the recovery algorithm provides a recovered position, that is shown as red dots. The black arrows connect the related points, starting at the real UE location, pointing to the reported UE location and then from the reported to the recovered UE location. It can be seen that in most cases the recovered positions are quite close to the real UE locations. During the walk segments when the UE is connected to the gNB 1 or 4, such recovered positions results in BPLs that are very close to the ideal BPL that would have been provided for the error-free location report such as in *scenario 2*. Additionally, the usage of the *ideal REM* in *scenario 6.a* guarantees that recovery will always deliver a valid REM entry, unless the serving gNB towards which the recovery happens is located so that all traversed REM entries happen to be inside the building.

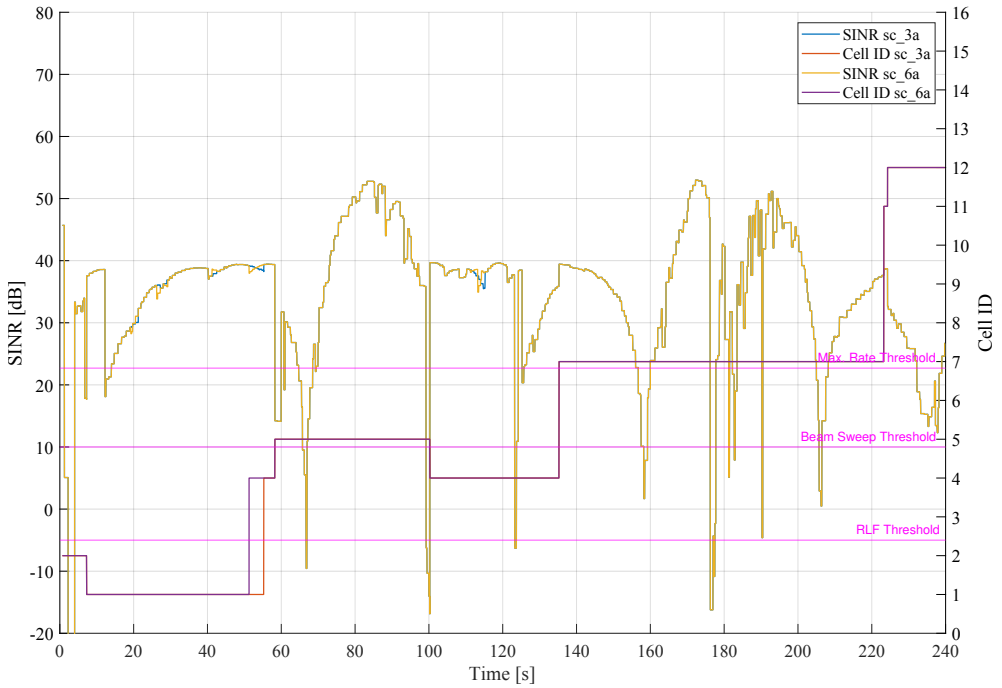

Figure 5.19: SINR in dB and serving gNB IDs for the UE in *scenario 3.a, 6.a*. Blue and red lines represent SINR and gNB ID for *scenario 3.a*, respectively. Yellow and purple lines represent SINR and gNB ID for *scenario 6.a*, respectively.

Scenario 6.b investigates the performance of the recovery algorithm for the case when the reported UE location is error-free, but the *measurement REM* is used instead of the *ideal REM*. From Figure 5.21 showing the SINR and serving gNB IDs for *scenario 4.a, 6.b* it can be observed that the LABM recovery algorithm has a more significant impact when it is applied on top of *scenario 4.a*, where the *measurement REM* is used and no UE location errors in REM querying are present. As described in the Section 5.2.2, the usage of the *measurement REM* leads to situations where the LABM algorithm is not able to deliver a BPL for up to 5 consecutive UE location reports in the simulated scenario, leading to the usage of the outdated BPL and strong SINR degradation. The recovery algorithm is expected to reduce the consequent REM failures by finding a non-empty REM entry. The confirmation to such expected behavior can be seen in Figure 5.21 around $t = 60\ s$ and around $t = 103\ s$, where the SINR level in *scenario 6.b* shows better performance than *scenario 4.a*. Around $t = 56\ s$ the duration of time spent under the RLF threshold is now significantly reduced due to the fact that querying the *measurement REM* at the recovered location happened to deliver REM entries that better reflect the channel propagation characteristics for the real UE location at that time point. By selecting different REM entries than in *scenario 4.a*, the SINR level in *scenario 6.b* increased beyond the maximum rate threshold, while in *scenario 4.a* the UE is still experiencing the RLF. Similar situation happens when the UE leaves the LOS of the serving gNB 5 at around $t = 101\ s$. As can be seen on the Figure 5.22 showing real, reported and recovered UE

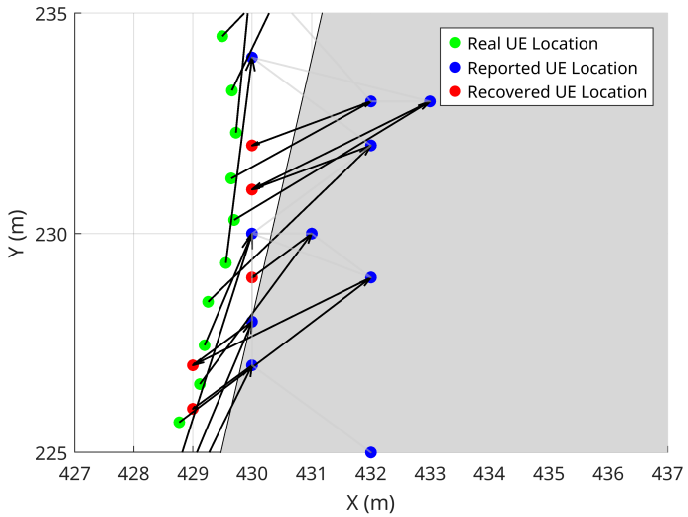

Figure 5.20: Real UE location (green), reported erroneous UE location (blue) and recovered UE locations (red) for *scenario 6.a*. The illustrated section of the walk path is served by the gNB 1.

locations in *scenario 6.b*, when the UE's location is within the area defined by x-coordinates 430 to 435 and y-coordinates between 280 and 290, there are 6 consecutive recovery events, which contributed to an update of the BPL according to the available REM entries in the *measurement REM*. The *measurement REM* caused ping-pong handovers between the gNB 4 and 5, but in general has allowed the SINR levels to raise above the maximum rate threshold for brief moments of time in *scenario 6.b*, whereas in *scenario 4.a*, the UE was experiencing a RLF.

Later, in proximity to the serving gNB 7 starting from $t = 178.25\ s$ the recovery algorithm had a negative effect on the performance of the LABM algorithm. It can also be seen on Figure 5.21, that the recovery algorithm has caused an additional RLF event at $t = 183.25\ s$. This is caused by the selection of a BPL that has a beam offset of 4 azimuth sectors for the gNB and 2 azimuth sectors for the UE. Such a high beam offset in the proximity to the serving gNB has a much stronger effect on the SINR, resulting in a strong signal degradation below the RLF threshold. In comparison to *scenario 4.a*, *scenario 6.b* shows an increased amount of performed handovers: 20 versus 14, but less RLF events: 4 versus 5, with less time spent under the RLF threshold. Moreover, *scenario 6.b* was able to recover in all 97 cases when the original REM query on the reported UE location fails due to a missing entry in the *measurement REM*.

Scenario 6.c incorporates the recovery algorithm on top of *scenario 5.a*, where both the reported erroneous UE locations for REM querying and the *measurement REM* are present. Figure 5.23 shows the SINR and serving gNB for *scenario 5.a, 6.c*, from which it can be observed, that the LABM recovery algorithm has a mixed influence on the behavior of signal quality. Higher SINR values are achieved in the area served by the gNB 5 between $t = 70\ s$ and $t = 100\ s$, and the earlier handover at around $t = 136.25\ s$ prevents the signal quality

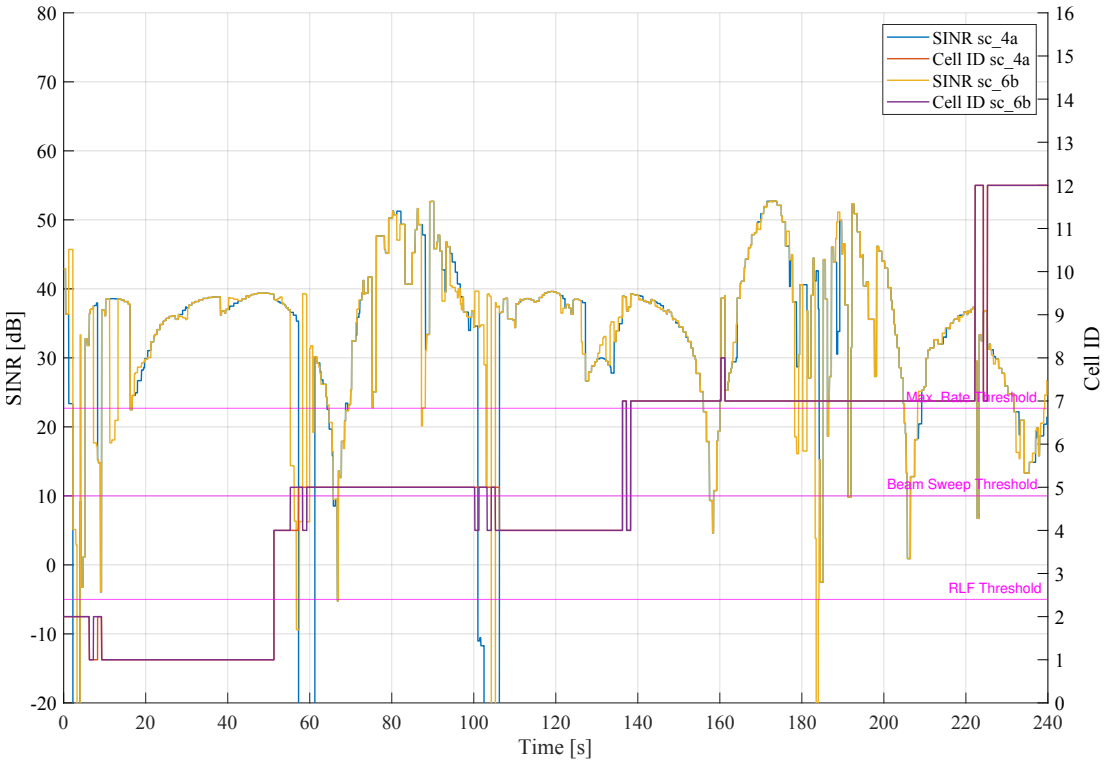

Figure 5.21: SINR in dB and serving gNB IDs for the UE in *scenario 4.a, 6.b*. Blue and red lines represent SINR and gNB ID for *scenario 4.a*, respectively. Yellow and purple lines represent SINR and gNB ID for *scenario 6.b*, respectively.

degradation below the maximum rate threshold. However, it can be seen that at around $t = 60\ s$ *scenario 6.c* shows similar behavior to *scenario 5.a*, where the algorithm fails to avoid RLF events when the reported location is in the LOS area of gNB 5, while the real UE location is still is in the NLOS of gNB 5. In the proximity of gNB 7 around$t = 170\ s$ higher beam ID offsets from the recovery to REM entries on erroneous locations lead to a stronger signal degradation and an additional RLF event. This effect is amplified by the fact that recovered locations lie even closer to the serving gNB, further amplifying the negative impact of even small beam ID offsets. The total amount of performed handovers remains at 20, same as in *scenario 6.b*, but it doubles with respect to *scenario 5.a*. *Scenario 6.c* experienced 8 RLF events. This aligns with the amount of RLF events in the scenario *scenario 5.a*, however, in *scenario 6.c* they occur at different time points, degrading the SINR in places, where in *scenaro 5.a* it was good enough to maintain the communication link.

In conclusion for tests in *scenario 6*, it can be said that the recovery algorithm had almost no effect for the case when querying the *ideal REM* on reported erroneous UE locations. The reason for that is that with the configured error model for the UE location

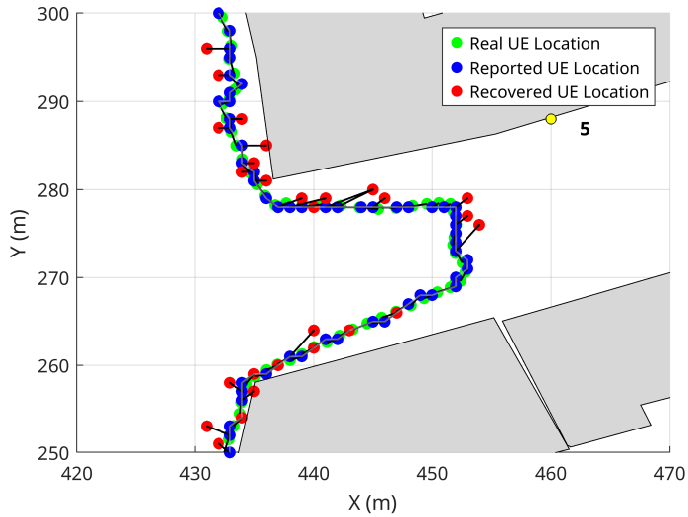

Figure 5.22: Real UE location (green), reported erroneous UE location (blue) and recovered UE locations (red) for *scenario 6.b*. Yellow dot represents the gNB location.

reports, the reported UE locations do not get moved into buildings for long enough periods in the selected walk path to make the currently used BPL outdated-enough to cause a severe beam misalignment. By contrast, as shown by *scenario 6.b*, the recovery algorithm is more efficient in counteracting the choice of sub-optimal BPLs if the only source of errors is the *measurement REM*. As shown by *scenario 6.b*, the SINR level was below to RLF threshold for shorter periods if compared to *scenario 4.a*. In the case when both UE location error in REM querying is present and the *measurement REM* is used, the recovery algorithm shows an improvement in the maximum achievable SINR level, but increases the total amount of performed handovers, increasing the associated signaling overhead. Additionally, the recovery algorithm helps to deliver a fresher BPL, avoiding strong signal level degradation as can be seen between $t = 130\ s$ and $t = 150\ s$ in the Figure 5.23. Furthermore, the recovery algorithm is able to provide a BPL in all 118 cases where the LABM delivers empty REM entry in *scenario 5.a*. However, as soon as the UE moves closer to the serving gNB, the recovery algorithm delivers locations that are closer to the serving gNB. This leads to the selection of sub-optimal REM entries, delivering BPLs that cause a beam ID offset, that are significant enough to lead to RLF.

5.4 Handover Thresholds

In this section the consequences of disabling the LABM immediate thresholds are investigated. *Scenario 7.1* extends *scenario 6.c*, where the UE location error in REM querying is present and the *measurement REM* is used. The LABM recovery algorithm is also enabled, while the LABM handover hysterisis threshold is set to 1. The effect of such configuration on the network performance in terms of SINR level is shown in Figure 5.24, where *scenario 6.c* is compared to *scenario 7.a*. A similar behavior to *scenario 5.b* in Figure 5.18 can be noticed. At $t = 51.25\ s$ the hysterisis threshold prevents a handover from gNB 1 to

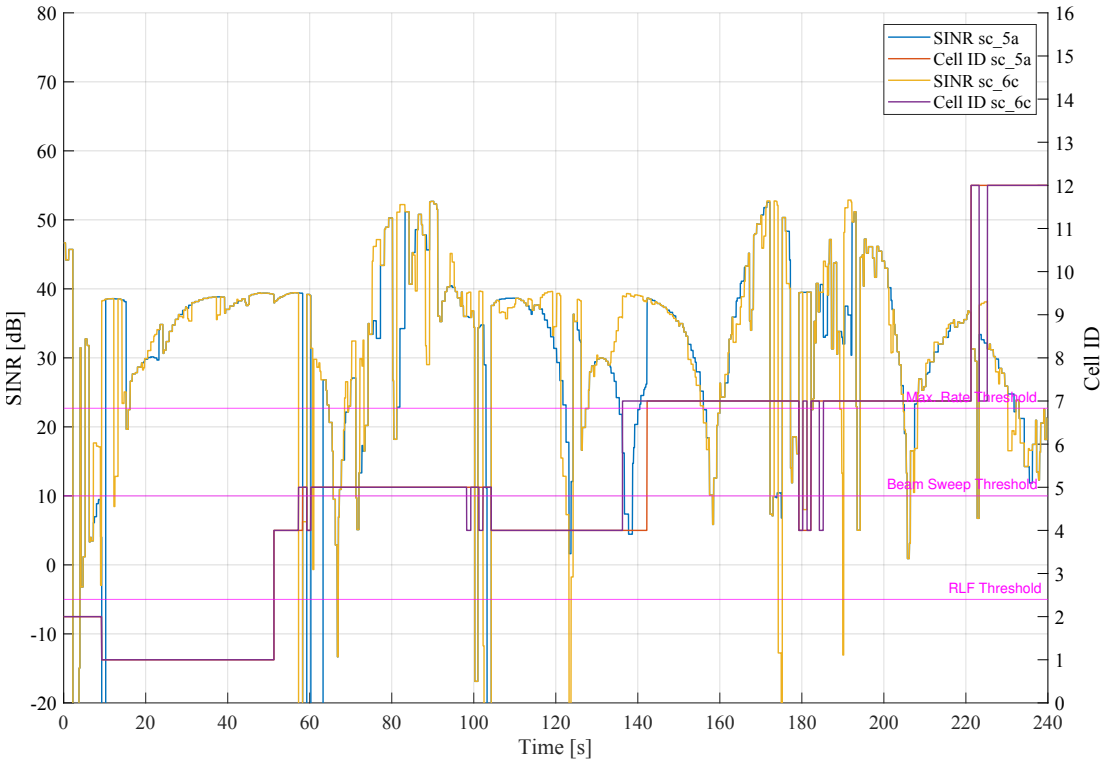

Figure 5.23: SINR in dB and serving gNB IDs for the UE in *scenario 5.a, 6.c*. Blue and red lines represent SINR and gNB ID for *scenario 5.a*, respectively. Yellow and purple lines represent SINR and gNB ID for *scenario 6.c*, respectively.

gNB 4, as the SINR level is above the maximum rate threshold. This leads to a difference in behavior between *scenario 6.c* and *7.a* starting from $t = 56.25\ s$. While *scenario 6.c* executes a handover to gNB 5 that was reported to be the optimal one and ends up in the RLF due to the lack of LOS to it, *scenario 7.a* continues using the gNB 1 until the LOS to it is interrupted. As a result, the RLF event still occurs, but at a later time point and the UE recovers from it with the next location report. Later, at $t = 136.25\ s$, the decision to remain at the current serving gNB 4 leads to a gradual degradation of the SINR. At $t = 152.25\ s$ the SINR level gets below the maximum rate threshold, triggering the handover hysterisis counter in the LABM algorithm, but the signal degrades too fast and the subsequent handover to the gNB 7 happens only when the SINR is below the beam sweep threshold of $10\ dB$. Another point that differs from *scenario 6.c* is the behavior towards the end of simulation. Similarly to *scenario 5.b*, the UE connects to gNB 4 and it is served by it until the end of the simulation. Thus, 3 handover events are avoided and the overall SINR level is kept above the maximum rate threshold. *Scenario 7.a* performs only 5 handovers during the simulation runtime, which is significantly lower than 20 handovers executed in *scenario 6.c*. The amount of RLF events has also reduced by 1 with respect to *scenario 6.c*. Apart from the stronger SINR degradation around $t = 153\ s$, *scenario*

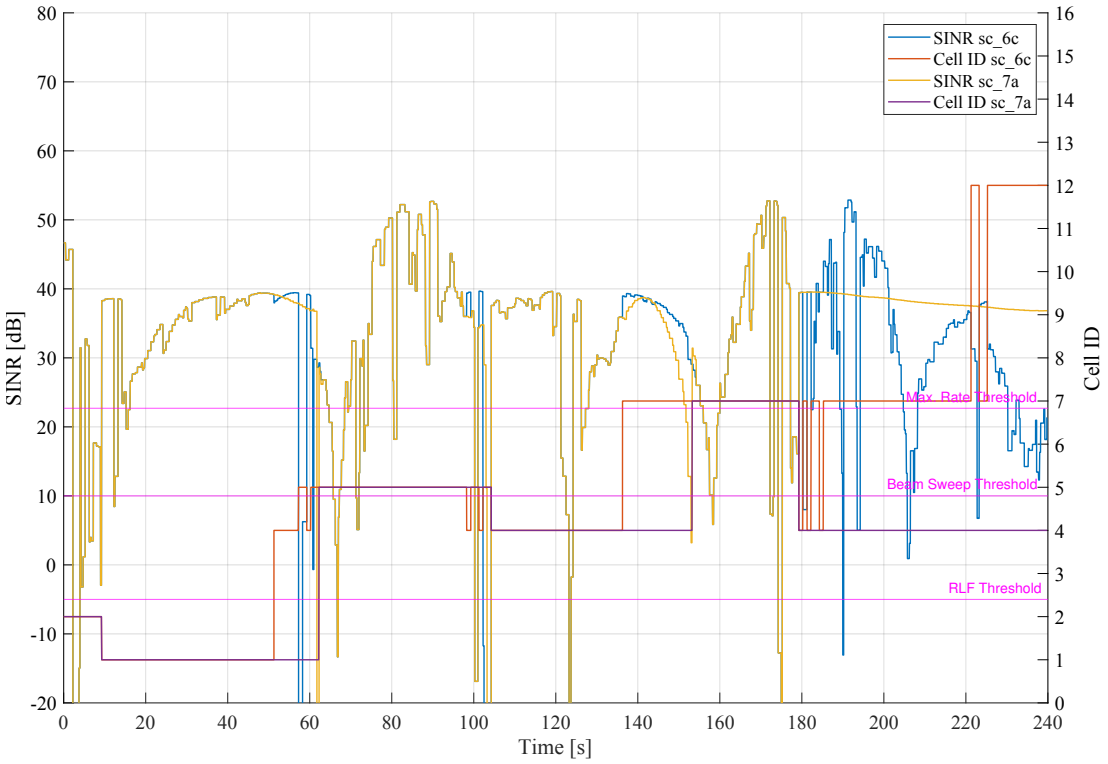

Figure 5.24: SINR in dB and serving gNB IDs for the UE in *scenario 6.c, 7.a*. Blue and red lines represent SINR and gNB ID for *scenario 6.c*, respectively. Yellow and purple lines represent SINR and gNB ID for *scenario 7.a*, respectively.

7.a shows better performance in terms of handover signaling overhead and signal stability, especially in the last segment of the walk path.

Scenario 7.b shows almost identical behavior of the SINR to *scenario 7.a*, while *scenario 7.c* shows similar behavior to *scenario 7.a* until $t = 150\ s$, and then the behavior similar to *scenario 6.a*. For this reason the corresponding SINR plots are omitted. The similarity in behavior between *scenario 7.b* and *7.a* is explained by the fact that LABM handover hysterisis thresholds are relevant only for the cases when the SINR is in the region between the maximum rate threshold of $22.7\ dB$ and the beam sweep threshold of $10\ dB$. Once the signal quality drops below SINR $= 10\ dB$, the LABM algorithm executes a handover to the most optimal cell according to the REM entry. Such behavior attempts to minimize the possibility to end up below the RLF threshold, as once the signal quality reaches $10\ dB$, there is a high risk of a further sudden drop. In the simulated scenario the SINR level usually does not remain between the maximum rate threshold of $22.7\ dB$ and the beam sweep threshold for longer periods.As the recovery algorithm succeeds in 100% of all 118 cases when it is triggered, the LABM always provides a BPL to the UE and gNB, either improving or significantly degrading the link quality. In the case of *scenario 7.c*, the UE does not perform the handover to gNB 4, as the increased hysterisis threshold of 3 location

reports causes the UE's SINR to be stuck between the maximum rate threshold of $22.7\ dB$ and the beam sweep threshold of $10\ dB$ for long enough for the SINR to increase above the maximum rate threshold, resetting the hysterisis counter and remaining served by the gNB 7.

As a conclusion for the usage of LABM handover hysterisis threshold in configurations with UE location error in REM querying, the *measurement REM* and the recovery algorithm, the overall performance in comparison to immediate LABM handovers can be generally considered as improved. As was demonstrated, the delayed decisions to handover helps to eliminate ping-pong handovers between gNBs, which is a particular issue when both UE location error in the REM querying and the *measurement REM* are simulated. It should be noted that the performance of the LABM algorithm with hysterisis thresholds strongly depends on the selected walk path and simulation area. In context of this thesis, a small hysterisis threshold has shown an improvement of signal stability, especially due to the behavior towards the end of the simulation, where the UE was served by a different gNB, than in almost all other simulation scenarios.

5.5 Location-Aided Beam Management in a High Urbanization Area

In *scenario 8* the influence of a stronger UE location error in REM querying is investigated. To simulate such scenario, the parameters for the Ornstein-Uhlenbeck stochastic process are set according to the Table 4.2 for the high urbanization scenario. The red line in Figure 4.3 shows the resulting erroneous UE walk path that is reported to the LTE coordinator. As can be seen on Figure 4.3, the significant portion of the walk path is now shifted inside of buildings. In scenarios without the recovery algorithm, this is expected to lead to prolonged sequences of failures to query the REM for the reported UE location, resulting in an outdated BPL being used for way too long. The usage of the *measurement REM* may improve the situation even without the recovery algorithm, as some REM entries may have been stored for locations inside of buildings and may overlap with reported erroneous UE locations.

Scenario 8.d introduces the high urbanization error applied to the UE location reported for REM querying, while using the *measurement REM* without recovery algorithm and with immediate LABM handovers. Such configuration is compared to *scenario 5.a*, which uses same LABM algorithm configuration with medium urbanization error. As can be observed in Figure 5.26 that compares the SINR and serving gNB for *scenario 5.a, 8.d*, the high urbanization error applied for UE location reports has lead to the failure to query the *measurement REM* at the start of the simulation, leading to an exhaustive beam sweep. Due to lack of recovery algorithm and a high error in UE location reports, the LABM fails to deliver a BPL for the next 6 reported locations, leading to the RLF event at $t = 2.25\ s$ and stronger SINR degradation in comparison to *scenario 5.a*. The LABM manages to deliver an optimal BPL for the real UE location only starting from $t = 12.5\ s$.. However, according to Figure 4.3 that shows the UE walk path with high urbanization error, at around $t = 30\ s$ the reported UE location is moved inside of building for a prolonged period of time. The effect of this can be observed on Figure 5.26 as a gradual degradation of the SINR that leads to a drop below the beam sweep threshold at $t = 45.75\ s$. When the REM query succeeds for the reported erroneous UE location at $t = 48.25\ s$, the SINR level is significantly improved and is comparable to the SINR in *scenario 5.a*. However,

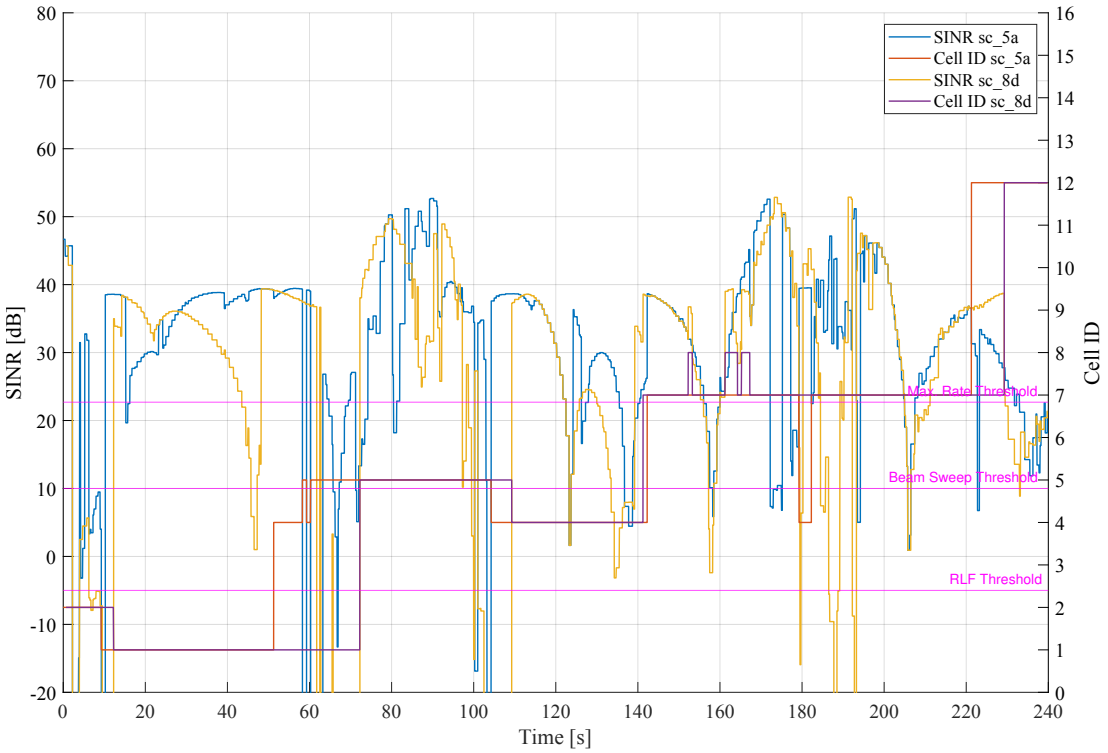

Figure 5.25: SINR in dB and serving gNB IDs for the UE in *scenario 5.a, 8.d*. Blue and red lines represent SINR and gNB ID for *scenario 5.a*, respectively. Yellow and purple lines represent SINR and gNB ID for *scenario 8.d*, respectively.

starting from $t = 61.7\ s$ the LABM can not deliver an up-to-date BPL and the UE remains served by gNB 1, to which the LOS is already lost at this time point. The lack of BPL updates leads to almost 10 seconds spent below the RLF threshold. Similar situation occurs starting from $t = 101\ s$. In contrast, in *scenario 5.a* the LABM manages to keep the SINR at higher levels, even briefly surpassing the maximum rate threshold several times. Greater magnitude of latitude error component in the reported erroneous UE location lead to ping-pong handovers between gNB 7 and 8 between $t = 152\ s$ and $t = 168\ s$, whereas in *scenario 5.a* the LABM algorithm managed to keep the UE connected to gNB 7. Due to proximity to serving gNB 7 and greater error magnitude in reported erroneous UE locations in *scenario 8.d*, the SINR level has much stronger fluctuations between $t = 178\ s$ and $t = 194\ s$ than in *scenario 5.a*, leading to 3 additional RLF events in comparison to *scenario 5.a*. Overall, the high urbanization error applied to the UE location reported for *measurement REM* querying leads to significant degradation of performance in terms of SINR levels. *Scenario 8.d* has experienced 3 additional RLF events in comparison to *scenario 5.a*. Moreover, the time spent below the RLF threshold is significantly longer when compared to *scenario 5.a*.

Scenario 8.a introduces the high urbanization error applied to the UE location reported for REM querying, while using the *measurement REM* with recovery algorithm and im-

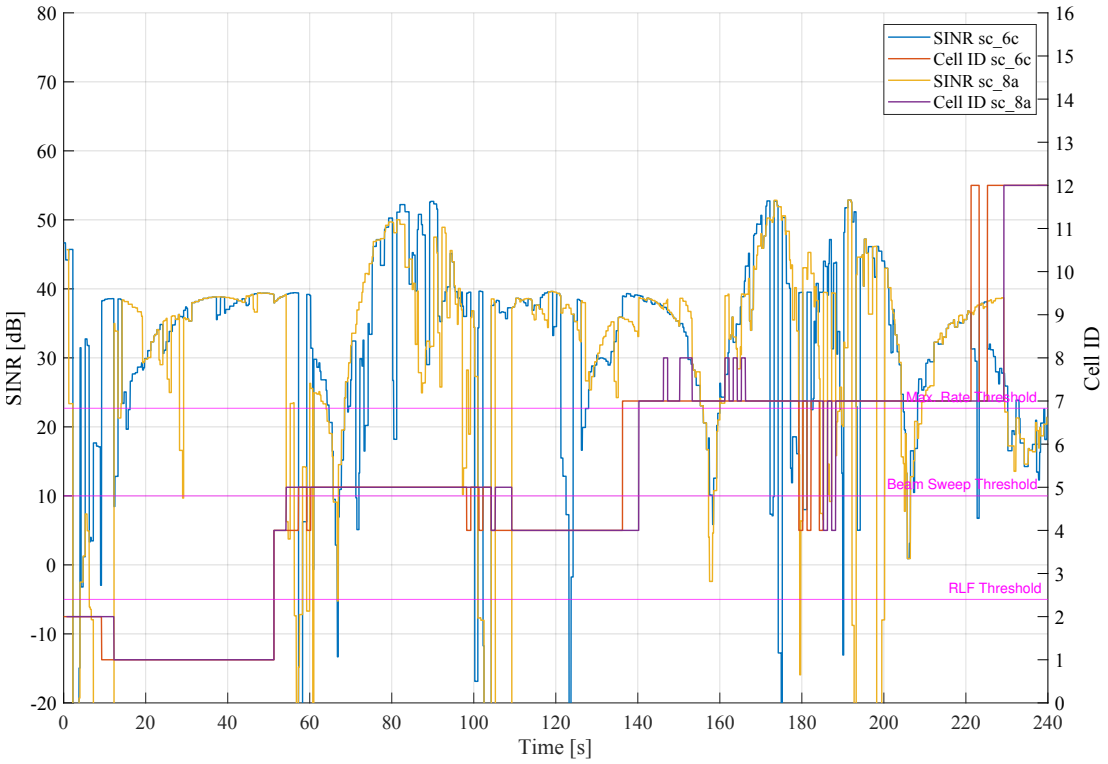

Figure 5.26: SINR in dB and serving gNB IDs for the UE in *scenario 6.c, 8.a*. Blue and red lines represent SINR and gNB ID for *scenario 6.c*, respectively. Yellow and purple lines represent SINR and gNB ID for *scenario 8.a*, respectively.

mediate LABM handovers. Such configuration is compared to *scenario 6.c*, which uses same LABM algorithm configuration with medium urbanization error. As can be observed in Figure 5.26 that compares the SINR and serving gNB for *scenario 6.c, 8.a*, the high urbanization error applied for UE location reports has lead to the failure to query the *measurement REM* at the start of the simulation, leading to an exhaustive beam sweep. Reported UE locations are significantly moved south-east with respect to real UE locations. Due to challenging channel propagation characteristics in the area near the gNB 2, the significant UE location error results in a very poor SINR level, leading to prolonged periods of time spent below the RLF threshold. Additionally, it can be observed that between $t = 140\ s$ and $t = 190\ s$ multiple ping-pong handovers take place, increasing the associated signaling overhead in comparison to *scenario 6.c*. *Scenario 8.a* executes a total of 22 handover events, which is the highest amount from all previously performed simulations.

In *scenario 8.a* 149 REM queries have initially failed and the recovery algorithm managed to deliver an alternative REM entry in 148 cases. The single instance of recovery algorithm failure occured at $t = 108.25\ s$ for the reported erroneous UE location at $x = 440, y = 291$. In that case the reported UE location was too far into the building and the serving gNB was still the gNB 5, which was located behind the building's corner in NLOS with respect

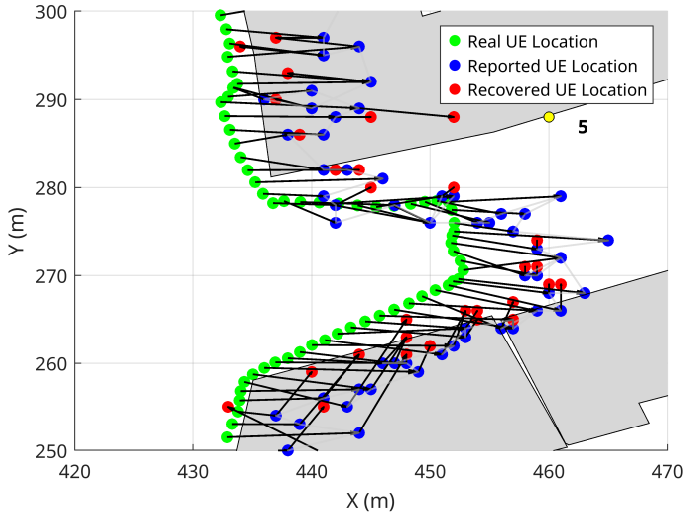

Figure 5.27: Real UE location (green), reported erroneous UE location (blue) and recovered UE locations (red) for *scenario 8.a*. Yellow dot represents the gNB location.

to the real UE location $x = 433, y = 291$. As a result, all of checked REM entries on the virtual line between the reported UE location and the serving gNB 5 were overlapping with buildings and none of entries from the *measurement REM* happened to be on this line.

Figure 5.27 shows the real, reported and recovered UE locations in *scenario 8.a* and demonstrates that in most cases, UE locations used for the REM querying are moved by 4 to 7 meters with relation to the real UE location. Often, recovered UE locations are moved into NLOS areas of the serving gNB. As a result, the time spent below the RLF threshold in the area around the gNB 5 is increased in comparison to *scenario 6.c*.
However, the periods of time spent below RLF threshold are still shorter than in *scenario 8.d*.

Figure 5.28 compares the SINR and serving gNB IDs between *scenario 8.a, 8.d* and it can be observed, that the significant performance degradation in the areas where the UE transitions between LOS and NLOS areas of the serving gNB such as at around $t = 62\ s$ and $t = 103\ s$ in *scenario 8.d*. The lack of recovery and updated BPL leads to an almost 10 second-long period under the RLF threshold at $t = 62\ s$, and 7 second-long period below the RLF threshold at $t = 102\ s$. It can also be observed tat generally the selected BPLs are not updated for long periods of time due to failed REM queries. In total, 149 REM queries fail in *scenario 8.d*, meaning that the LABM algorithm can not deliver a BPL in response to more than half of reported UE locations. This results in multiple instances of gradual SINR level degradation below the beam sweep threshold of $10\ dB$, which do not happen in *scenario 6.c*. The total amount of RLF events in *scenario 8.d* is 11, which is the highest amount from all previous simulations. The time spent below the RLF threshold is also the longest from all performed tests, which indicates the worst network performance so far. On the other side, the total amount of executed handovers is 11: half of what *scenario 8.a* performed.

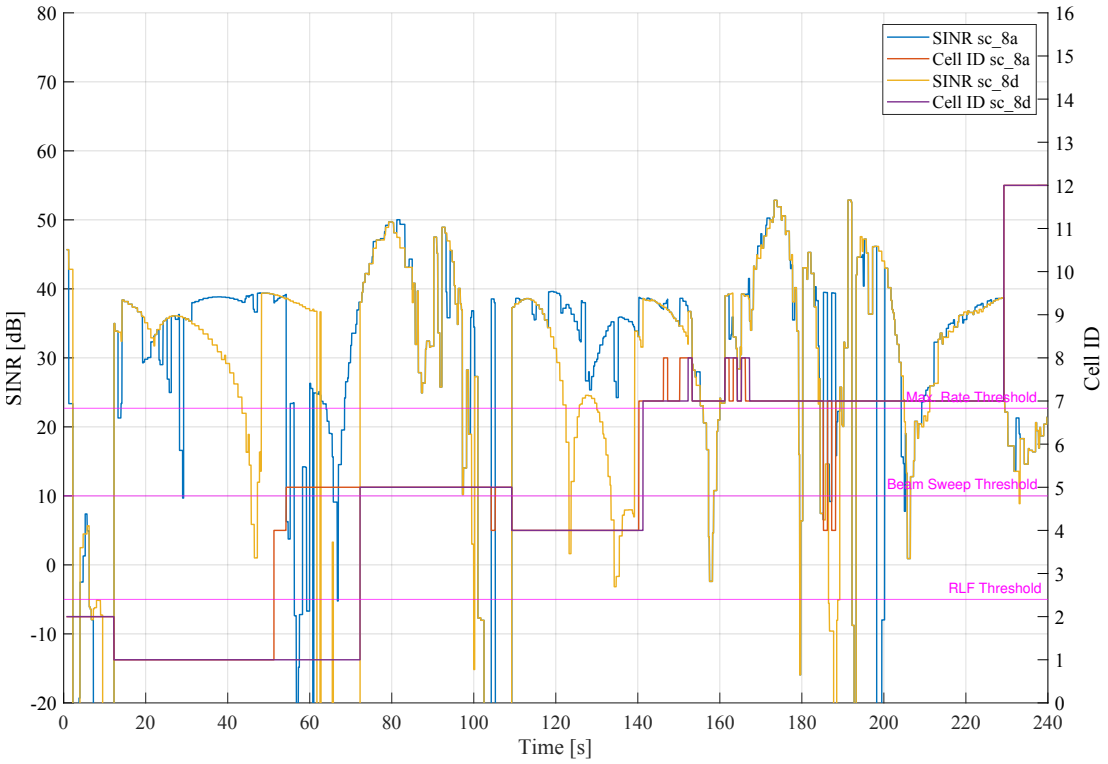

Figure 5.28: SINR in dB and serving gNB IDs for the UE in *scenario 8.a, 8.d*. Blue and red lines represent SINR and gNB ID for *scenario 8.a*, respectively. Yellow and purple lines represent SINR and gNB ID for *scenario 8.d*, respectively.

Scenario 8.b and *8.c* disable the LABM immediate thresholds and introduce the LABM hysterisis threshold of 1 and 2 location reports, respectively. From Figure 5.29 comparing the SINR and serving gNBs in *scenario 8.a, 8.b, 8.c* it can be seen, that the amount of performed handovers reduces from 22 in *scenario 8.a* to 6 in both *scenario 8.b* and *8.c*. Interestingly, in case of the high urbanization error applied for the UE location report for *measurement REM* querying, the usage of hysterisis thresholds contributes to a more stable SINR levels, avoiding strong fluctuations of the received signal quality around $t = 55\ s$, where the UE was moving out of the LOS of the gNB 1 towards the LOS area of the gNB 5. Delayed handover decisions have already shown improvements for the signal quality in *scenario 4.b, 4.c, 5.b* and *5.c*. Additionally, it can also be observed that due to the exact pattern of SINR fluctuation at around $t = 185\ s$, the usage of hysterisis thresholds causes the UE have a stable connection to gNB 4 in the last part of the walk path. This leads to SINR values above the maximum rate threshold, contributing to a more stable communication link, similarly to *scenario 5.b*.

As a conclusion for *scenario 8*, the high urbanization level significantly degrades the performance of the network if no recovery algorithm is used, leading to frequent and

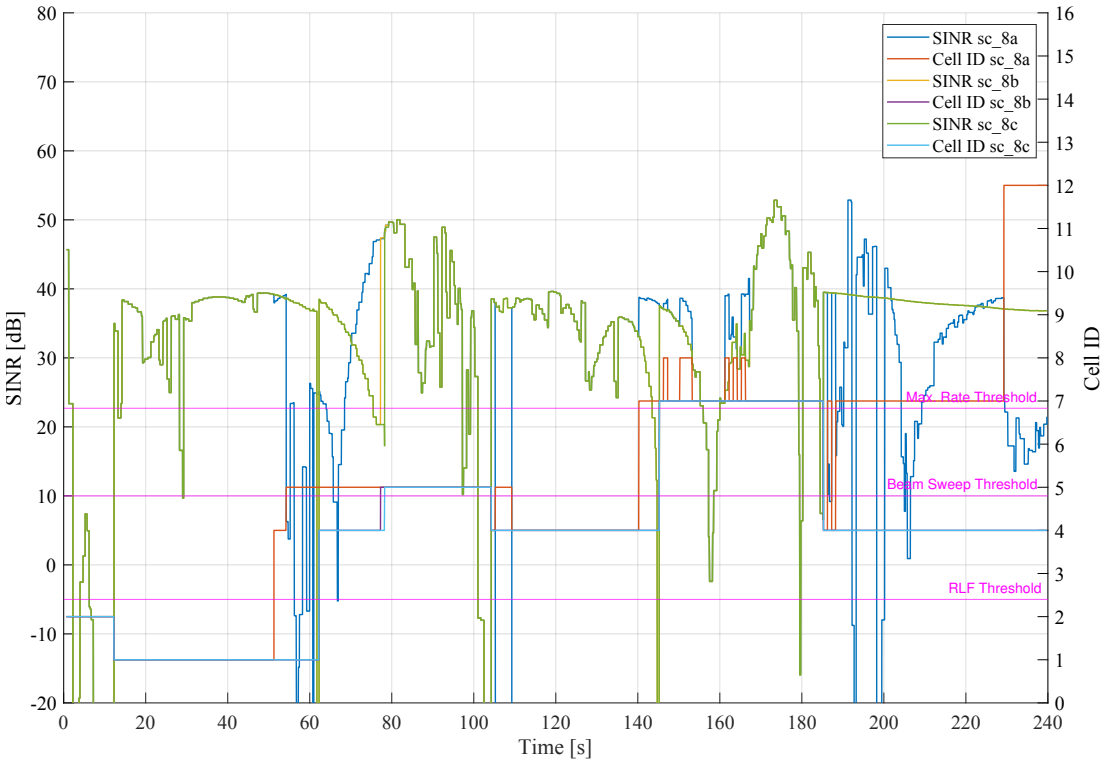

Figure 5.29: SINR in dB and serving gNB IDs for the UE in *scenario 8.a, 8.b, 8.c*. Blue and red lines represent SINR and gNB ID for *scenario 8.a*, respectively. Yellow and purple lines represent SINR and gNB ID for *scenario 8.b*, respectively. Green and cyan lines represent SINR and gNB ID for *scenario 8.c*

prolonged outages. When the recovery algorithm is used in *scenario 8.a*, the LABM algorithm is still able to operate in the most challenging setup so far. Additionally, if the immediate LABM handovers are disabled, this contributes to more stable SINR behavior with reduced amount of handover-related signaling overhead. As shown in the last simulation section in Figure 5.29, hysterisis threshold may also contribute to a better choice of the serving gNB. However, this most probably can not be generalized as an expected behavior with all possible UE walk paths and simulation areas.

5.6 High LTE RRC Delay

Lastly, the effect of an increased delay for the reporting of UE locations to the LTE coordinator is investigated. An artificial delay is introduced in the *DoSendPositionReport* method of the *nrUeRrcProtocolIdeal* class during the scheduling of the transmission of the *LteRrcSap::PositionReport* structure to the LTE coordinator's RRC layer. The introduced delay is derived from a normal distribution with its mean μ set to 250 ms, and the standard deviation σ to 300 ms. The lower bound for the delay is set to 250 ms. Thus, the

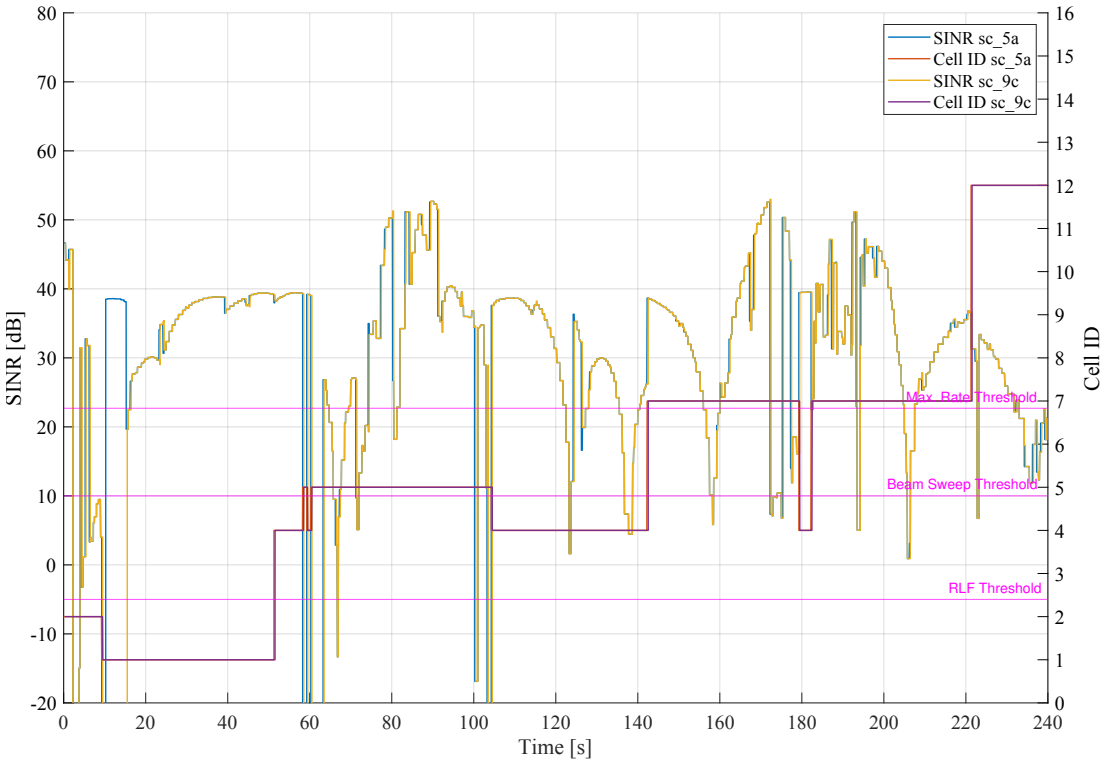

Figure 5.30: SINR in dB and serving gNB IDs for the UE in *scenario 5.a, 9.c*. Blue and red lines represent SINR and gNB ID for *scenario 5.a*, respectively. Yellow and purple lines represent SINR and gNB ID for *scenario 9.c*, respectively.

distribution causes the UE location report to be delayed by more than 500 ms in some cases. Considering the typical LTE delays between 20-60 ms, the configured delay represents a highly congested LTE network [62].

Scenario 9.a introduces this delay for the setup based on *scenario 3.a*, where only the UE location error in the *ideal REM* querying is present, with enabled immediate LABM handovers. The performance of the network is almost identical to the performance in *scenario 3.a* with only a couple of instances where the SINR is up to 3 dB lower for scenario *scenario 9.a*. With configured velocities of the UE of $1\ m/s$, the *ideal REM* and medium urbanization error for UE location reports, the configured delay is leading to a significant difference in the network performance. For *scenario 9.b*, where the only source of errors is the usage of the *measurement REM*, the high RRC delay makes a larger difference by causing a RLF event at around $t = 60\ s$. The combined effect of an executed handover from gNB 4 to gNB 5, the delayed UE location report and a failed REM query have resulted in the communication over a sub-optimal BPL, leading to an outage. *Scenario 9.c* is based on *scenario 5.a*, where the UE location error in the *measurement REM* querying with immediate LABM handovers is simulated. In the Figure 5.30 only significant difference to *scenario 5.a*, is the behavior of the LABM algorithm in the first 15 s of the simulation,

where the UE moves from the LOS area of the gNB 2 into the LOS area of the gNB 1. Due to a delayed location report and subsequent failures in REM querying, the UE remains with a sub-optimal BPL that causes a beam offset of 2 azimuth sectors, leading to a prolonged period spent under the RLF threshold. The remaining part of the simulation did not show any significant differences to *scenario 5.a*. Due to minimal differences in network performance in *scenario 9.a, 9.b* to *scenario 3.a* and *4.a*, respectively, their SINR plots are omitted.

The last *scenario 9.d* is based on *scenario 6.c*, where the UE location error in the *measurement REM* querying with immediate LABM handovers and an enabled recovery algorithm is simulated. The behavior of the network is almost identical to *scenario 6.c*. Due to the enabled recovery algorithm, the initially failed REM queries that prevented the UE BPL update in *scenario 9.c* are now recovered and the LABM algorithm is a able to provide an up-to-date BPL. The only significant difference is observed at $t = 57.5\ s$, where the delayed update of the BPL seems to avoid the degradation of the SINR below the RLF threshold. Also for *scenario 9.c* the SINR plot is omitted.

As a summary for *scenario 9*, the increased LTE RRC delay is not able to significantly affect the performance of the LABM algorithm with an exception of some mentioned edge-cases. The observations are in line with expectations, as the configured delay values are not delaying the UE location report for long enough to make the location information outdated enough. The situation might be different for the case when the UE velocity increases, as in this case the reported UE location will be further away from the real location, potentially resulting in a more severe beam misalignment.

5.7 Analysis Summary

In this section, a summary of the performance of selected simulation scenarios is provided. The default 5G-NR network configurations and the ideal configuration of the LABM with UE location reporting set to 1 Hz were selected as baselines. The remaining scenarios in this comparison are selected in such way that it is possible to do a side-by-side comparison of the network performance with most important combinations of the LABM algorithm's parameters.

To begin with, the distribution of SINR values is compared between the selected *scenarios 0, 2, 3.a, 4.a, 5.a, 6.c, 7.a, 7.c, 8.a, 8.b, 9.d* in form of box plots in Figure 5.31. As expected, *scenario 0.b* has its Inter Quartile Range (IQR) concentrated over a very small range of SINR values with a median of $38.6\ dB$. Its minimum and maximum whiskers are at $37.2\ dB$ and $40.7\ dB$, respectively. This scenario represents the configuration with the most up-to-date BPL information and most stable SINR values. *Scenario 0.a* has its SINR values spread over larger range while having a median of $34.1\ dB$ with minimum and maximum whiskers at $10.9\ dB$ and $45.7\ dB$, respectively. It can be observed, that among all LABM configurations, *scenario 2*, *7.a* and *8.b* have their IQR concentrated over a smaller range of SINR values that tends to be covering higher SINR values. The median of *scenario 2*, *7.a* and *8.b* is skewed towards a higher SINR value of $40\ dB$. Such distribution of data implies a better performance of *scenario 2* and *7.a* in comparison to other LABM configurations and also in comparison to *scenario 0.a*. In case of *scenario 2*, *7.a* and *8.b*, the maximum whisker is set to $50.9\ dB$, $48.6\ dB$ and $48.63\ dB$, respectively. Such values are higher

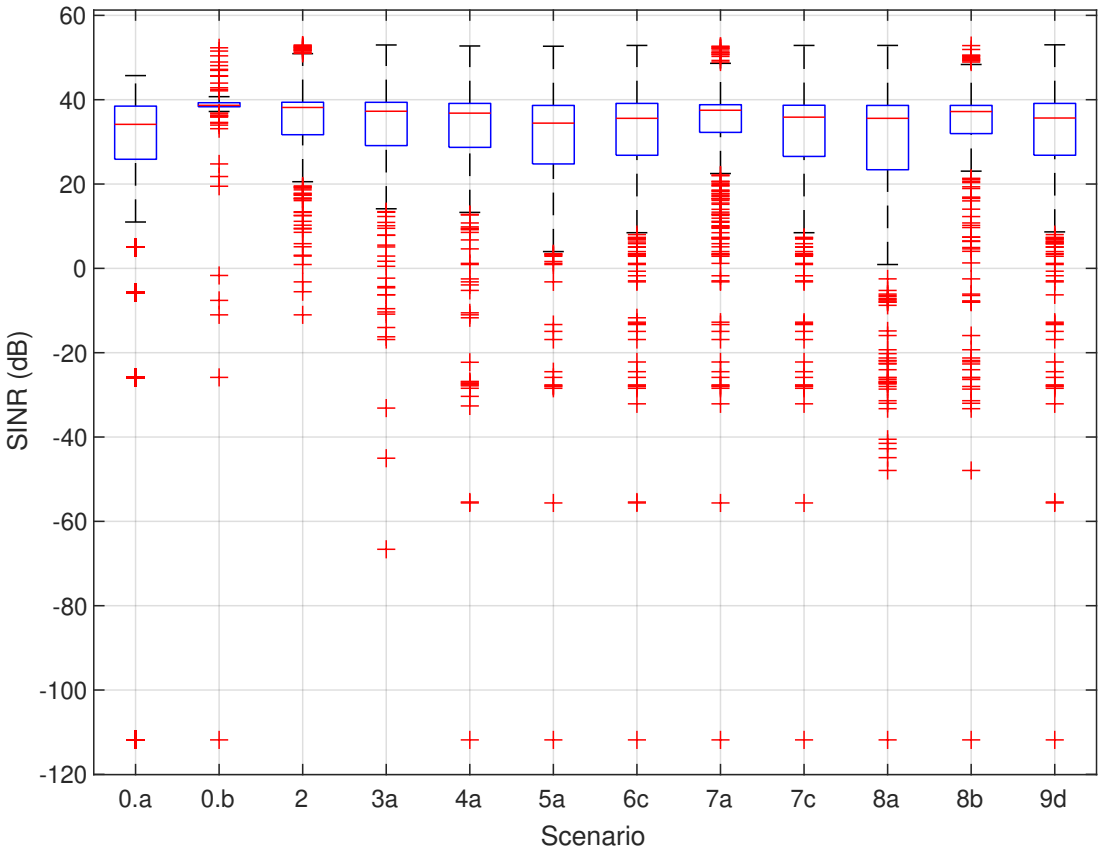

Figure 5.31: Box plots of the SINR distribution for the selection simulation scenarios.

than the maximum whisker of $45.7\ dB$ in the default 5G-NR configuration in *scenario 0.a* and *0.b*. This, as well as other LABM configurations in other selected scenarios, shows a greater amount of instances with higher values within the top 25% of the distribution of SINR values. Thus, it can be concluded that the LABM is able to achieve higher SINR values by selecting and trying to continuously maintain the optimal BPL for UE and gNB. Surprisingly, this also holds for the most challenging *scenario 8.b*, where the high UE location error was initially expected to deliver worst performance, but the recovery algorithm and a LABM hysterisis threshold were still able to deliver optimal BPLs.

Largest IQR can be observed for *scenario 5.a* and *8.a*. Such distribution is expected, as *scenario 5.a* includes the UE location error in the *measurement REM* querying without using the recovery algorithm, leading to almost half of all REM queries to fail and leading to the usage of sub-optimal outdated BPLs. *Scenario 8.a* introduces a high urbanization error model for the UE location error in the *measurement REM* querying, while using immediate LABM handovers, which lead to the highest amount of RLF events. Figure 5.31 also shows that for the simulated environment and the selected UE walk path, the hysterisis threshold set to 1 in *scenario 7.a* and *scenario 8.b* lead to the distribution of SINR values on a smaller range with a median close to a higher SINR value than the usage of immediate LABM handovers in *scenario 6.c*. This result confirms that setting LABM handover hysterisis

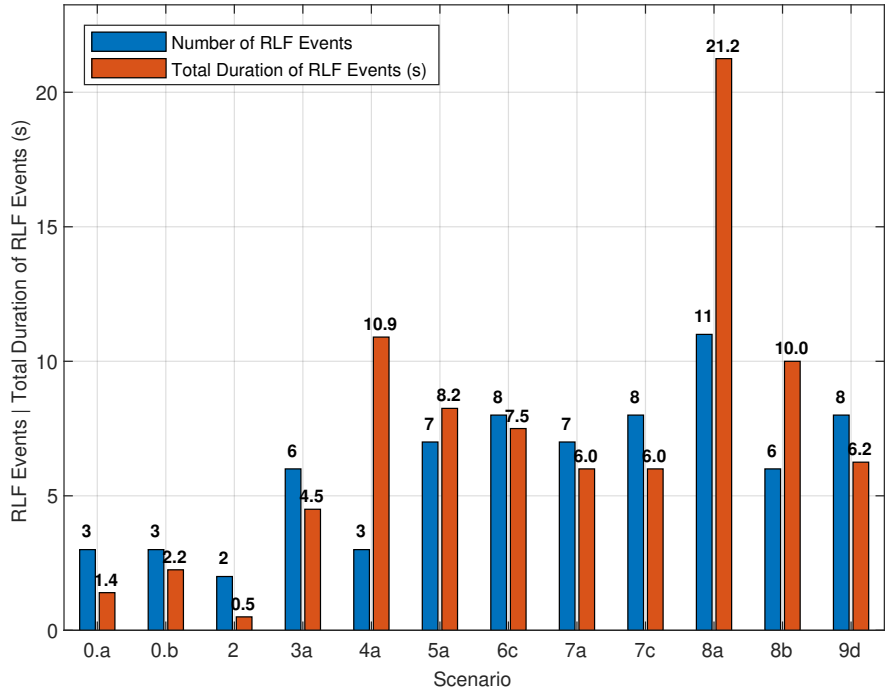

Figure 5.32: Amount of RLF events along the UE walk path and their total duration for selected simulated scenarios.

threshold to 1 or 2 location reports improves the performance of the LABM algorithm in the presence of realistic GNSS error in REM construction and querying.

Figure 5.32 shows the amount of RLF events along the walk path and their duration for each of the selected scenarios. It can be observed that the smallest amount of RLF events in LABM configurations with shortest duration is in the baseline LABM algorithm configuration in *scenario 2*, where no error models are used and the UE location reporting frequency is set to 1 Hz. This is an expected result, as in such configuration the LABM algorithm is able to provide the optimal BPL at almost all times.*Scenario 8.a* shows the worst performance in terms of the amount of RLF events. In this case the UE also spends the most time with the signal quality below the RLF threshold. This is an expected behavior, as the combined effect of UE location errors modeled for high urbanization and the usage of *measurement REM* with immediate LABM handovers cause severe beam misalignment in transitions between LOS and NLOS areas of serving gNBs, and in proximity to the serving gNB. The performance is significantly improved with reduced the amount of RLF events and their total duration by half in *scenario 8.b*, which uses handover hysteris thresholds instead of immediate handovers. This proves again that the decision to not execute immediate LABM handovers tends to contribute to a more stable link quality, allowing the LABM algorithm to operate even in the case of high urbanization error for UE location reports.

The problem caused by the severe beam misalignment in transitions between LOS and NLOS areas of serving gNBs, and in proximity to the serving gNB can also be noticed in *scenario 4.a*, where the LABM is not able to provide a valid non-empty REM entry in similar areas due to lack of recovery algorithm. When comparing *scenario 4.a* to *5.a*, it can be

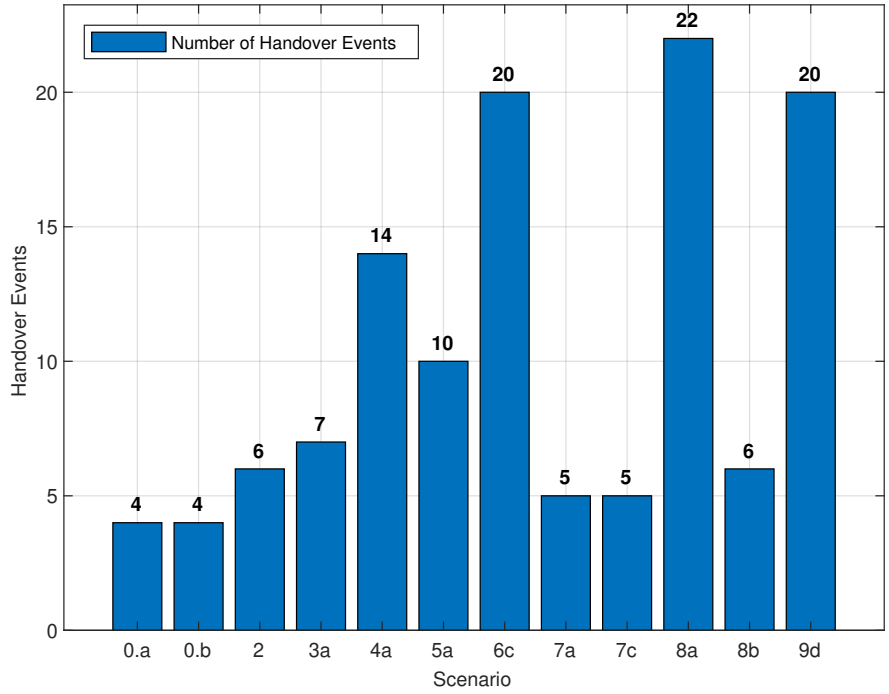

Figure 5.33: Amount of handovers for selected simulated scenarios.

noticed that the amount of RLF events has doubled in *scenario 5.a*, but the duration spent with SINR level below the RLF threshold has decreased. This confirms that when both UE location error in the REM querying and the *measurement REM* are used, the sources of error compensate each other to some extent. Enabling the recovery algorithm in *scenario 6.c* shows a minor improvement in terms of duration of RLF events, but the difference is not significant, as it can not be guaranteed that the recovered location will provide a better BPL than the one that is currently used. Between all scenarios that have both the UE location error in the REM querying and the *measurement REM*, *scenario 7.a* shows the least amount of RLF events and the shortest duration of those. As already mentioned, this behavior is explained by improvements of signal quality in areas of transitions between LOS and NLOS areas of serving gNBs due to delayed decisions to execute a handover. Additionally, the lack of ping-pong handovers in *scenario 7.a* avoids strong fluctuations of the SINR level that lead to RLF events in *scenario 6.c*. *Scenario 9.d* shows results similar to *6.c, 7.a* and *7.c*. As mentioned in the Section 5.6, the average UE velocity is not high enough for the configured reporting delay to have a significant impact on the performance of the LABM algorithm.

Figure 5.33 shows the amount of performed handovers in each of selected scenarios. It can be observed that the delayed decision to execute a handover in *scenario 7.a, 7.c* by disabling the immediate LABM handovers results in the lowest signaling overhead due to the lowest amount of handover events, comparable to the signaling overhead in default 5G-NR network configurations in *scenario 0.a* and *0.b*. *Scenario 7.a, 7.c* show a comparable performance to the default 5G-NR network configuration and execute around 4 times less handovers in comparison to the remaining selected LABM configurations.

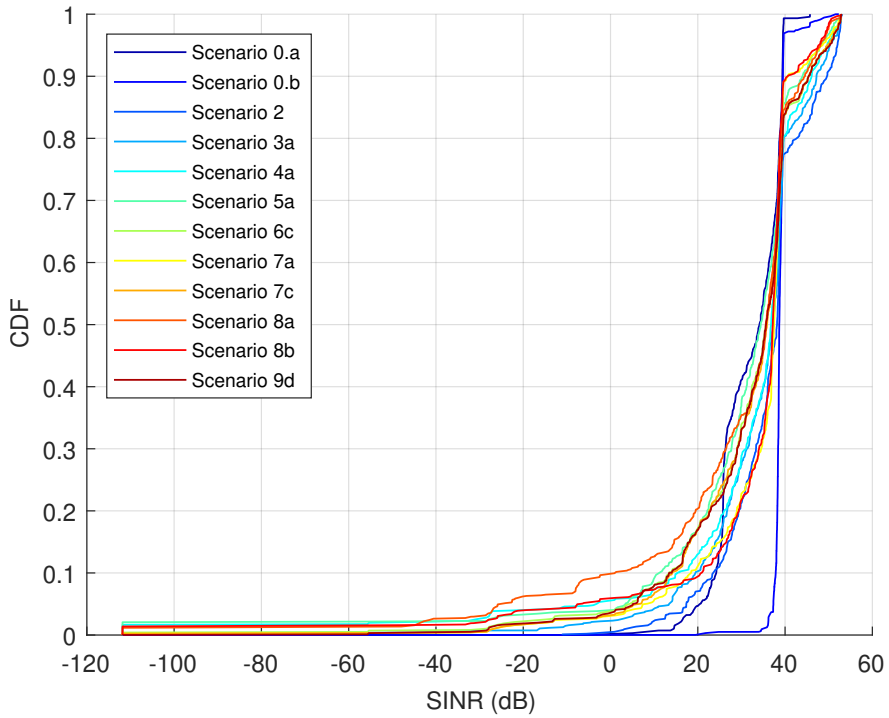

Figure 5.34: CDF plot for SINR distribution along the walk path for selected simulated scenarios.

Figure 5.34 shows a CDF plot of the SINR values along the UE walk path for each of selected scenarios. The overall best performance is observed for the default 5G-NR in *scenario 0.a, 0.b*, baseline LABM in *scenario 2* and *scenario 3.a*, where the LABM algorithm is mostly able to provide optimal BPLs at all times. The worst performance is again shown by *scenario 8.a* due to its failure to provide optimal BPLs at the beginning of the simulation due to the significantly higher influence of location reporting errors in *measurement REM* querying. The fact that the CDF curve has a value of 0.1 at a SINR of $0\ dB$ indicates that up to 10% of the observed SINR values fall within the range of SINR values that is close to the RLF threshold. This suggests that in at least 10% of the cases, the signal quality is poor, leading to degradation of the link stability and decreased IP throughput. *Scenario 7.a* shows the best behavior in comparison to other scenarios that have the UE location error in the *measurement REM* querying.

Finally, Figure 5.35 provides a CDF plot for the achieved IP throughput along the UE walk path in each of the selected scenarios. The trend is very similar to Figure 5.35. The spike in all curves at $400\ Mbit/s$ is explained by the fact that this represents the target throughput set by the remote host. In the region before the target throughput it can be observed, that *scenario 7.a* again shows the best performance from all selected LABM configurations by having a lower probability of having the IP throughput below the target value. Due to strong fluctuations in the SINR level and frequent and long RLF events, *scenario 8.a* demonstrates the worst performance by having the probability of around 18% for the IP throughput to be below the target rate. *Scenario 8.b* shows almost 2 times better performance than the *sceanrio 8.b*, indicating the performance closer to *scenario*

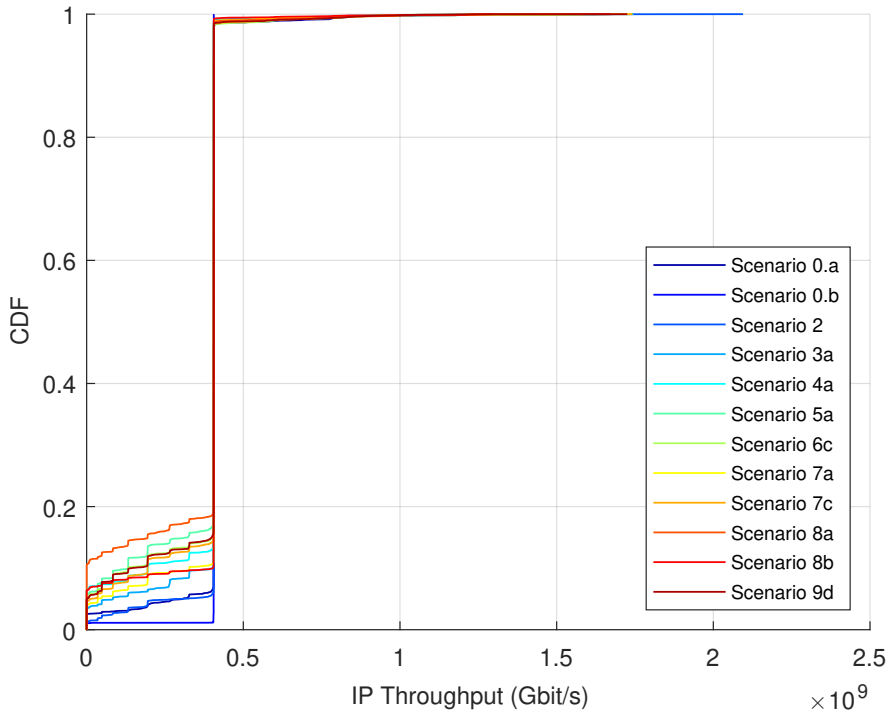

Figure 5.35: CDF plot for IP throughput for selected simulated scenarios.

7.a, which used medium urbanization error for the UE location reports. This is proving again the benefit of using LABM algorithm with a small hysterisis threshold instead of immediate handovers for scenarios that have UE location error in the querying of REM and the *measurement REM*. In general it can be concluded that the usage of the implemented recovery algorithm was not enough to improve the network performance, as it can not be guaranteed that REM queries on recovered locations deliver an optimal BPL. The usage of handover hysterisis thresholds on top of the recovery algorithm was able to prevent ping-pong handovers, leading to a more stable SINR level and reducing the amount and duration of RLF events.

From Figures 5.31, 5.32, 5.34, 5.35 it can be observed, that the *scenario 0.b* with baseline 5G-NR with SSB RLM shows the best performance in terms of most stable SINR with distribution across a small range with median close to $40\ dB$, the smallest amount of handovers and RLF events, and an almost constant IP throughput of $400\ Mbit/s$ along the whole UE walk path. However, such performance comes at the cost of an extreme overhead of 25% of radio resources that are spent for SSB and CSI-RS signals. The LABM algorithm is able to almost completely eliminate the dependency on SSB signals and does not use CSI-RS signals. The LABM performance in *scenario 7.a* and *scenario 8.b* proves that the algorithm is able to maintain relatively stable network performance that is close to the default 5G-NR configuration in *scenario 0.a* and even provide higher peak SINR values in some parts of the walk path. The LABM algorithm achieves this level of performance with minimal signaling overhead, demonstrating its feasibility for deployment in real-world networks.

6

Conclusion and Future Work

In this thesis, an implementation of LABM algorithm for 5G networks in the ns-3 network simulator was presented. The information about the UE location was assumed to be provided by a consumer-grade GNSS modules with no error compensation. The associated localization inaccuracies were modeled with help of the Ornstein-Uhlenbeck stochastic process with parameters derived from the measurement data in the previous work by authors in [60]. The RRC layer of the LTE coordinator eNB in the simulated NSA 5G network architecture was extended to store and query the REM. The REM was constructed from the output data of the Wireless InSite ray-tracing software that models the mmWave propagation in the selected simulation are in Frankfurt, Germany. In order to model the realistic location error in REM construction, i.e. *measurement REM*, a normally distributed error was applied to the latitude and longitude components of the location, for which each REM entry was stored. The main focus was to investigate the individual and combined effect of UE location error in REM querying and of the *measurement REM*. To enable this, a new algorithm was implemented on the LTE coordinator's RRC layer to implement the LABM. The algorithm was tested in a variety of scenarios and the influence of each available parameter was analyzed.

The ideal configuration of the LABM algorithm with no error models and the UE location reporting frequency of 1 Hz has shown an improvement in comparison to the default 5G-NR network configuration in terms of maximum achieved SINR. The LABM algorithm also allows to eliminate exhaustive beam sweeping after the first IA. In the case when the first ever REM query returns a non-empty REM entry with a BPL close to the optimal one, the IA procedure in the beginning of the simulation can be skipped and the UE is able to receive data almost immediately after the simulation start. It was shown that the individual contribution of the UE location error in REM querying is leading to an increased amount of RLF events due to failure to execute a handover from a NLOS gNB. Moreover, the individual error contribution of the *measurement REM* leads to prolonged periods of time spent with SINR below the RLF threshold, as the LABM is either not able to successfully query the REM for the reported location, or provides a REM entry that stores the BPL for a different location in the simulation environment. The effect of UE location error in querying the *measurement REM* has shown that both error sources tend to compensate each other to a certain degree. In addition, the fact that some *measurement REM* entries are stored at locations inside of obstacles, the previously failed query at an erroneous reported location may now return a non-empty REM entry. The implemented recovery algorithm based on the Bresenham's line algortihm was shown to be effective in majority of cases in simulated scenarios for the selected UE walk path, recovering almost all previously failed query attempts. However, it was shown that the recovery algorithm may not always recover the reported UE location to an optimal location. Importantly, it was shown that the decision to delay an execution of the handover to the best gNB according

to the queried REM entry is beneficial in terms of avoiding the handover signaling overhead and providing a more stable communication link.

In conclusion, this thesis demonstrated the performance of the LABM scheme implemented in the ns-3 simulator in the presence of realistic location errors. It was shown that the implemented LABM algorithm is able to provide stable link quality even in the case when UE location error in REM querying was simulated together with the usage of the *measurement REM*. The available parameters of LABM algorithm have allowed to find an optimal configuration that minimizes the signaling overhead from handover events and improves the link stability.

Although the proposed algorithm has shown promising results, there remain several aspects that could be explored in future work. In this thesis the REM was assumed to be already constructed and available to the LTE coordinator from the beginning of the simulation. This is not guaranteed to be the case in a real world network deployment. Thus, the possible approaches of an online REM construction from the reported measurements by UE of DL control signals such as SSBs could be investigated. Moreover, due to time constraints, this thesis focused on the simulation with a single UE present in the network. The increased amount of UE may raise load-balancing-related problems and further improvements that will be required in the LABM algorithm. Furthermore, as mentioned in previous sections, the simulated mobility model used for the UE assumed a relatively slow velocity of around $1\ m/s$. An increased velocity of the UE will most probably lead to stronger contribution of possible delays in the location reporting procedure. Additionally, the implemented recovery algorithm triggered in the cases when the REM query failed for the reported location has shown to be ineffective or having detrimental effect on SINR in the cases when the recovered location was still assuming a LOS to the serving gNB, whereas the real UE location was already in the NLOS area. This highlights the need for developing more optimal recovery algorithms for the LABM scheme to enhance its efficiency and reliability.

A

Abbreviations

3GPP 3rd Generation Partnership Project

5G-NR 5G New Radio

5GC 5G Core Network

A-GNSS Assisted GNSS

AMF Access and Mobility Management Function

AoA Angle of Arrival

AoD Angle of Departure

ADC Analog to Digital Converter

BPL Beam Pair Link

BWP Bandwidth Part

CBR Constant Bit Rate

CDF Cumulative Distribution Function

CO Coordinator

CP Cycling Prefix

CSI-RS Channel State Information Reference Signal

CTTC Centre Tecnològic de Telecomunicacions de Catalunya

CQI Channel Quality Indicator

DAC Digital to Analog Converter

DC Dual Connectivity

DCI Downlink Control Information

DL Downlink

DL-AOD Downlink Angle of Departure

DL-TDOA Downlink Time Difference of Arrival

DoA Direction of Arrival

DoD Direction of Departure

DM-RS DeModulation Reference Signal

DRB Data Radio Bearer

DSP Digital Signal Processor

E-CID Enhanced Cell-ID

E-SMLC Enhanced Serving Mobile Location Centre

E-UTRAN Evolved Universal Terrestrial Radio Access Network

EPC Enhanced Packet Core

eMBB Enhanced Mobile Broadband

EN-DC Evolved Universal Terrestrial Radio Access New Radio Dual Connectivity

eNB Enhanced Node B

FDD Frequency Division Duplex

FR1 Frequency Range 1

FR2 Frequency Range 2

FSPL Free Space Path Loss

GCS Global Coordinate System

gNB Next Generation Node B

GNSS Global Navigation Satellite System

GPS Global Positioning System

GSM Global System for Mobile Telecommunications

GTP GPRS Tunneling Protocol

HARQ Hybrid Automatic Repeat Request

HO Handover

IA Initial Access

IP Internet Protocol

IPSD Interference Power Spectral Density

IMSI International Mobile Subscriber Identity

IMU Inertial Measurement Unit

IQR Inter Quartile Range

KNN K-Nearest Neighbor

KPI Key Performance Indicator

LABM Location-Aided Beam Management

LCS Local Coordinate System

LMF Location Management Function

LOS Line of Sight

LPP LTE Positioning Protocol

LTE Long Term Evolution

MAC Medium Access Control

mMTC Massive Machine Type Communications

MIB Master Information Block

MIMO Multiple Input Multiple Output

mIoT Massive Internet of Things

MR Maximum Rate

MU-MIMO Multi-User MIMO

Multi-RTT Multi-Round-Trip-Time

NAS Non-Access Stratum

NF Network Function

ng-eNB New Generation Enhanced Node B

NG-RAN New Generation Radio Access Network

NLOS Non Line of Sight

NN Neural Network

NR New Radio

NRPPa NR Positioning Protocol A

NSA Non-Standalone Architecture

NSA-DL Non-Standalone-Downlink Architecture

NSA-UL Non-Standalone-Uplink Architecture

NZP Non-Zero Power

OFDM Orthogonal Frequency-Division Multiplexing

OFDMA Orthogonal Frequency Division Multiple Access

OSI Open Systems Interconnection

OTDOA Observed Time Difference Of Arrival

P2P Point-to-Point

PBCH Physical Broadcast Channel

PCAP Packet Capture

PDCP Packet Data Convergence Protocol

PDSCH Physical Downlink Shared Channel

PDU Protocol Data Unit

PF Proportional Fair

PGW Packet Data Network Gateway

PHY Physical Layer of the OSI model

PRB Physical Resource Block

PRS Positioning Reference Signal

PSS Primary Synchronization Signal

QoS Quality of Service

RA Random Access

RACH Random Access Channel

RAN Radio Access Network

RAT Radio Access Technology

RBG Ressource Block Group

REM Radio Environment Map

RF Radio Frequency

RLC Radio Link Controller

RLF Radio Link Failure

RLM Radio Link Monitoring

RNTI Radio Network Temporary Identifier

RR Round Robin

RRC Radio Resource Controller

RSRP Reference Signal Received Power

RSRQ Reference Signal Received Quality

RSTD Reference Signal Time Difference

RX Receiver

SA Standalone Architecture

SA-DL Standalone-Downlink

SAP Service Access Point

SBA Service-Based Architecture

SCS Subcarrier Spacing

SGW Service Gateway

SINR Signal to Interference and Noise Ratio

SLP SUPL Location Platform

SNR Signal to Noise Ratio

SRB Signaling Radio Bearer

SRS Sounding Reference Signal

SS Synchronization Signal

SSB Synchronisation Signal Block

SSS Secondary Synchronization Signal

SU-MIMO Single-User MIMO

SUPL Secure User Plane Location

SVM Support Vector Machine

TDD Time Division Duplex

TDMA Time Division Multiple Access

TDOA Time Difference Of Arrival

TCP Transmission Control Protocol

ToA Time of Arrival

TTI Transmission Time Interval

TX Transmitter

UDP User Datagram Protocol

UE User Equipment

UL Uplink

UL-AOA Uplink Angle of Arrival

UL-TDOA Uplink Time Difference of Arrival

UM Unacknowledged Mode

UPF User Plane Function

URLLC Ultra-reliable and Low Latency Communication

USIM Universal Subscriber Identity Module

V2X Vehicle-to-Everything

WiIS Wireless InSite

WLAN Wireless Local Area Network

List of Tables

List of Figures

Bibliography

[1] N. Patriciello, S. Lagen, B. Bojovic, and L. Giupponi, "An E2E Simulator for 5G NR Networks," 2019. [Online]. Available: https://arxiv.org/abs/1911.05534

[2] O. Atasoy, "Simulation of Beam Management in 5G-NR Millimeter-wave Cellular Networks in ns-3," M.Sc. thesis, RWTH Aachen, 2021.

[3] *3GPP Technical Report TR 38.913*, "*Study on Scenarios and Requirements for Next Generation Access Technologies*," 3GPP, Tech. Rep. version 14.2.0, 05 2017.

[4] *3GPP Technical Report TR 121.915*, "*Technical Specification Group Services and System Aspects; Release description; Release 15*," 3GPP, Tech. Rep. version 15.0.0, 10 2019.

[5] H. Jin, K. Liu, M. Zhang, L. Zhang, G. Lee, E. N. Farag, D. Zhu, E. Onggosanusi, M. Shafi, and H. Tataria, "Massive mimo evolution toward 3gpp release 18," *IEEE Journal on Selected Areas in Communications*, vol. 41, no. 6, pp. 1635–1654, 2023.

[6] T. Obara, T. Okuyama, Y. Inoue, Y. Aoki, S. Suyama, J. Lee, and Y. Okumura, "Experimental trial of 5g super wideband wireless systems using massive MIMO beamforming and beam tracking control in 28ghz band," vol. E100.B, no. 8, pp. 1256–1268. [Online]. Available: https://www.jstage.jst.go.jp/article/transcom/E100.B/8/E100.B_2016FGP0020/_article

[7] *3GPP Technical Specification TS 38.104*, "*NR; Base Station (BS) radio transmission and reception*," 3GPP, Tech. Rep. version 17.0.0, 01 2024.

[8] *3GPP Technical Specification TS 38.101*, "*NR - User Equipment (UE) radio transmission and reception - Part 2: Range 2 Standalone*," 3GPP, Tech. Rep. version 16.5.0, 2021.

[9] T. S. Rappaport, *Wireless Communications: Principles and Practice*, 2nd ed. Prentice Hall, 2002.

[10] T. S. Rappaport, S. Sun, R. Mayzus, H. Zhao, Y. Azar, K. Wang, G. N. Wong, J. K. Schulz, M. Samimi, and F. Gutierrez, "Millimeter Wave Mobile Communications for 5G Cellular: It Will Work!" *IEEE Access*, vol. 1, pp. 335–349, 2013.

[11] International Telecommunication Union (ITU), "Attenuation by Atmospheric Gases: Recommendation ITU-R P.676-12," International Telecommunication Union (ITU), Tech. Rep. P.676-12, 2019, accessed: March 15, 2025. [Online]. Available: https://www.fccdecastro.com.br/pdf/ITU-RP676-12.pdf

[12] I. Rodriguez, H. C. Nguyen, T. B. Sørensen, J. Elling, J. Å. Holm, P. E. Mogensen, and B. Vejlgaard, "Analysis of 38 GHz mmWave Propagation Characteristics of Urban Scenarios," 2015. [Online]. Available: https://api.semanticscholar.org/CorpusID:55667113

[13] T. S. Rappaport, G. R. MacCartney, M. K. Samimi, and S. Sun, "Wideband Millimeter-Wave Propagation Measurements and Channel Models for Future Wireless Communication System Design," *IEEE Transactions on Communications*, vol. 63, no. 9, pp. 3029–3056, 2015.

[14] M. K. Samimi, G. R. MacCartney, S. Sun, and T. S. Rappaport, "28 GHz Millimeter-Wave Ultrawideband Small-Scale Fading Models in Wireless Channels," publisher: arXiv Version Number: 2. [Online]. Available: https://arxiv.org/abs/1511.06938

[15] S. Kutty and D. Sen, "Beamforming for Millimeter Wave Communications: An Inclusive Survey," *IEEE Communications Surveys Tutorials*, vol. 18, no. 2, pp. 949–973, 2016.

[16] *3GPP Technical Report TR 21.915*, "*NR and NG-RAN Overall Description; Stage 2*," 3GPP, Tech. Rep. version 17.0.0, 03 2023.

[17] G. Liu, Y. Huang, Z. Chen, L. Liu, Q. Wang, and N. Li, "5g deployment: Standalone vs. non-standalone from the operator perspective," *IEEE Communications Magazine*, vol. 58, no. 11, pp. 83–89, 2020.

[18] M. Giordani, M. Polese, A. Roy, D. Castor, and M. Zorzi, "Standalone and Non-Standalone Beam Management for 3GPP NR at mmWaves," *IEEE Communications Magazine*, vol. 57, no. 4, pp. 123–129, 2019.

[19] M. Polese, M. Giordani, M. Mezzavilla, S. Rangan, and M. Zorzi, "Improved Handover Through Dual Connectivity in 5G mmWave Mobile Networks," *IEEE Journal on Selected Areas in Communications*, vol. 35, no. 9, pp. 2069–2084, 2017.

[20] M. Giordani, M. Mezzavilla, S. Rangan, and M. Zorzi, "An efficient uplink multi-connectivity scheme for 5g millimeter-wave control plane applications," *IEEE Transactions on Wireless Communications*, vol. 17, no. 10, pp. 6806–6821, 2018.

[21] 3GPP, "*NR PRACH Preamble Resource Allocation*," Ericsson, Tech. Rep. Tdoc RAN1 87, R1-1611905, Nov. 2016.

[22] Motorola Mobility, Lenovo, "Discussion on remaining issues of SS block and SS burst set," 3GPP, Tdoc R1-1714212, 2017.

[23] M. Giordani, M. Polese, A. Roy, D. Castor, and M. Zorzi, "A Tutorial on Beam Management for 3GPP NR at mmWave Frequencies," *IEEE Communications Surveys Tutorials*, vol. 21, no. 1, pp. 173–196, 2019.

[24] *3GPP Technical Specification TS 38.211*, "*NR; Physical channels and modulation*," 3GPP, Tech. Rep., 06 2020.

[25] Samsung, "Framework for beamformed access," 3GPP TSG RAN WG1, Technical Document Tdoc R1-164013, 2016.

[26] *3GPP Technical Specification TS 38.331*, "*NR; Radio Resource Control (RRC); Protocol specification*," 3GPP, Tech. Rep. version 16.1.0, 07 2020.

[27] *3GPP Technical Specification TS 38.300*, "*5G NR - NR and NG-RAN Overall Description - Stage 2*," 3rd Generation Partnership Project, Tech. Rep. version 15.13.0, 09 2021.

[28] *3GPP Technical Specification TS 38.305*, "*NR; Positioning Architecture*," ETSI, Tech. Rep. version 17.0.0, 03 2023.

[29] *3GPP Technical Specification TS 36.355*, "*LTE; Evolved Universal Terrestrial Radio Access (E-UTRA); LTE Positioning Protocol (LPP)*," 3GPP, Tech. Rep. version 11.1.0, 03 2013.

[30] A. Ali, N. González-Prelcic, and R. W. Heath, "Millimeter Wave Beam-Selection Using Out-of-Band Spatial Information," *IEEE Transactions on Wireless Communications*, vol. 17, no. 2, pp. 1038–1052, 2018.

[31] A. Schott, E. Tosi, F. Chiariotti, and L. Simić, "Impact of Realistic GNSS Location Errors on REM-Based Beam Management in Urban Millimeter-Wave Networks," in *2024 IEEE International Symposium on Dynamic Spectrum Access Networks (DySPAN)*, 2024, pp. 383–392.

[32] Y. Zeng and X. Xu, "Toward Environment-Aware 6G Communications via Channel Knowledge Map," *IEEE Wireless Communications*, vol. 28, no. 3, pp. 84–91, 2021.

[33] H. B. Yilmaz, T. Tugcu, F. Alagöz, and S. Bayhan, "Radio environment map as enabler for practical cognitive radio networks," *IEEE Communications Magazine*, vol. 51, no. 12, pp. 162–169, 2013.

[34] A. Ichkov, P. Mähönen, and L. Simić, "Is ray-tracing viable for millimeter-wave networking studies?" in *2020 IEEE 31st Annual International Symposium on Personal, Indoor and Mobile Radio Communications*, 2020, pp. 1–7.

[35] M. Mezzavilla, M. Zhang, M. Polese, R. Ford, S. Dutta, S. Rangan, and M. Zorzi, "End-to-End Simulation of 5G mmWave Networks," *IEEE Communications Surveys Tutorials*, vol. 20, no. 3, pp. 2237–2263, 2018.

[36] N. Baldo, M. Miozzo, M. Requena-Esteso, and J. Nin-Guerrero, "An open source product-oriented LTE network simulator based on ns-3," in *Proceedings of the 14th ACM international conference on Modeling, analysis and simulation of wireless and mobile systems*. ACM, pp. 293–298. [Online]. Available: https://dl.acm.org/doi/10.1145/2068897.2068948

[37] *3GPP Technical Specification TS 36.322*, "*LTE; Evolved Universal Terrestrial Radio Access (E-UTRA); Radio Link Control (RLC) protocol specification*," 3GPP, Tech. Rep. version 15.1.0, 06 2018.

[38] A. Ichkov, O. Atasoy, P. Mähönen, and L. Simić, "Full-stack ns-3 framework for the evaluation of 5g-nr beam management in non-standalone downlink millimeter-wave networks," in *2022 IEEE 23rd International Symposium on a World of Wireless, Mobile and Multimedia Networks (WoWMoM)*, 2022, pp. 40–49.

[39] A. M. Nor, S. Halunga, and O. Fratu, "Survey on positioning information assisted mmWave beamforming training," vol. 135, p. 102947. [Online]. Available: https://linkinghub.elsevier.com/retrieve/pii/S1570870522001287

[40] J. Morais, A. Bchboodi, H. Pezeshki, and A. Alkhateeb, "Position-Aided Beam Prediction in the Real World: How Useful GPS Locations Actually are?" in *ICC 2023 - IEEE International Conference on Communications*, 2023, pp. 1824–1829.

[41] M. Arvinte, M. Tavares, and D. Samardzija, "Beam Management in 5G NR using Geolocation Side Information," in *2019 53rd Annual Conference on Information Sciences and Systems (CISS)*, 2019, pp. 1–6.

[42] M. B. Mollah, H. Wang, and H. Fang, "Position Aware 60 GHz mmWave Beamforming for V2V Communications Utilizing Deep Learning," in *ICC 2024 - IEEE International Conference on Communications*, 2024, pp. 4711–4716.

[43] Y. Lu, M. Koivisto, J. Talvitie, M. Valkama, and E. S. Lohan, "Positioning-Aided 3D Beamforming for Enhanced Communications in mmWave Mobile Networks," *IEEE Access*, vol. 8, pp. 55 513–55 525, 2020.

[44] N. Garcia, H. Wymeersch, E. G. Ström, and D. Slock, "Location-aided mm-wave channel estimation for vehicular communication," in *2016 IEEE 17th International Workshop on Signal Processing Advances in Wireless Communications (SPAWC)*, 2016, pp. 1–5.

[45] J. C. Aviles and A. Kouki, "Position-Aided mm-Wave Beam Training Under NLOS Conditions," *IEEE Access*, vol. 4, pp. 8703–8714, 2016.

[46] S. Khosravi, H. S. Ghadikolaei, J. Zander, and M. Petrova, "Location-aided beamforming in mobile millimeter-wave networks," in *2022 IEEE 95th Vehicular Technology Conference: (VTC2022-Spring)*, 2022, pp. 1–7.

[47] V. Va, T. Shimizu, G. Bansal, and R. W. Heath, "Online Learning for Position-Aided Millimeter Wave Beam Training," version Number: 3. [Online]. Available: https://arxiv.org/abs/1809.03014

[48] F. Maschietti, D. Gesbert, P. de Kerret, and H. Wymeersch, "Robust Location-Aided Beam Alignment in Millimeter Wave Massive MIMO," in *GLOBECOM 2017 - 2017 IEEE Global Communications Conference*, 2017, pp. 1–6.

[49] M. Hoffmann and P. Kryszkiewicz, "Beam management driven by radio environment maps in o-ran architecture," in *2023 IEEE International Conference on Communications Workshops (ICC Workshops)*, 2023, pp. 54–59.

[50] A. Schott, "Simulation of Multi-user 5G-NR Millimeter-Wave Mobile Cellular Networks in ns-3," M.Sc. thesis, RWTH Aachen, 2022.

[51] A. Ichkov, A. Schott, P. Mähönen, and L. Simić, "flexRLM: Flexible Radio Link Monitoring for Multi-User Downlink Millimeter-Wave Networks," in *IEEE INFOCOM 2023 - IEEE Conference on Computer Communications*, 2023, pp. 1–10.

[52] Centre Tecnológic de Telecomunicacions de Catalunya (CTTC), "Radio Environment Map (REM) - 5G-LENA Documentation," 2024, accessed: February 22, 2025. [Online]. Available: https://5g-lena.cttc.es/features/rem/

[53] L. Simić, J. Riihijärvi, A. Venkatesh, and P. Mähönen, "Demo abstract: An open source toolchain for planning and visualizing highly directional mm-wave cellular networks in the 5g era," in *2017 IEEE Conference on Computer Communications Workshops (INFOCOM WKSHPS)*, 2017, pp. 966–967.

[54] A. W. Soundy, B. J. Panckhurst, and T. C. Molteno, "Enhanced noise models for GPS positioning," in *2015 6th International Conference on Automation, Robotics and Applications (ICARA)*, 2015, pp. 28–33.

[55] S. Kuchuk-Iatsenko and Y. Mishura, "Option pricing in the model with stochastic volatility driven by OrnsteinâUhlenbeck process. Simulation," vol. 2, no. 4, pp. 355–369. [Online]. Available: https://www.vmsta.org/doi/10.15559/15-VMSTA43

[56] J. E. Bresenham, "Algorithm for computer control of a digital plotter," *IBM Systems Journal*, vol. 4, no. 1, pp. 25–30, 1965.

[57] *3GPP Technical Specification TS 38.901*, "*Study on channel model for frequencies from 0.5 to 100 GHz*," 3GPP, Tech. Rep. version 15.0.0, 2018.

[58] M. Zhang, M. Polese, M. Mezzavilla, S. Rangan, and M. Zorzi, "ns-3 implementation of the 3gpp mimo channel model for frequency spectrum above 6 ghz," in *Proceedings of the 2017 Workshop on Ns-3*, ser. WNS3 '17. New York, NY, USA: Association for Computing Machinery, 2017, p. 71â78. [Online]. Available: https://doi.org/10.1145/3067665.3067678

[59] PTV Group, "PTV Viswalk," 2025, [Online; accessed 28-Feb-2025]. [Online]. Available: https://www.ptvgroup.com/en/solutions/products/ptv-viswalk/

[60] E. Tosi, "Effect of localization error on the performance of location-aided beam-management in 5G and beyond," M.Sc. thesis, RWTH Aachen, 2023.

[61] [Online]. Available: https://github.com/inets-rwth/ns3-flexRLM

[62] T. S. Rappaport, Y. Xing, G. R. MacCartney, A. F. Molisch, E. Mellios, and J. Zhang, "Overview of Millimeter Wave Communications for Fifth-Generation (5G) Wireless NetworksâWith a Focus on Propagation Models," *IEEE Transactions on Antennas and Propagation*, vol. 65, no. 12, pp. 6213–6230, 2017.

Zentrales Prüfungsamt/Central Examination Office

Eidesstattliche Versicherung
Statutory Declaration in Lieu of an Oath

Name, Vorname/Last Name, First Name

Matrikelnummer (freiwillige Angabe)
Matriculation No. (optional)

Ich versichere hiermit an Eides Statt, dass ich die vorliegende Arbeit/Bachelorarbeit/ Masterarbeit* mit dem Titel
I hereby declare in lieu of an oath that I have completed the present paper/Bachelor thesis/Master thesis* entitled

selbstständig und ohne unzulässige fremde Hilfe (insbes. akademisches Ghostwriting) erbracht habe. Ich habe keine anderen als die angegebenen Quellen und Hilfsmittel benutzt. Für den Fall, dass die Arbeit zusätzlich auf einem Datenträger eingereicht wird, erkläre ich, dass die schriftliche und die elektronische Form vollständig übereinstimmen. Die Arbeit hat in gleicher oder ähnlicher Form noch keiner Prüfungsbehörde vorgelegen.
independently and without illegitimate assistance from third parties (such as academic ghostwriters). I have used no other than the specified sources and aids. In case that the thesis is additionally submitted in an electronic format, I declare that the written and electronic versions are fully identical. The thesis has not been submitted to any examination body in this, or similar, form.

Ort, Datum/City, Date

Unterschrift/Signature

*Nichtzutreffendes bitte streichen

*Please delete as appropriate

Belehrung:
Official Notification:

§ 156 StGB: Falsche Versicherung an Eides Statt
Wer vor einer zur Abnahme einer Versicherung an Eides Statt zuständigen Behörde eine solche Versicherung falsch abgibt oder unter Berufung auf eine solche Versicherung falsch aussagt, wird mit Freiheitsstrafe bis zu drei Jahren oder mit Geldstrafe bestraft.
Para. 156 StGB (German Criminal Code): False Statutory Declarations
Whoever before a public authority competent to administer statutory declarations falsely makes such a declaration or falsely testifies while referring to such a declaration shall be liable to imprisonment not exceeding three years or a fine.
§ 161 StGB: Fahrlässiger Falscheid; fahrlässige falsche Versicherung an Eides Statt
(1) Wenn eine der in den §§ 154 bis 156 bezeichneten Handlungen aus Fahrlässigkeit begangen worden ist, so tritt Freiheitsstrafe bis zu einem Jahr oder Geldstrafe ein.
(2) Straflosigkeit tritt ein, wenn der Täter die falsche Angabe rechtzeitig berichtigt. Die Vorschriften des § 158 Abs. 2 und 3 gelten entsprechend.
Para. 161 StGB (German Criminal Code): False Statutory Declarations Due to Negligence
(1) If a person commits one of the offences listed in sections 154 through 156 negligently the penalty shall be imprisonment not exceeding one year or a fine.
(2) The offender shall be exempt from liability if he or she corrects their false testimony in time. The provisions of section 158 (2) and (3) shall apply accordingly.

Die vorstehende Belehrung habe ich zur Kenntnis genommen:
I have read and understood the above official notification:

Ort, Datum/City, Date

Unterschrift/Signature